

Combining cryogenic ion spectroscopy with ion mobility for the study of glycan fragmentation

Présentée le 28 octobre 2021

Faculté des sciences de base
Laboratoire de chimie physique moléculaire
Programme doctoral en chimie et génie chimique

pour l'obtention du grade de Docteur ès Sciences

par

Robert Paul PELLEGRINELLI

Acceptée sur proposition du jury

Prof. H. Girault, président du jury
Prof. T. Rizzo, directeur de thèse
Dr I. Compagnon, rapporteuse
Prof. R. Zenobi, rapporteur
Dr M. Drabbels, rapporteur

"They did not know it was impossible so they did it"

- Mark Twain

Abstract

The importance of glycans in biological processes are matched by their structural complexity. Coating the surface of most living cells, glycans play key roles in many biological processes, and the role they play is closely related to their structures. Structural determination of glycans remains however very challenging, due to the isomeric complexity inherent to this class of molecules. Many of the monosaccharides which make up the building blocks of glycans are isomeric, and can link together in various positions, resulting in a vast number of constitutional isomers and anomers. Furthermore, glycan synthesis is not template driven, resulting in glycans being naturally heterogenous, with a wide range of different structures occurring from cell to cell. This thesis presents a new approach, aimed at determining glycan primary structure, by combining collision-induced dissociation (CID) with cryogenic messenger-tagging infrared spectroscopy and ultra-high resolution ion mobility (IMS), performed on home-built state-of-the-art instruments.

The first part of this thesis gives an overview of the instrumentation used to carry out the research presented. A detailed account of the addition of a new, ultra-high resolution ion mobility stage to the existing apparatus is provided, along with its characterization.

We then investigate the generality of initial findings, showing that glycan C fragments generated by CID from disaccharides retain the anomericity of the glycosidic bond, and demonstrate that this rule extends to larger C fragments than those observed in the initial study and also applies to large, and branched parent molecules. These findings are significant as they imply that C fragments always appear to retain the anomericity of the glycosidic bond from which it was generated, a property that will greatly benefit glycan sequencing.

Next, we present a methodology developed, using Y fragments generated from mobility-separated glycans, to identify which mobility-separated species correspond to the α and β reducing-end anomers. This allows us to distinguish the reducing anomers from other structures when studying a mixture of isomeric glycans by IMS. The data obtained from studying C and Y fragments of glycans can be used in a complementary way to build a spectroscopic database, which assigns exact glycan structures to specific infrared spectra. The creation of such a database would allow for rapid and exact identification of glycans, greatly advancing the field of glycomics.

Finally, the cyclic oligosaccharide β -cyclodextrin was investigated by spectroscopy and IMS. The structures of its main dissociation products were computed by electronic structure calculations and compared to their experimental vibrational spectra. The fragments observed corresponded in mass to either B-type or Z-type fragments, and the calculated lowest energy structures which match the experimental data seem to indicate that the fragments observed are 2-ketone B fragments. Further investigation of B fragments generated from other systems may indicate a correlation between the structure of these fragments and the type of glycosidic bond from which they are produced. If this turns out to be the case, then B fragments can also be added to the spectroscopic database as identifiers for glycan structures.

Keywords: collision-induced dissociation, cryogenic spectroscopy, ion mobility spectrometry, glycans, glycan isomers, glycan anomers, anomer retention, cyclodextrin.

Résumé

L'importance des glycanes dans les processus biologiques est comparable à leur complexité structurale. Recouvrant la surface de la plupart des cellules vivantes, les glycanes jouent un rôle clé dans de nombreux processus biologiques, et ceci est étroitement lié à leurs structures. La détermination structurale des glycanes reste cependant très difficile, en raison de la complexité isomérique inhérente à cette classe de molécules. De nombreux monosaccharides qui constituent les blocs de construction des glycanes sont des isomères et peuvent se lier entre eux en différentes positions, ce qui donne lieu à un grand nombre d'isomères constitutionnels et d'anomères. De plus, la synthèse des glycanes n'est pas pilotée par un modèle, ce qui fait que les glycanes sont naturellement hétérogènes, avec un large éventail de structures différentes d'une cellule à l'autre. Cette thèse présente une nouvelle approche, visant à déterminer la structure primaire des glycanes, en combinant la dissociation induite par collision (CID) avec la spectroscopie infrarouge cryogénique et la mobilité ionique à ultra-haute résolution (IMS), réalisée sur des instruments de pointe faits maison.

La première partie de cette thèse donne un aperçu de l'instrumentation utilisée pour mener à bien les recherches présentées. Un compte rendu détaillé de l'ajout de la mobilité ionique à ultra-haute résolution à l'appareil existant est fourni, ainsi que sa caractérisation.

Nous étudions ensuite la généralité des résultats initiaux, montrant que les fragments C de glycans générés par CID à partir de disaccharides conservent l'anoméricité de la liaison glycosidique, et démontrons que cette règle s'étend à des fragments C plus grands que ceux observés dans l'étude initiale et s'applique également à des molécules parentes plus grandes et ramifiées. Ces résultats sont importants car ils impliquent que les fragments C semblent toujours conserver l'anoméricité de la liaison glycosidique à partir de laquelle ils ont été générés, une propriété qui profitera grandement au séquençage des glycanes.

Ensuite, nous présentons une méthodologie développée, en utilisant des fragments Y générés à partir de glycanes séparés par mobilité, pour identifier quelles espèces séparées par mobilité correspondent aux anomères α et β réductrices. Cela nous permet de distinguer les anomères réducteurs des autres structures lors de l'étude d'un mélange de glycanes isomériques. Les données obtenues par l'étude des fragments C et Y des glycanes peuvent être utilisées de manière complémentaire pour construire une base de données spectroscopique, qui attribue des structures exactes de glycanes à des spectres infrarouges spécifiques. La création d'une telle base de données permettrait une identification rapide et exacte des glycanes, ce qui ferait progresser de manière significative le domaine de la glycomique.

Enfin, l'oligosaccharide cyclique β -cyclodextrine a été étudié par spectroscopie et IMS. Les structures de ses principaux produits de dissociation ont été calculées par des calculs de structure électronique et comparées à leurs spectres vibrationnels expérimentaux. Les fragments observés correspondaient en masse à des fragments de type B ou de type Z, et les structures calculées de plus basse énergie qui correspondent aux données expérimentales semblent indiquer que les fragments observés sont des fragments B de structure 2-cétone. Une étude plus approfondie des fragments B générés à partir

d'autres systèmes pourrait indiquer une corrélation entre la structure de ces fragments et le type de liaison glycosidique à partir duquel ils sont produits. Si cela s'avère être le cas, alors les fragments B peuvent également être ajoutés à la base de données spectroscopique en tant qu'identificateurs des structures de glycanes.

Mots clés : dissociation induite par collision, spectroscopie cryogénique, spectrométrie de mobilité ionique, glycanes, isomères de glycanes, anomères de glycanes, rétention d'anomères, cyclodextrine.

List of abbreviations

Abbreviation	Definition
ATD	arrival time distribution
CCS	collision cross section
CD	cyclodextrin
CE	capillary electrophoresis
CID	collision-induced dissociation
DFT	density functional theory
ECD	electron capture dissociation
EDD	electron detachment dissociation
ESI	electrospray ionization
ETD	electron transfer dissociation
FAB	fast atom bombardment
FAIMS	field asymmetric ion mobility
HPLC	high-pressure liquid chromatography
IMS	ion mobility spectrometry
IR	infrared
IRMPD	infrared multiple photon dissociation
LC	liquid chromatography
MALDI	matrix-assisted laser desorption
MIPS	Modular Intelligent Power Sources
Nd:YAG	neodymium-doped yttrium aluminium garnet
MS	mass spectrometry
NMR	nuclear magnetic resonance
OPO	optical parametric oscillator
PCB	printed circuit board
RF	radiofrequency
SLIM	structures for lossless ion manipulation
SNGF	Symbol Nomenclature for Glycans
TOF	time of flight
TW	travelling wave
UV	ultraviolet
ZPE	zero-point energy

Table of contents

<i>Abstract</i>	III
<i>Résumé</i>	IV
<i>List of abbreviations</i>	VI
<i>Table of contents</i>	VII
1. Introduction	1
1.1 The analysis of biomolecules by gas-phase techniques	1
1.2 Glycans, their importance and challenges	1
1.3 State of the art of glycan analysis and ongoing development	4
1.4 Fragmentation of glycans	7
1.5 Theme of this research	9
2. Experimental approach	11
2.1 A tandem mass spectrometer for cryogenic spectroscopy of gas-phase molecular ions	11
2.2 Addition of a SLIM-based ion mobility stage to the tandem mass spectrometer for cryogenic spectroscopy of gas-phase molecular ions	14
2.2.1 Ion funnel trap	15
2.2.2 Travelling wave IMS implemented by SLIM	16
2.2.3 SLIM based ion guide and CID region	19
2.2.4 Electronics	20
2.2.5 Detection of ions in the SLIM IMS section and ion guide	20
2.2.6 Performance of the SLIM-IMS module	21
3. Collision-induced dissociation of sodiated glycans	25
3.1 Fragmentation of the glycosidic linkage	25
3.2. Center-of-mass reference frame	26
3.3 Mean free path and the effects of pressure	27
3.4 Collisional activation and the two-step process	29
3.5 Unimolecular dissociation and RRKM theory	30
3.6 Competitive pathways and ion relaxation	31
3.7 Closing comments	32
4. Anomeric retention of glycan C-type fragments	33
4.1 Introduction	33
4.2 Experimental approach	34
4.3 Mass spectra of CID fragments	34
4.4 Cryogenic infrared spectrum of a monosaccharide	36
4.5 Spectroscopic investigation of the anomeric retention of C fragments	37

4.6 Spectroscopic identification of an ambiguous fragment	41
4.7 Conclusions	41
<i>5. A new glycan sequencing strategy coupling ion-mobility-selected CID and messenger-tagging IR spectroscopy</i>	<i>43</i>
5.1 Introduction	43
5.2 Experimental approach.....	44
5.3 Spectroscopic study Y fragments generated by CID of mobility-selected precursors.....	44
5.3.1 Disaccharide Gal(β -4)GalNAc.....	45
5.3.2 Trisaccharide MAN-1.....	47
5.3.3 Tetrasaccharide LNNt.....	50
5.3.4 Pentasaccharide maltopentaose.....	51
5.4 Comparison of mobility-separated disaccharides to their permethylated standards.....	54
5.5 Conclusions	56
<i>6. Unravelling the structures of sodiated β-cyclodextrin and its fragments.....</i>	<i>58</i>
6.1 Introduction	58
6.2 Methods.....	60
6.2.1 Experimental Details	60
6.2.2 Computational approach.....	60
6.3 Results and Discussion	61
6.3.1 CID mass spectrum.....	61
6.3.2 Ion mobility and cryogenic IR action spectra of sodiated α -CD and β -CD.....	63
6.3.3 Cryogenic IR spectra of CID fragments	66
6.3.4 Comparison with Theory	68
6.4 Conclusions	73
<i>7. Conclusions</i>	<i>75</i>
<i>Appendix: Fragmentation mechanisms, calculated spectra, and relative energies of the candidate fragment ion structures of β-cyclodextrin</i>	<i>78</i>
<i>Acknowledgements.....</i>	<i>82</i>
<i>Curriculum Vitae</i>	<i>85</i>
<i>Robert Pellegrinelli.....</i>	<i>85</i>
<i>Bibliography.....</i>	<i>88</i>

1.Introduction

1.1 The analysis of biomolecules by gas-phase techniques

The function of biomolecules in living organisms is closely related to their structure, which is why a considerable amount of time and effort has been devoted to unravelling their architecture. Of the various techniques proposed to unravel biomolecular structure, gas-phase techniques have proven to be extremely useful due to their high sensitivity and selectivity. Isolating an analyte molecule from its solution environment facilitates its detection and identification by allowing measurements to be made on the bare molecule without clouding from the environment. This is one of the key advantages of gas-phase techniques, where rapid identification of and primary structure determination of biomolecules become possible. This ability to rapidly provide information on biomolecules has greatly increased with the invention of soft ionization techniques such as electrospray ionization (ESI)¹ and matrix-assisted laser desorption (MALDI)², which have allowed for the seamless transfer of large, intact biomolecules into the gas phase.

As a result, structural studies of isolated peptides, lipids, nucleic acids, and glycans has become possible, allowing to analyze the linkage and composition of these molecules with unprecedented rapidity and detail, revolutionizing the fields of metabolomics,³ genomics, and proteomics.⁴ Mass spectrometry (MS)-based protein sequencing methods make use of the easy detection fragment masses to re-construct the full peptide sequence. The high sensitivity MS-based methods has led to the detection of slight changes in metabolite levels as indicators for diseases such as cancers,⁵⁻⁷ cardiovascular diseases,⁸⁻⁹ and inborn errors of metabolism.¹⁰⁻¹² Improvement of ambient ionization methods has allowed for in vivo and in situ MS imaging along various dimensions,¹³ lipid profiling in different layers of tissue sample,¹⁴⁻¹⁵ and the imaging of proteins in a three-dimensional sample volume.¹⁶ The development of action spectroscopy has allowed for spectroscopic studies of gas-phase biomolecules to be performed, providing a whole new approach to identification and structure determination.¹⁷

In this work, we cover the application of gas-phase techniques to the complex field of glycomics, and present the latest innovations for glycan structure elucidation, based on fragmentation in the gas phase.

1.2 Glycans, their importance and challenges

Glycans are compounds consisting of monosaccharides linked together by glycosidic bonds, which play a central role in many biological processes. Most proteins on cell surfaces are heavily glycosylated, resulting in almost all living cells being covered by a “forest” of glycans called the glycocalyx (Figure 1.1). These mediate both intrinsic and extrinsic recognition between cells and external entities.¹⁸⁻²⁰ Blood group type and organ-donor compatibility²¹, and immune response to pathogens¹⁹ are all strongly influenced by glycans. The processes by which viruses gain access to host cells and escape

immune detection are also principally mediated by glycans on viral surfaces, which help to “unlock” host cells and mask certain features recognized by the immune system.²²⁻²⁴ For example, recent studies on the SARS-CoV-2 spike protein has shown that a number of N-linked glycans contribute to its folding as well as helping in immune evasion.²⁵⁻²⁶ In one way or another, glycans are implicated in virtually all major human diseases. In order to gain a better understanding of these processes and propose effective and targeted solutions, it is essential to understand the structure of glycans, which is directly related to their physiological functions.

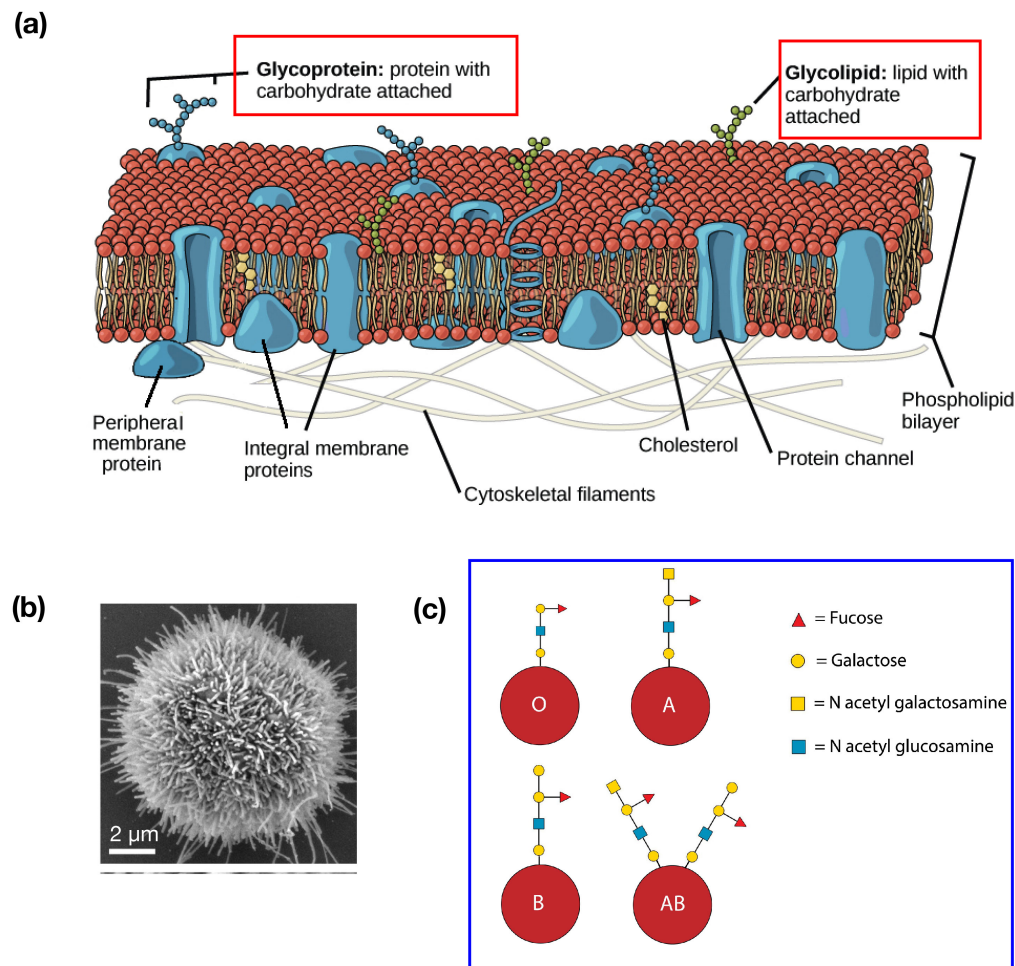


Figure 1.1: Illustration of a cell membrane with glycoproteins and glycolipids highlighted on the cell surface, reproduced with permission from reference²⁷ (a). Scanning electron microscopy image of the glycocalyx of a cell, reproduced with permission from reference²⁸ (b). Illustration of how glycans are responsible for blood group type (c).

Despite being of fundamental importance in biological processes, deciphering glycan primary structure is complex. This complexity arises from both their biosynthetic pathways and their inherent chemical structure. Glycan synthesis is not a template-driven process, but rather relies on the presence and concentration of enzymes that link monosaccharides together. While the presence of such enzymes is determined by genes, their concentrations depend on the cellular environment,

which can greatly vary from cell to cell. This results in a large heterogeneity in the glycosylation of proteins, for example, with each glycosylation site having the possibility of hosting different glycans.

To fully appreciate the complexity of glycans, it is necessary to understand the basics of glycan structure. We take the example of glucose (Figure 1.2). In solution, glucose exists as an equilibrium between its open-chain and cyclic forms, but in aqueous solutions, over 99% of glucose is in a cyclic pyranose form (Figure 1.2a). The carbon atoms are labelled C-1 through C-6, with the C-1 being part of the aldehyde group in the open-chain form. The C-1 hydroxyl group is the most labile due to the electron-donating effect of the adjacent oxygen and is called the anomeric OH. This OH group exists in either axial or equatorial configurations in the pyranose form, producing α and β anomers (Figure 1.2b), which interconvert in solution through a process called mutarotation.²⁹ The equilibrium for glucose is 36% α and 64% β at room temperature. When forming polymers, the unit containing a free anomeric OH is called the reducing end, while the other extremity is referred to as the non-reducing end (Figure 1.2c). Every reducing sugar will therefore possess a racemic mixture of reducing anomers, resulting from the anomeric OH being in the α or β configuration according to thermodynamic equilibrium.

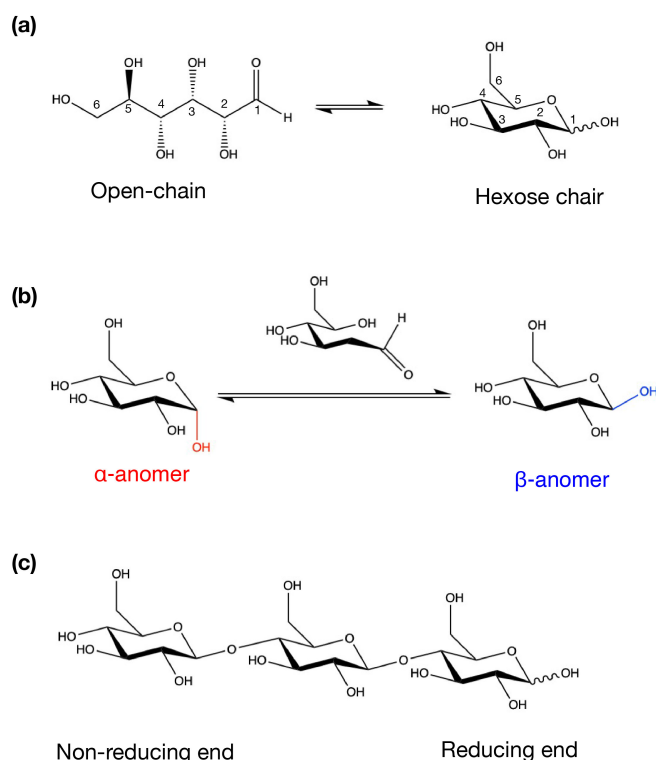


Figure 1.2: The basics of glycan structure taking glucose as an example. (a) carbon numbering and the typical ring-structure of a monosaccharide, (b) different anomers due to the position of the reducing end OH group, (c) designation of reducing and non-reducing end in a glucose polymer.

The complexity of glycan structure is further rooted in the fact that many of the monosaccharides, which are the building blocks of glycans, differ only in the stereochemistry around an asymmetric carbon atom (Figure 1.3a). Moreover, when a glycosidic linkage is formed at the anomeric carbon (C-1), it can adopt either an α or a β configuration resulting in different anomers (Figure 1.3b).

Furthermore, glycosidic linkages can be formed at different hydroxyl groups, giving rise to a multitude of regioisomers and branched structures, all of which can have equivalent monosaccharide content and molecular mass (Figure 1.3c). The combination of all these various types of isomerisms leads to an enormous number of possible primary structures for a glycan of a given mass. For example, a glycan comprised of six monosaccharide units can exist in any one of 1×10^{12} different isomeric forms,³⁰ each of which will have different properties. Because of this isomeric complexity, the structural determination of glycans remains a challenging yet, undeniably important task.

In the context of this work, the SNGF notation for drawing glycans is used.³¹ This shorthand allows the simple representation of complex glycan structures as a series of colour-coded symbols joined by straight lines, representing the glycosidic linkages, over which the anomericity and linkage position are indicated. The glycosidic linkage is always assumed to originate from the C-1, except for 2-ketoses which originate from C-2. A small glossary of the common monosaccharides used in this work is presented in the inset of Figure 1.3.

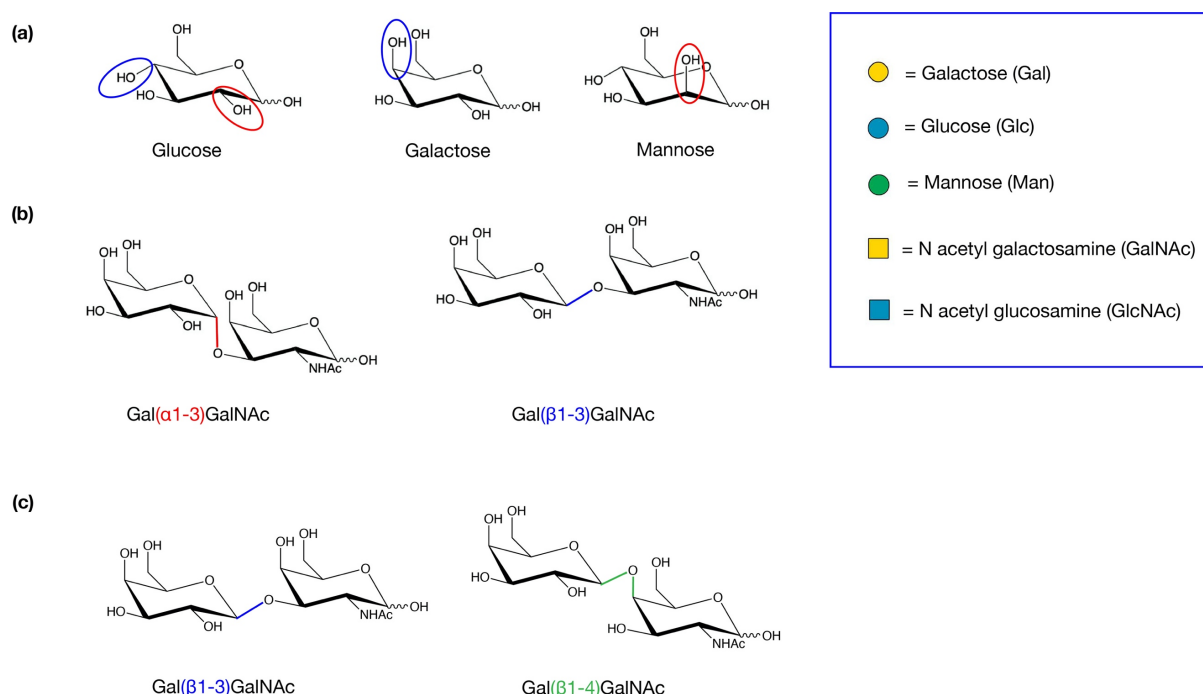


Figure 1.3: Structural complexity of glycans, with the illustration of (a) isomeric monosaccharides, (b) glycan anomers, (c) regioisomers. Inset: abbreviations of common monosaccharides used in this work.

1.3 State of the art of glycan analysis and ongoing development

Due to the complex nature of glycans, direct measurements of the molecular structure may seem to be the best option. X-ray crystallography is such a direct measurement, that has been used to measure glycan structure to a limited extent.³² The limitation of X-ray crystallography arises from the fact that most glycans do not crystallize, most likely due to their flexible nature, making it less likely for them to pack uniformly into a crystalline structure. Nuclear magnetic resonance (NMR) spectroscopy is the

most widely used technique when an absolute structural characterization of a molecule is necessary. This has been used to determine the structure of glycans with a high degree of precision,³³⁻³⁵ and ¹H NMR is commonly used by carbohydrate suppliers to validate their products. Although both techniques can potentially provide all the details on glycan structure, they require considerable amounts of sample, making them unsuitable for analytical purposes.

Analytical techniques that separate molecules based on their structure and physical properties have gained traction for the study of glycans. Capillary electrophoresis (CE), which separates charged molecules based on their migration time between two electrodes, has been used to separate and identify glycans.³⁶ Typically, glycans are chemically labelled by a charged, fluorescent label, which plays the double role of ensuring good mobility in the electric field and of providing easy UV detection.³⁷ A ladder of standards, consisting of increasingly large polysaccharides, have been used to estimate the size, monosaccharide content and structure in CE studies of glycans.^{36, 38} High-pressure liquid chromatography (HPLC) separates molecules based on their affinity to a stationary phase inside a column and characterizes them by their retention times. Much like CE, glycans can be functionalized with a fluorescent label and detected optically as they elute from the chromatographic column.³⁹ The use of enzymes, typically exoglycosidases, which can cleave specific types of glycosidic bonds from the non-reducing end, has been used in conjunction with CE and HPLC techniques to provide a complete glycan sequencing strategy, capable of determining monosaccharide content, linkage position, and anomericity to a high degree of accuracy.⁴⁰⁻⁴⁴ Although powerful, these approaches are time-consuming and labour intensive, with separation runs taking tens of minutes and enzymatic digestions often taking hours, and cannot always resolve all types of isomerism. This beckons the development of faster, simpler, and more structurally sensitive methods for glycan analysis.

Mass spectrometry (MS), which distinguishes ions based on their mass to charge ratio (m/z), is the most widely used technique for glycan analysis due to its speed and sensitivity.⁴⁵⁻⁴⁷ Although simple MS is unable to distinguish between glycan isomers, tandem mass spectrometry (MS^n), which consists of breaking a mass-selected parent ion and detecting the fragments, has been able to provide structural insights into complex glycans, based on the identification of particular fragments or fragmentation patterns.⁴⁸⁻⁵⁰ Recently, tandem mass spectrometric techniques have unraveled many structural details such as linkage position, branching, and in some cases the anomericity of small glycans.⁵⁰⁻⁵² Even so, MS^n alone is unable to distinguish between all the isomers and isomeric fragments formed when studying glycans. It has therefore been coupled to separation techniques such as HPLC, providing hybrid methods that have allowed many glycan isomers to be separated and identified based on their retention times and MS patterns.^{42-43, 53} Schemes have been developed in which a glycan sample is treated by arrays of enzymes which cleave specific glycosidic bonds, and the products are then separated by HPLC and analyzed by tandem MS.^{42, 54-55} Such methods are very powerful, with the ability to fully sequence large oligosaccharides. However, they often require chemical labeling of the glycans, long incubation times, and multiple chromatographic runs, making them complex and time consuming. This leaves the floor open to faster, more direct separation techniques to be partnered to MS^n analysis.

Ion mobility spectrometry (IMS) separates ions moving through an electric field in the presence of an inert gas. This separation is based on the collisional cross section (CCS), which is specific for each compound and drift gas. Many different types of ion mobility exist, the most common of which are

drift tube IMS (DTIMS), field asymmetric IMS (FAIMS), and travelling wave IMS (TWIMS).⁵⁶ Ion mobility has been coupled to MS analysis, adding the ability to separate isomeric and isobaric species that could not be resolved by MS, giving rise to many different hyphenated IMS-MS techniques.⁵⁷ Adoption of these techniques for the study of biomolecules has provided a new and powerful way to separate and probe different molecular conformations.⁵⁸ A few examples include the direct measurement of protein folding as a function of pH and temperature,⁵⁹⁻⁶¹ separation of chiral amino acids,⁶² and the assembly of viruses,⁶³ and the separation and distinction of isomeric glycan structures.⁶⁴⁻⁶⁵

Ion mobility has recently been coupled with MSⁿ techniques for the study of glycans, separating isomers on the millisecond timescale, and thus providing an attractive and novel alternative to HPLC.⁶⁶⁻⁶⁸ Glycans of different monosaccharide content, as well as regioisomers and anomers with the same monosaccharide content have been identified using IMS-MSⁿ.^{67, 69-76} The development of structures for lossless ion manipulation (SLIM) allows for ion mobility to be performed on very long serpentine drift paths, traced out by electrodes on a pair of mirroring printed circuit boards.⁷⁷⁻⁷⁹ Studies of glycan fragments generated by tandem MS and combined with IMS have led to the identification of regioisomers and anomers of the parent glycans based on different arrival time distributions (ATDs) of the fragments.⁷¹⁻⁷² Implementation of such SLIM-based technology has allowed for unprecedented resolution on relatively compact instruments, which can easily separate different isomeric glycans, and even sub-structures within a single glycan.⁸⁰ Nevertheless, IMS is still unable to distinguish most subtle structural differences common to many isomeric glycans. Moreover, IMS has difficulty assigning a separated drift peak to a specific primary structure.

Thus, while IMS can answer the question, “How many structures are there?”, the question, “What are these structures?” is more difficult to answer.

Another approach to for glycan analysis is to use vibrational spectroscopy. Molecular spectra are sensitive to the slightest change in molecular structure. This can be particularly useful for analysing molecules with intrinsically complex structures, such as glycans. Room temperature vibrational spectroscopy, combined with MS² and IMS techniques, have been used to gain detailed structural information and identify epimers and anomers of small glycans.^{72, 81-87} However, this approach is limited, as the spectra of larger glycans tend to be too congested at room temperature to be used as identifiers. Cooling molecules to cryogenic temperatures eliminates inhomogeneous broadening,⁸⁸ substantially improving spectral resolution and cryogenic messenger-tagging IR spectroscopy has enabled the fingerprinting of glycans of increasing size and isomeric complexity to be identified based on their IR spectra.⁸⁹⁻⁹⁴ Combining ion mobility with cryogenic IR spectroscopy provides a formidable tool for identifying different glycan isomers, and the recent integration of ultra-high resolution SLIM-based IMS has allowed for various glycan isomers to be separated and their spectra recorded individually,^{89,91} revealing minor structural differences, even in glycans containing up to ten monosaccharides.⁹²⁻⁹³ Although cryogenic IR spectroscopy can be used to identify large and complex glycans, it cannot infer the primary structure from the spectrum alone. Most glycans are too large to be accurately treated by quantum mechanical calculations, which are needed to assign experimental spectra to molecular geometries. If we wish to use spectroscopy to analyse glycan structure, we must have either one of two things:

1. A reference spectrum for every naturally occurring glycan structure (isomer, anomer, open ring form, etc.)
2. A method to break the glycan of interest into smaller glycan structures for which the associated spectra are known in such a way that the parent structure can be reconstructed.

While a database of spectra for every single glycan structure does not yet exist, such a spectral database can be constructed if we possess a set of common, small glycans for which their IR spectra and associated structures are known. This will form an initial spectroscopic database. If we then fragment larger glycans into those contained in our initial database without losing structural information of the parent upon fragmentation, we can then identify the exact primary structure of the parent glycan and add its IR spectrum to the database. The database can thus be progressively expanded to larger, more complex glycans, ultimately resulting in every common glycan structure being associated to an IR spectrum, which opens the door to using spectroscopy as a rapid and easy means of glycan identification.

1.4 Fragmentation of glycans

Fragmentation of gas phase ions by various techniques in tandem mass spectrometry (illustrated in Figure 1.4), which has been a valuable tool for the structural elucidation of peptides and proteins, has also proven to be a powerful method to probe and identify glycan structures.⁹⁵

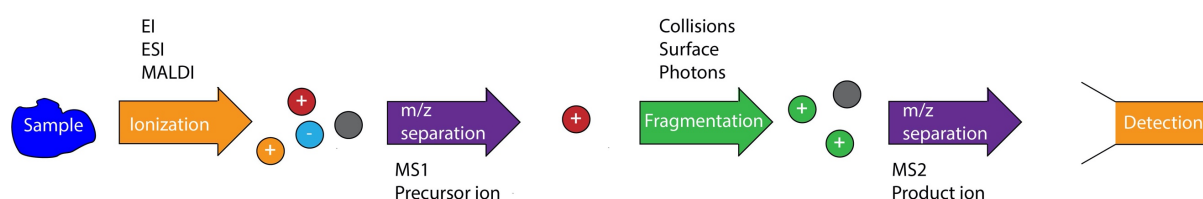


Figure 1.4: General workflow of fragmentation processes used in an MS² study.

Of these fragmentation techniques, collision-induced dissociation (CID) is the most frequently used. The fragments produced by CID principally come from glycosidic bond cleavages and provide information on glycan sequence and branching.⁹⁶ Cross-ring fragments, resulting from the breaking two bonds in the sugar ring, occur less frequently and require higher collision energies. When formed however, these fragments conserve the glycosidic bond and can therefore provide information on linkage positions and bond anomericity.^{51, 97-98} For this reason, various electron dissociation methods such as electron capture dissociation (ECD), electron transfer dissociation (ETD), and electron detachment dissociation (EDD) have been used to produce cross-ring fragments not formed by CID and in larger abundances, providing more information on glycan structures.⁹⁹⁻¹⁰¹ Although less commonly used, IRMPD also allow the generation of more cross-ring fragments not always accessible by CID.¹⁰²

The nomenclature for the fragmentation of glycans was first proposed in 1988 by Domon and Costello and follows that used for peptides.¹⁰³ Fragments containing the non-reducing end are labelled A_m, B_m, and C_m, while fragments containing the reducing sugar unit are labelled X_n, Y_n, and Z_n. Subscripts

indicate the position in the glycan chain relative to the reducing end, and superscripts are used for cross-ring fragments to indicate which bonds are cleaved within the carbohydrate ring, as illustrated in Figure 1.5. The different fragments carry different information about the precursor molecule. While the C and Y fragments are themselves intact glycans, principally used to identify the monosaccharide content and branching,¹⁰⁴⁻¹⁰⁵ the B and Z fragments are intact saccharides from which an H₂O has been eliminated (-18 a.u.). This points to an extra degree of unsaturation, predicted to be in the form of a ketone or an ahydro structure.^{83, 106} The A and X fragments come from cleaving two bonds in the glycosidic ring. These fragments appear to be strongly dependant on the type of glycosidic linkage, which is preserved during this kind of fragmentation, making them useful indicators of anomericity and linkage position,^{51, 97-98} although they often require high-energy CID or other processes such as electron capture dissociation.^{49, 99-101, 107-108}

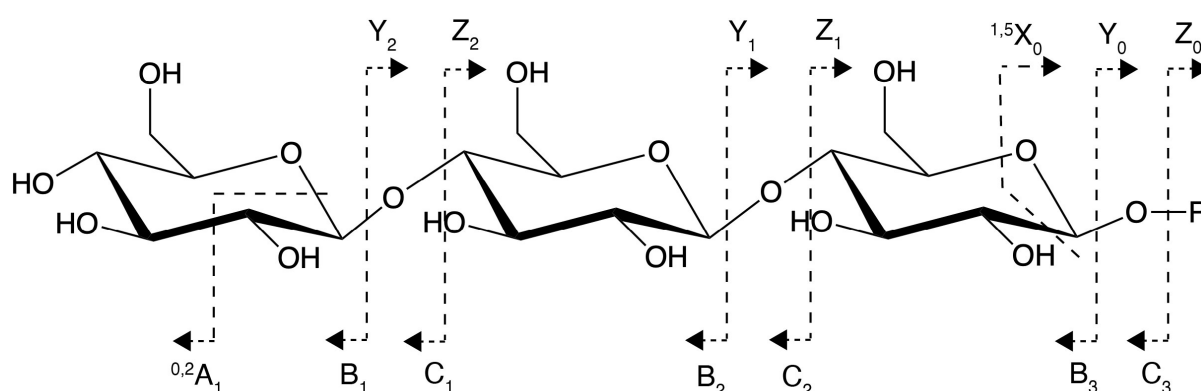


Figure 1.5: Domon and Costello nomenclature for glycan fragments.¹⁰³ The C and Y fragments carry a hydrogen making them intact glycans.

Chemical modification such as permethylation of the free hydroxyl groups before fragmentation helps locate the position of the glycosidic linkages in the precursor molecules.^{99, 109} Recently, software developments have increased the automation of structure prediction based on fragment analysis.¹¹⁰ Nevertheless, some structural information is often lost upon fragmentation, which is why CID can be combined with ion mobility to get a better understanding of how to relate fragments to parent structures, as discussed in the previous section.^{67-68, 70-73}

The nature of the precursor glycan ion plays a key role in determining which fragments will be formed by a given dissociation method. Protonated and deprotonated glycans fragment very differently, with the former producing mainly B_n and Y_n ions, while the fragmentation patterns of the latter seem more molecule-dependant.⁴⁶ Forming adducts between glycans and polyatomic anions or metal cations allow for a greater control over the fragmentation pathways. It has been reported that CID studies on N-glycan-nitrate adducts predominantly produced C-type fragments,¹⁰⁴⁻¹⁰⁵ while metal cation-adducts seem more prone to cross-ring fragmentation.^{46, 48, 95} All the fragmentation studies presented in this work were performed on positively and singly charged glycans, either by addition of a proton or by complexation to a singly-charged metal cation.

Very recently, the combination of CID with IR spectroscopy has shown that C fragments from alkali metal-complexed disaccharides retain the anomericity of the glycosidic bond in their reducing end OH.⁸² One of the goals of the work presented in this thesis is to investigate the generality of the anomeric retention of C fragments for larger and more complex glycans and is presented in Chapter 4. Furthermore, we explore how the IR spectra of Y fragments, generated from mobility-resolved glycans can be used to identify the reducing anomers of the precursor molecule (Chapter 5). This ongoing work indicates that IR spectroscopy combined with CID can add a powerful new dimension to glycan analysis and reveal structural details that were until now obscured.

1.5 Theme of this research

For over a decade, the Rizzo research group has pioneered spectroscopic studies of biomolecules in the gas phase. With earlier works mainly performed on peptides, the focus shifted to glycans in 2017, when Masellis *et al* performed the first mobility-selected cryogenic IR spectra of disaccharides, using a 2 meter drift tube to get mobility separation and messenger tagging for spectroscopic detection.^{89, 111} Since then, ultra-high resolution ion mobility based on SLIM technology has been implemented, allowing for more detailed studies to be performed on glycan isomers and anomers.^{91-92, 112}

A key contributing factor to our success in studying large biomolecules has been cryogenic spectroscopy. Cooling ions to cryogenic temperatures before taking their IR spectra greatly improves the spectral resolution by eliminating inhomogeneous broadening, i.e. the broadening due to the thermal population of rovibrational states and the presence of multiple conformers that are populated at room temperature. Moreover, using messenger-tagging spectroscopy ensures that the action spectra obtained are from a single-photon process, which ensures their linearity and robustness. Unlike multiple photon spectroscopy, as soon as a single photon is absorbed the tag boils off and the product ions are detected. This avoids inherent broadening common to multiple photon spectroscopy, further enhancing spectral resolution.

The work performed for this thesis employs the state-of-the-art techniques, associating collision-induced dissociation with cryogenic messenger-tagging IR spectroscopy and ultra-high resolution ion mobility, to study the fragmentation of positively charged glycans. We present the experimental approach used to perform this research and give a detailed view on recent upgrades made on to the main instrument that has been used throughout this thesis in Chapter 2. The theory behind collisional activation and unimolecular dissociation applied to a glycan ion are discussed in Chapter 3. The following chapters elaborate how cryogenic IR spectroscopy and ultra-high resolution ion mobility can be combined with CID to study C and Y fragments of linear and branched oligosaccharides, providing unprecedented structural information, unambiguously identifying the anomericity of glycosidic bonds as well as fingerprinting reducing-end anomers. These lay the cornerstones to building a spectroscopic glycan database, in which every glycan structure has an associated fingerprint spectrum. This database can be grown to include ever larger glycan structures until a point where ultimately, every naturally occurring glycan structure can be identified by matching its spectrum to an entry in the database.

In the last chapter, we study the fragmentation of β -cyclodextrin, an important cyclic oligosaccharide. Theoretical calculations performed on the fragments formed were compared to experimental data,

giving useful insights into the structure of the fragments, and potential fragmentation mechanisms. The relevance of this work in the context of the development of glycomics are discussed in the conclusions, as well as future directions.

2. Experimental approach

A home-built tandem mass spectrometer equipped with a cryogenic ion trap was used to perform the majority of the experiments discussed in chapters 4 and 6, and is presented here. The original instrument was tuned to produce glycan fragments by collision-induced dissociation (CID), which were then investigated by cryogenic infrared (IR) spectroscopy. An additional ultra-high resolution ion mobility stage was later added to this instrument, allowing to perform mobility selection of ions before CID and spectroscopic interrogation. The addition and characterization of this mobility stage is described in the second part of this chapter and this new setup was used to perform the experiments described in chapter 5.

2.1 A tandem mass spectrometer for cryogenic spectroscopy of gas-phase molecular ions

A home-built tandem mass spectrometer,¹¹³ equipped with a cryogenic octupole ion trap was used in this work is schematically shown in Figure 2.1.

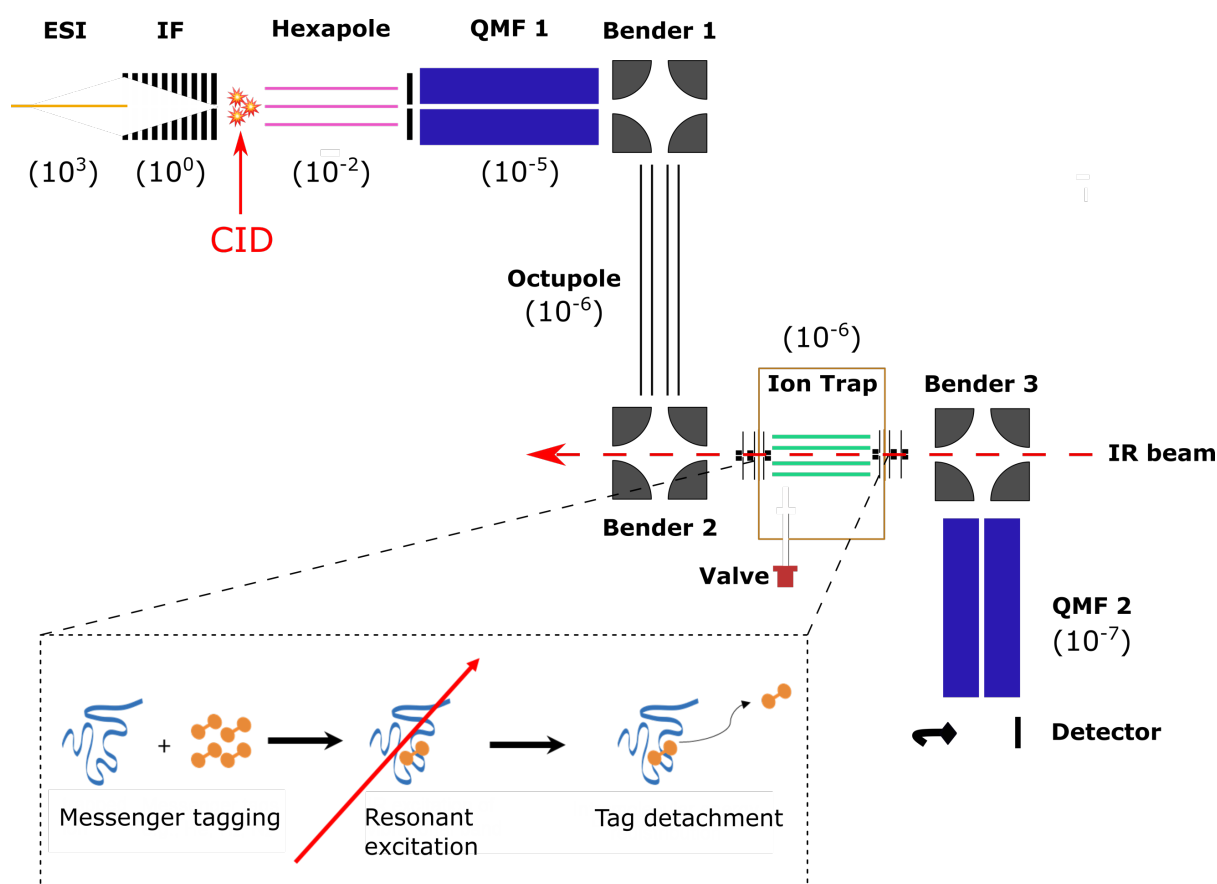


Figure 2.1: Schematic representation of the tandem mass spectrometer, setup to obtain cryogenic messenger-tagging IR spectra of mass-selected molecules and CID fragments. Pressures, in mBar, are indicated in parenthesis for the various differentially pumped sections. Inset: IR messenger-tagging spectroscopy.

Gas-phase ions are produced by nano-electrospray ionization (nESI) from a solution in which the analyte is dissolved, typically in a mixture of water and methanol. The concentration of analyte used ranges between 50 and 100 μ M, and the flow rate is \sim 100 nL/min. The ions are radially confined in a home-built ion funnel, equipped with a jet disruptor to block droplets coming from the source, reducing the pumping load on the next stage.¹¹⁴ The continuous stream of ions is accumulated in a hexapole ion trap and released as short ion pulses at a 10 Hz frequency by switching the hexapole exit lens from high to low voltage. The ion pulse is sent through a first quadrupole mass filter and guided to an octupole ion trap. The original setup used a 22-pole ion trap which was replaced by the current octupole to achieve better focusing of ions along the central axis.¹¹⁵ The trap is maintained at cryogenic temperatures by a closed-cycle cryogenic cooler and a resistive heater. Here, ions are cooled by collisions with a cold buffer gas containing a mixture of helium and nitrogen, which is pulsed into the trap several milliseconds before the ions arrive. Upon cooling, the ions form weakly-bound complexes with nitrogen molecules, which serve as “tags” to monitor photon absorption. The tagged ions in the trap are then irradiated every second trapping cycle by a pulse of IR photons generated from a Nd:YAG pumped, tunable optical parametric oscillator (OPO, LaserVison). They are extracted through a second quadrupole mass filter and detected on a channeltron.

When the IR photon is in resonance with a vibrational transition of the tagged ion, the ion is excited to a higher vibrational state before redistributing the energy intramolecularly among its vibrational modes. This process causes the dissociation of the nitrogen tag, and the IR spectra is obtained by monitoring the depletion of the tagged ion mass as a function of IR wavelength in a *laser-on /laser-off* experiment (Figure 2.1 inset).

The conditions of the cryogenic trap are tuned to achieve mostly singly N₂ tagged species as shown for the singly sodiated monosaccharide GalNAc- α -OMe in Figure 2.2. This is to prevent the scenario where a higher-order tagged species loses all but one of its tags upon IR irradiation, hence resulting in an increase of singly tagged species and an observed gain at the resonance transition. It is interesting to note that for this molecule, the distribution of tags appears to be truncated and a maximum of only two N₂ tags are observed. This is likely due to a limited number of binding sites for the N₂ tag on this relatively small molecule.

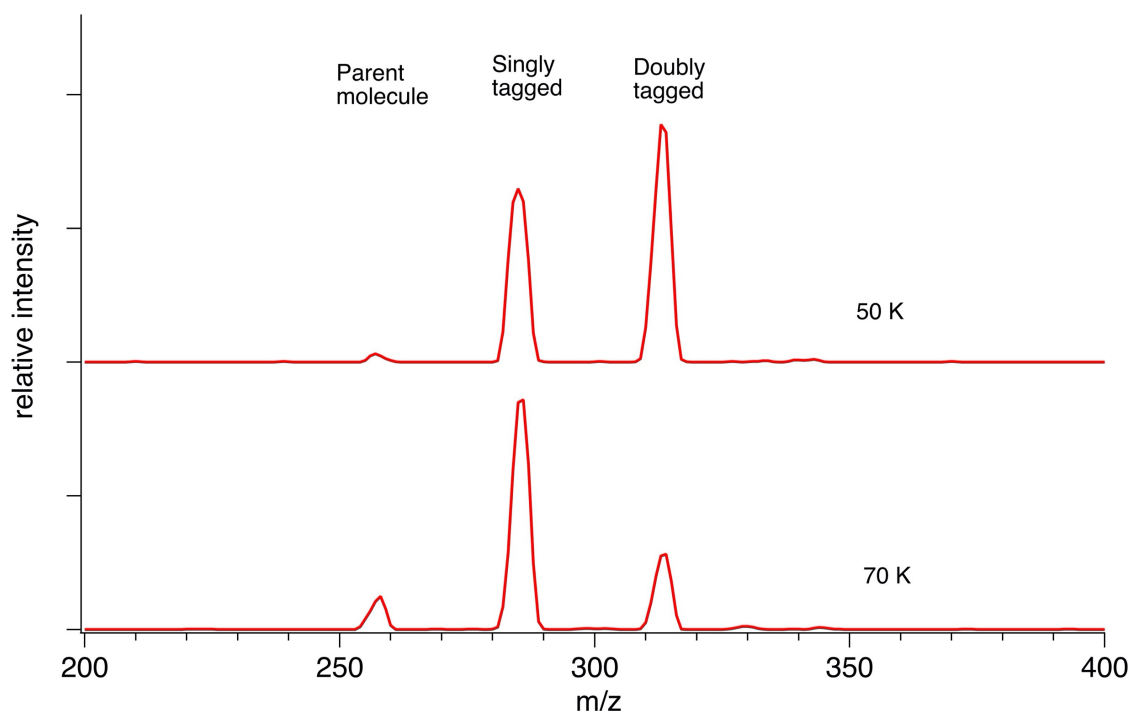


Figure 2.2: Mass spectra of the N_2 -tagged, sodiated GalNAc- α -OMe at 50 K and 70 K. The higher temperature favors the formation of singly tagged species and is used to measure IR spectra.

Collision-induced dissociation is achieved by accelerating ions from the funnel into the hexapole with a potential difference typically ranging between 100 and 270 V. The collisions occur in the hexapole with residual molecules at $\sim 10^{-2}$ mbar, and the collision energy can be tuned by adjusting the potential difference between the ion funnel exit and hexapole bias. The fragmentation process will be discussed in more detail in Chapter 3. Figure 2.3 illustrates fragmentation spectra of a sodiated tetrasaccharide with increasing potential difference. These MS spectra were obtained by running the first quadrupole mass filter as a simple ion guide and scanning the mass selection of the second quadrupole mass filter. At a potential difference of 100 V, the parent is the predominant species, while the formation of fragments from breaking the glycosidic bonds as well as cross-ring fragments become more abundant as the voltage is increased. The first quadrupole mass filter can then be used to select any of these fragments for further spectroscopic investigation. Fragments observed show resemblances to those reported on recent MS^n studies of similar metal-complexed oligosaccharides.^{108, 116}

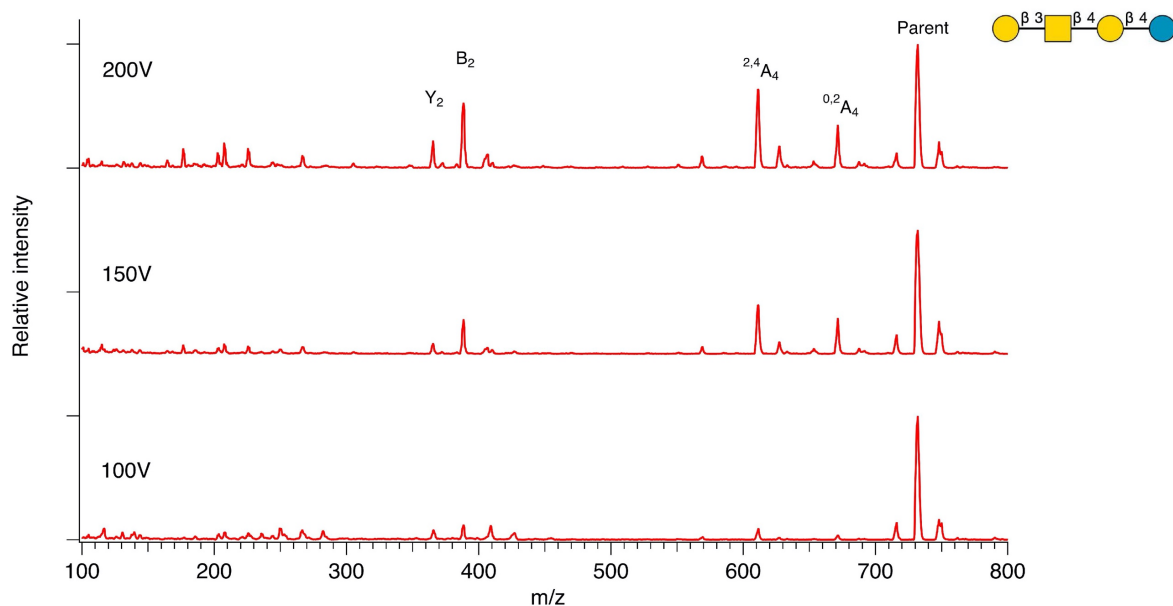


Figure 2.3: MS² spectra of the tetrasaccharide $[\text{Gal}(\beta\text{-3})\text{GalNAc}(\beta\text{-4})\text{Gal}(\beta\text{-4})\text{Glc}]\text{Na}^+$ with 100, 150 and 200V potential difference between the ion funnel and hexapole. Identified CID fragments are labelled.

2.2 Addition of a SLIM-based ion mobility stage to the tandem mass spectrometer for cryogenic spectroscopy of gas-phase molecular ions

In order to perform separation of ions prior to fragmentation and/or spectroscopy, an ion mobility device, was designed and built in our lab, was added to the tandem mass spectrometer described in the previous section. This device uses traveling wave (TW) ion mobility and was implemented by structures for lossless ion manipulation (SLIM) technology, developed initially by Richard Smith and coworkers.⁷⁷⁻⁷⁸ As mentioned in the introductory chapter, such SLIM-IMS devices have been recently shown to achieve ultra-high resolution, separating molecules with minor structural differences, including glycan isomers and anomers.^{80, 91} The fact that ions can be turned 90° on these SLIM-IMS devices allow for very long drift paths to be achieved on a relatively compact device, and the use of TW to move the ions through the drift gas makes for a low voltage device, as opposed to kV power supplies associated with the classical DC drift tube.

The addition of such a technology to our existing instrument allows us to separate specific glycan isomers or anomers prior to CID and cryogenic spectroscopy experiments. These targeted experiments, performed on an isolated glycan structure, allow us to characterize its fragmentation and obtain its spectral fingerprint which can be added to the spectroscopic database, allowing it to be rapidly identified in future experiments.

A schematic view of the instrument is shown in Figure 2.4, with more detailed information on specific parts in the following sub-sections. Ions of interest are generated by nano-electrospray ionization (nESI), accumulated and trapped in an ion funnel, then released as packets into the SLIM-IMS region for separation. The SLIM-IMS region is filled with a drift gas, typically helium, between 1.5 and 2.5 mbar. After traversing the IMS region, mobility-separated ion packets are conducted through a differentially pumped region by a planar RF guide with a constant DC gradient. An ion lens at the next

conductance limit can be used as a gate to slice out particular ion packets by their arrival times. The ions then pass through a hexapole ion guide before arriving at a mass-selecting quadrupole (Q1). An RF octupole guide with a DC quadrupole bender on either end directs the mass- and mobility selected ions into a cryogenic octupole trap, where messenger-tagging IR spectroscopy is performed. A third DC bender and a second mass-selecting quadrupole with a channeltron detector are used to detect the tagged and untagged species.

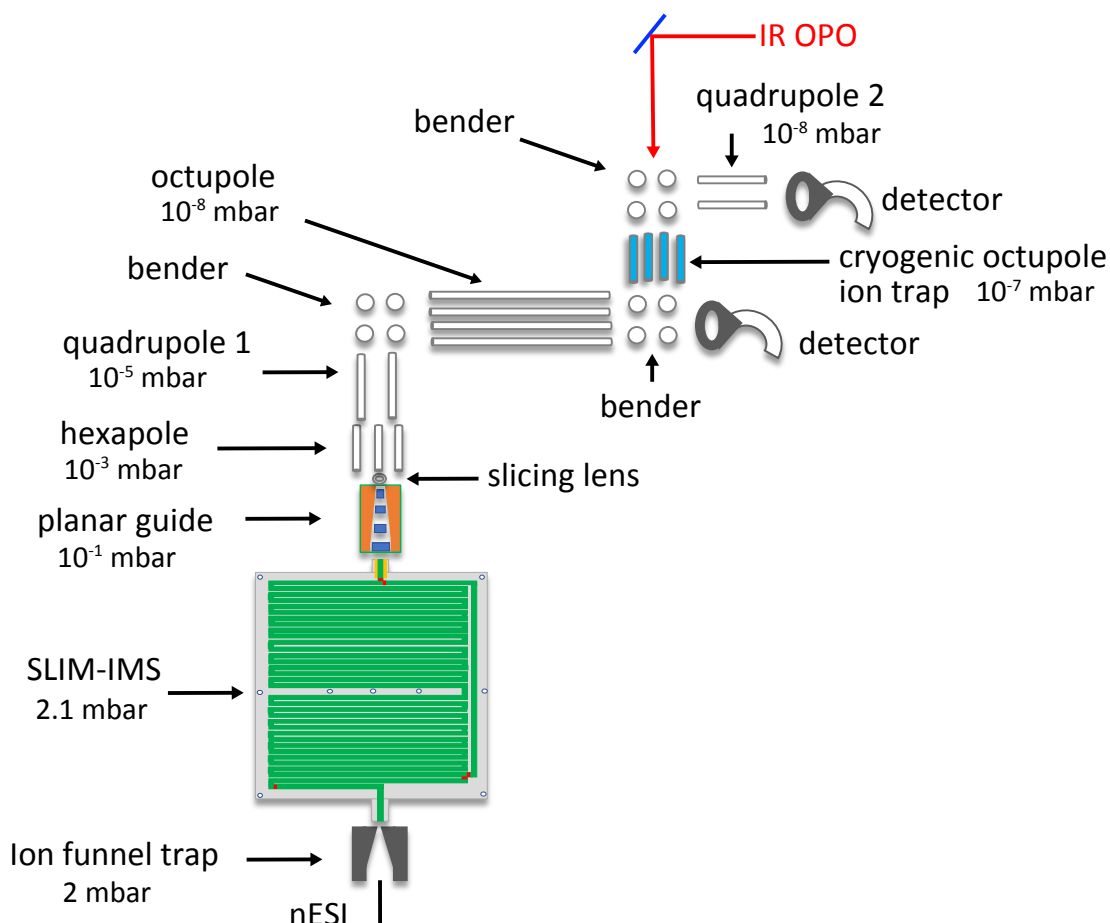


Figure 2.4: Schematic of the instrument in which SLIM-IMS is coupled to a tandem mass spectrometer with a cryogenic ion trap. Typical pressures for each differentially pumped section are indicated.

2.2.1 Ion funnel trap

To generate an ion packet from the continuous nESI source, two grids were added to a home-built ion funnel,¹¹³ as shown in Figure 2.5. Thus, the space between grid2 and the end electrode is used as a trap to accumulate the ions and produce a short pulse for IMS separation.¹¹⁷ Typical voltages for V_{in} , V_{grid1} , V_{grid2} , and V_{out} are given in Table 2.1. The voltage on the last funnel electrode, V_{end} , is set to 275 V for a period of 99.5 ms to trap the ions and then lowered to 250 Volts for 0.5 ms to release them into the subsequent IMS separation path. We thus run the experimental cycle at 10 Hz, which is

compatible with the repetition rate of the pulsed optical parametric oscillator that generates infrared pulses for spectroscopic interrogation of the ions further downstream.

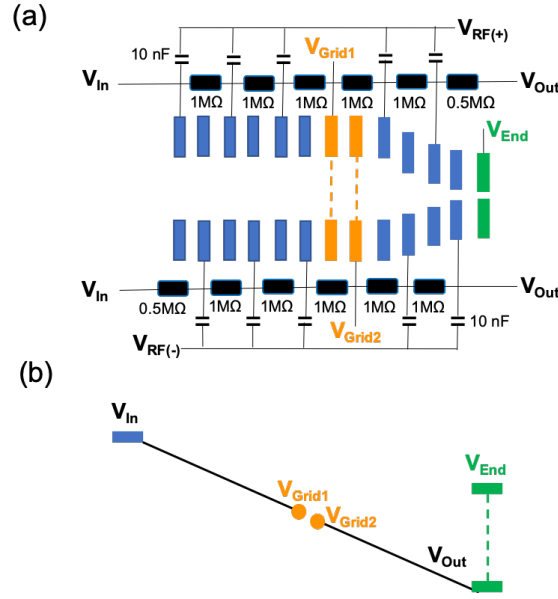


Figure 2.5: Schematic view (a) and relative operating potentials (b) of the various elements of the ion funnel trap.

Table 2.1: Typical DC voltage settings for the ion funnel trap.

Electrodes	V_{In}	V_{Grid1}	V_{Grid2}	V_{out}	V_{end}
Voltage (V)	380	280	270	260	275/250

2.2.2 Travelling wave IMS implemented by SLIM

The IMS device was designed using structures for lossless ion manipulation (SLIM) technology, first implemented by Smith and coworkers.⁷⁷⁻⁷⁸ This consists of a “sandwich” of mirror-image printed circuit boards (PCB), illustrated in Figure 2.6, and consists of three types of electrodes: (1) Guard electrodes confine the ions in the x-direction, perpendicular to the direction of travel. (2) RF electrodes which confine the ions in the y-direction between the two boards. (3) Repeating arrays of eight electrodes, to which a square potential is applied. This potential is stepped forwards one electrode at a time to produce a travelling wave which moves the ions in the z-direction, along the SLIM path.

The RF electrodes produce an effective potential (V_{eff}) in the y-direction, which is a scalar function of the y coordinate and is defined by the local intensity of the RF electric field (E_{RF}):

$$V_{eff} = \frac{zeE_{RF}^2}{4m\omega^2} \quad 2.1$$

where z is the ion's charge state, e is the elementary charge, m is the ion's mass, and ω is the angular frequency related to the RF frequency f (Hz) by $\omega = 2\pi f$. Since the RF electrodes do not produce any confinement in the x-direction, guard electrodes are necessary to keep the ions from dispersing off the edges of the track. It has been determined that when the spacing between the top and bottom boards is under 3 mm, the penetration of the DC guards in the effective potential in the y direction is eliminated.¹¹⁸ This is important as such penetration of the DC potentials will create off-center minima in the potential along the y-axis, resulting in the ions grouping close to the top and bottom RF electrodes. The electric potentials along the x- and y-coordinates are shown in Figure 2.7, where the (0,0) point is defined as the midpoint between the upper and lower boards and the left and right-side guard electrodes. We see that a global minimum is created around the (0,0,z) trajectory, and ions will not leave this region if their kinetic energy does not exceed the potential barriers produced by the guard electrodes. By keeping the ion's kinetic energy below that of the potential well, the lossless regime is achieved and the ions can be transferred along the z-axis with negligible losses.

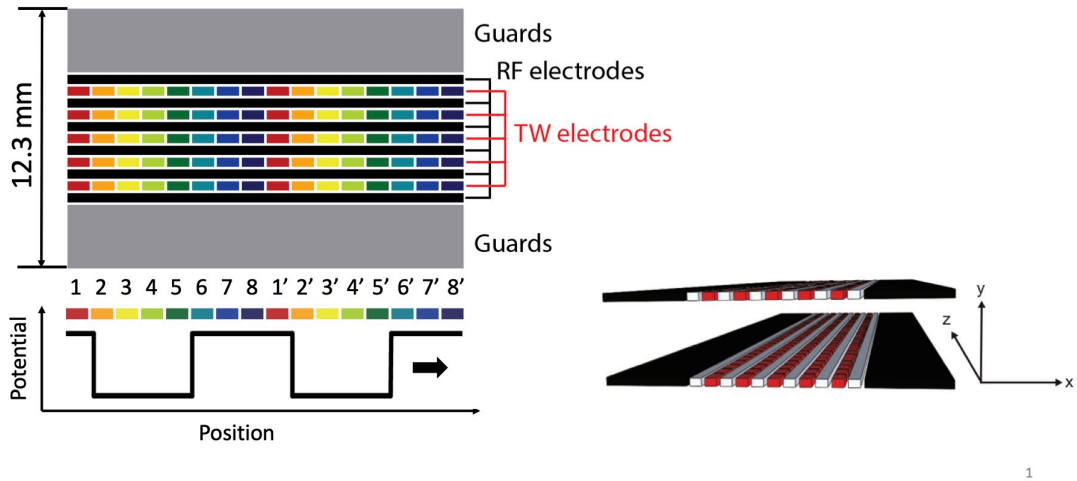


Figure 2.6: illustration of the electrode configuration on the PCB of a SLIM board and of the travelling wave configuration on the rung electrodes (left), and a 3D arrangement of a pair of PCB SLIM boards (right).

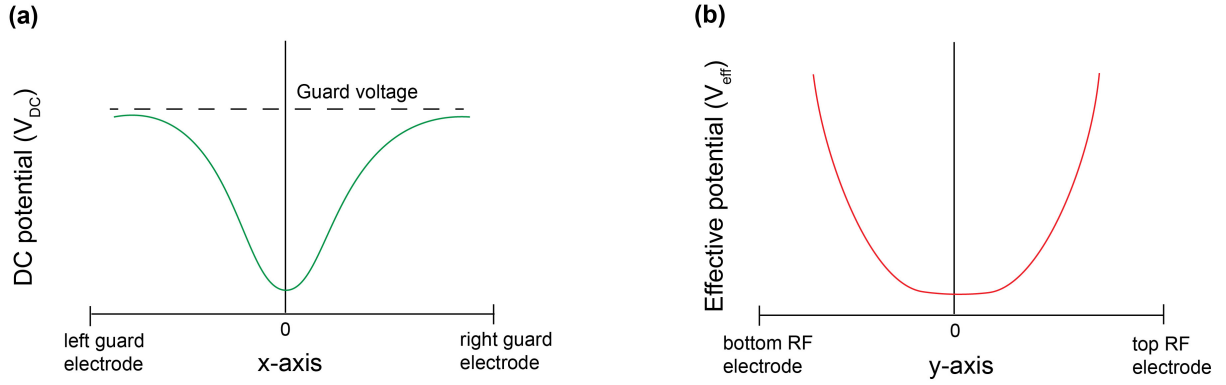


Figure 2.7: sketch of the (a) DC potential profile between the guard electrodes along the x-coordinate, (b) effective potential of the RF electrodes along the y-coordinate.

As the TW moves along the z-axis, the ions are pushed as packets in the valley between two wave peaks. The ions move with the same speed as the TW and ions of different mobility do not separate from one another. This operation is dubbed “surfing mode”, as the ions surf on the travelling wave and do not roll over. When the TW’s speed is increased, the collisions with the drift gas provide enough drag force so that ions with a larger collisional cross section (CCS) will roll over the TW and arrive at a later time. This roll over point is different for different CCSs, with bulkier ions rolling over sooner, and having longer drift times than more compact structures. Thus, when operating in roll-over mode, different structures can be separated from each other, based on their mobility through the drift gas.

The unit shown in Figure 2.6 can be repeated for extended lengths and can also be configured to produce 90° turns.¹¹⁹ These features were combined to produce the 35 x 28 cm SLIM board shown in Figure 2.8, with a serpentine ion path and a single-pass length of 7.5 m. The elements labelled B1, B2, B3, and B4 are electrodes which can be switched between traveling waves for propelling ions or static DC voltages, which can be used to block them. The bias of the SLIM board is typically set at 200 V, which is 50 volts lower than the V_{end} of the ion funnel, to introduce the ion pulse and achieve annealing of conformers. Ions of interest can be separated by travelling-wave IMS while traversing either a single pass along the 7.5 m serpentine path on the SLIM device or multiple passes through the same structure.

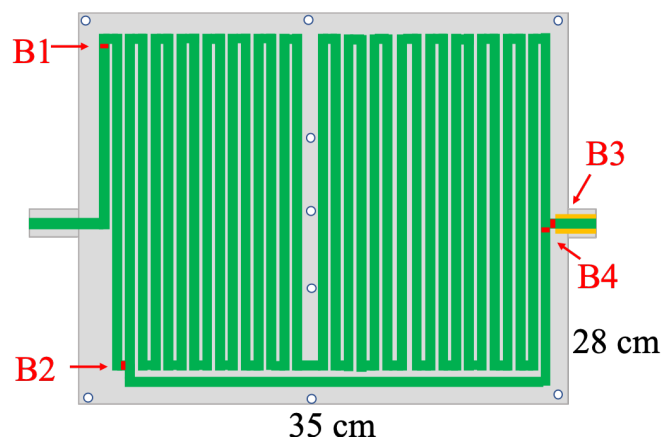


Figure 2.8: Schematic view of the SLIM board with a 7.5 m serpentine path used for IMS separation. The elements marked B1-B4 can be switched between the normal traveling wave potential and DC blocking potentials.

The optimum TW and DC settings for ion mobility separation are determined empirically. The TW consists of a square wave (i.e. 50% duty cycle) that can be varied in speed and amplitude. In a typical experiment, a TW amplitude of 15 V and speed of 420 m/s is used to separate ions. When performing IMS separation in a single-pass on the 7.5 m serpentine path, travelling wave voltages are applied to the elements B1, B2, and B3, while a blocking voltage of 240 V is applied to B4, which forces the ions to exit the SLIM board. To achieve longer path lengths and thus higher IMS resolution, the ions can be cycled multiple times by applying a blocking voltage of 240 V to B3 and a travelling wave to B4, which drives the ions into the next cycle. Elements B1 and B2 can be used as blocks to trap ions on the board instead of in the ion funnel, however we did not operate in this mode during the work reported here.

2.2.3 SLIM based ion guide and CID region

A planar RF ion guide, a schematic of which is shown in Figure 2.9, was designed based on the work of Smith and coworkers,¹²⁰⁻¹²¹ and is used to carry ions through the next stage of differential pumping and also to fragment them. The mirror-image pair of PCB boards contains guard electrodes (orange) to which we apply a static DC potential, and rung electrodes (blue) which have an RF potential superimposed on a DC potential. As with the TW SLIM device, the RF potential serves to confine ions in the direction normal to the board surface, while the guard electrode confines them perpendicular to their propagation direction. The DC potential on both the guard and rung electrodes gradually decreases along the length of the board, pushing the ions towards the RF hexapole. The exit of this planar guide narrows to concentrate ions into the subsequent hexapole guide through the slicing lens, which with a diameter of 0.6 mm, provides a conductance limit. An RF frequency of 1 MHz and amplitude of 20 V along with a DC gradient (i.e., difference between V_{in} and V_{out}) of a few tens of volts are used to guide the ions. The guard voltages ($V_{in-guard}$ and $V_{out-guard}$) are maintained 1 to 2 V higher than the DC imposed upon rung electrodes in order to keep the ions focused in the center of the track. Fragmentation of mobility-resolved isomer ions is induced by accelerating the ions through a potential difference of 100-200 V between the SLIM exit and the planar ion guide at a pressure of 10^{-1} mbar.

After passing through a quadrupole for mass selection, either the parent or fragment ions are then directed to the cryogenic ion trap where they can be characterized by messenger-tagging IR spectroscopy.

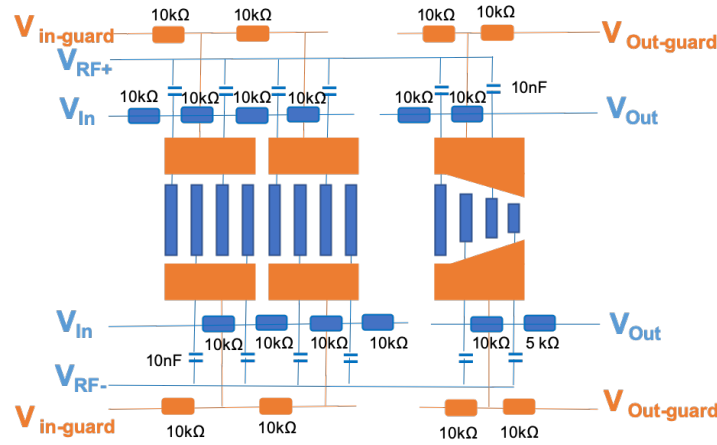


Figure 2.9: Schematic view of the planar, RF ion guide used in this work. The guide consists of two mirror-image boards of this type.

2.2.4 Electronics

The travelling waves, RF, and DC potentials for the SLIM-IMS and planar ion guide are generated by a customized power supply (GAA Custom Engineering, LLC). It provides eight TW output channels, two DC supplies for guard electrodes, an RF power supply for the SLIM and planar ion guide, and eight DC power supplies varying from -250 V to +250 V to bias various elements. An RF frequency of 550 KHz is used to drive the SLIM board, and 1 MHz is applied to the planar ion guide. The DC, RF, and TW potentials are controlled by the Modular Intelligent Power Sources (MIPS) software and triggered by an 8-channel delay generator (BNC MODEL 565).

2.2.5 Detection of ions in the SLIM IMS section and ion guide

The voltage setting for ion transition through the newly added stages had to be found empirically. For this, a picoammeter was used to detect for ions at different points along the ion path. While performing these tests, the last ion funnel electrode (V_{end} in Figure 2.5) was left on a constant DC voltage to allow for a continuous flow of ions to enter the SLIM device, thus facilitating detection of the ion current. The electrodes that were probed were B1 and B4 on the SLIM board (Figure 2.8), and the ion lens at the conductance limit separating the planar guide from the hexapole (Figure 2.4). Once current was detected, parameters were adjusted to maximise the current on each of these elements.

A maximum ion current of ~ 50 pA on B1 could be achieved by adjusting the bias of the SLIM board to be 50 V less than the exit of the ion funnel. It is worth to mention that the ion current measured at

the end of the ion funnel was ~ 100 pA, which indicates that there are some significant ion losses when passing from the funnel into the SLIM boards. The ion current detected on B3 is optimized by tuning the RF frequency and guard voltages and a current about equivalent to that detected on B1 is achieved, indicating minimal losses of ions through the 7.5m drift path. However, a maximum of only 2 pA can be detected on the ion lens after the planar ion guide, once again indicating significant losses. Although we cannot exclude the possibility that these losses occur in the planar ion guide, it seems much more likely that the ions are being lost when passing through the ion lens which separates the SLIM IMS board from the planar ion guide. In any case, once 2 pA of current has been achieved on this lens, ions are easily detected on the channeltrons downstream.

2.2.6 Performance of the SLIM-IMS module

We characterized the IMS capabilities of this new instrument using the reverse peptides GRGDS and SDGRG in their singly charged state ($[M+H]^+$) which have collisional cross sections (CCSs) of 135.2 \AA^2 and 133.9 \AA^2 respectively.¹²² The resolution a TW-IMS device cannot be calculated directly from the drift times because of the complex relationship between drift times and collisional cross section.¹²³ Instead, we calibrate our drift time scale with these previously calculated CCSs and calculate the resolution of our IMS device using the peak-width definition shown in equation 2.2:

$$R = \frac{\Omega}{\Delta\Omega} \quad 2.2$$

where Ω is the CCS and $\Delta\Omega$ is the peak width on the CCS axis at half of its height. Assuming linearity between CCS and drift times over this range, we calculate the resolution for the two peptides as a function of the number of cycles and plot the results in Figure 2.10. The resolution after a single cycle along the 7.5 m serpentine path is ~ 200 , classifying our device as ultra-high resolution. After eight cycles, which represents a ~ 60 m pathlength, a resolution increases to 560 is achieved. This indicates the newly designed SLIM-IMS is able to separate isomers that differ in CCS by as little as 0.18%.

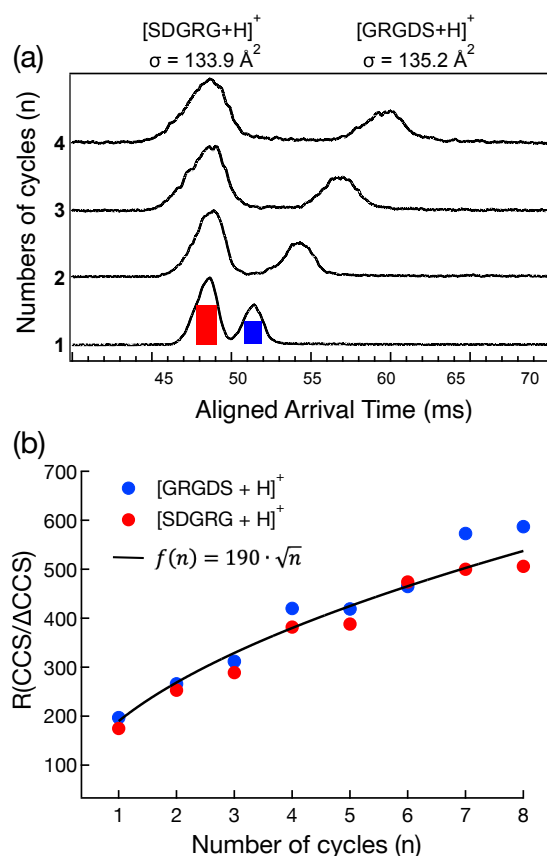


Figure 2.10: (a) Arrival time distribution of singly protonated cations for a mixture of the reverse-sequence peptides GRGDS and SDGRG for different number of cycles n (7.5 m per cycle). The arrival times after multiple cycles have been aligned to the first peak of the single-cycle ATD. (b) IMS resolution of the new instrument as a function of the number of cycles n .

The transmission of our device is demonstrated in Figure 2.11, where GRGDS was sent once, twice, and three times through our ion SLIM track. The ATD was recorded for each cycle (Figure 2.11a) and the integrated signal, corresponding to the number of ions, is shown in Figure 2.11b. A 3.75 % loss of ions over the three cycles (22.5m) is an acceptable transmission, allowing us to reach a resolution of well over 200, without sacrificing ion intensity.

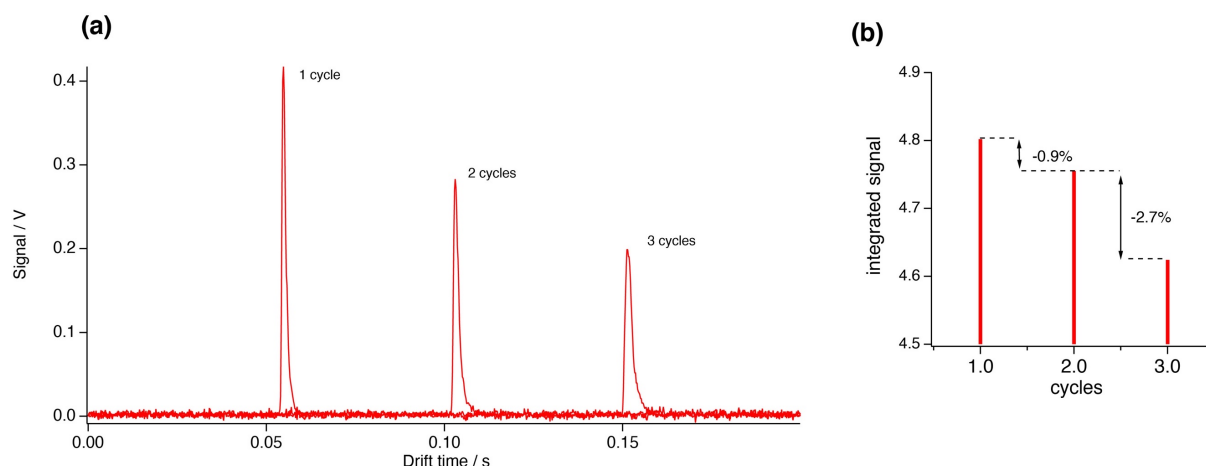


Figure 2.11: (a) Arrival time distribution of singly protonated SDGRG for 1, 2, and 3 cycles through the SLIM. (b) integrated signal for each cycle, with the losses indicated as a percentage.

To demonstrate the capability of our modified instrument to produce CID fragments, we used the singly sodiated isomeric human milk oligosaccharides Lacto-N-tetraose (LNT) and Lacto-N-neotetraose (LNnT). The results are shown in Figure 3.11. Each of these sugars separated into two distinct mobility peaks after 7.5 and 15m drift paths respectively (Figures 2.12b and 2.12e) indicating that each molecule contains two structures, most likely the reducing end anomers. Each of these mobility peaks were gated and fragmented upon entering the SLIM ion guide region, producing a number of fragments shown in Figures 2.12c and 2.12f. For LNT, the CID spectrum looks identical for the first and second mobility peak, but in the case of LNnT, the second mobility peak appears to provide a higher fragmentation yield. However, assigning a structure to each mobility peak based on the fragmentation pattern alone is not straightforward and will not be attempted here.

This data illustrates that our instrument is capable of performing mobility-selective CID which, when coupled with spectroscopy, will provide a very promising new tool to identify isomeric molecules. The application of this to glycans will be explored in Chapter 5.

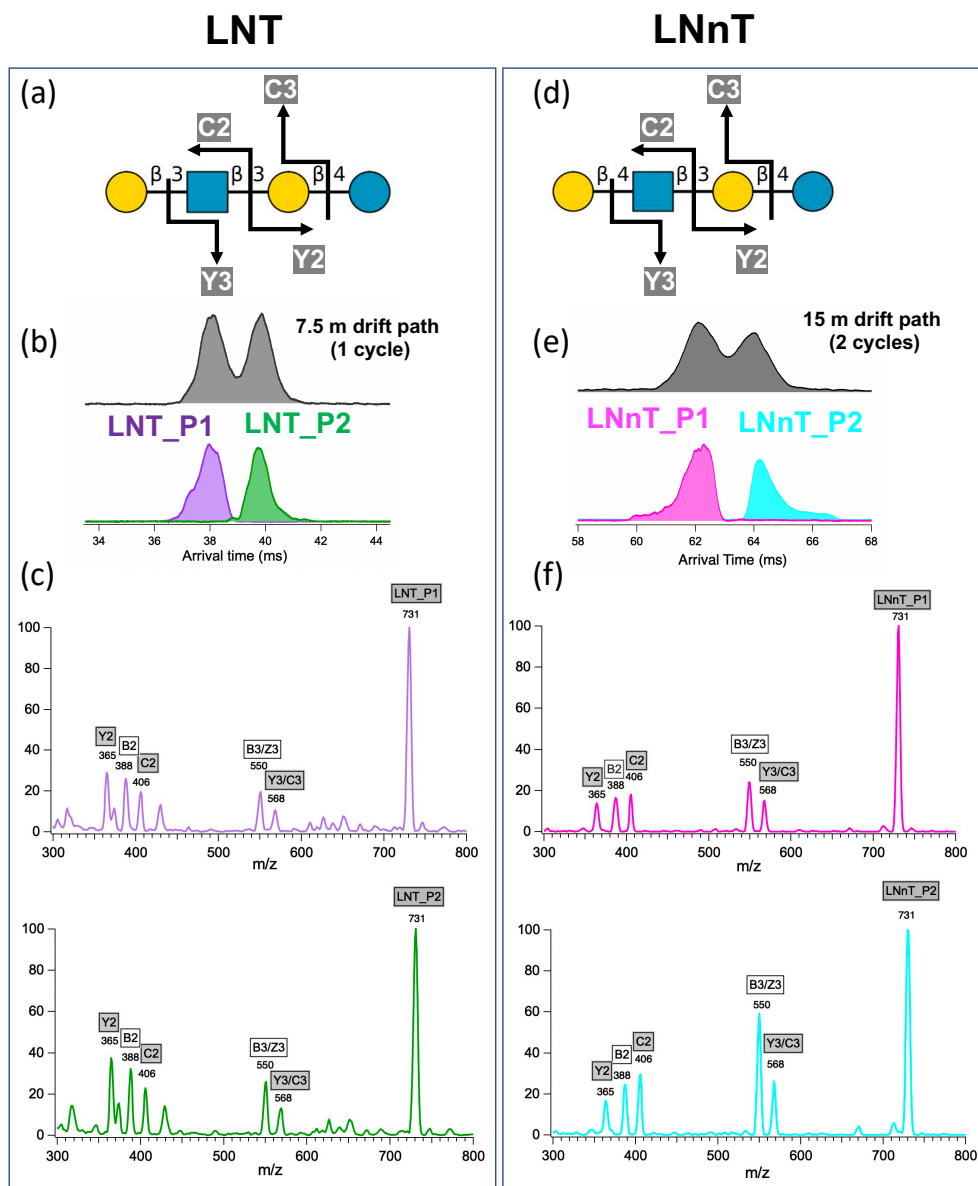


Figure 2.12: Nomenclature of C/Y fragments of (a) LNT and (d) LNnT, IMS separation and slice of (b) LNT and (e) LNnT, and isomer-specific fragmentation of well-sliced peaks for (c) LNT and (f) LNnT.

3. Collision-induced dissociation of sodiated glycans

To fully appreciate the underlying principles on which the work of this thesis is based, it is important to understand the collisional journey of a glycan ion as it travels through our instrumental setups described in Chapter 2. We will take as example the initial instrument, on which the majority of the work presented in this thesis was performed (Chapters 4 and 6). The collisional journey of the ions through the updated version of the instrument with the SLIM-IMS stage is analogous to that presented here, with the exception that the ions undergo extra collisions with the buffer gas as they go through the serpentine SLIM path. These collisions however are not observed to produce any fragmentation due to the high pressure in this region causing collisional deactivation to play an important role and is further addressed in section 3.4.

The gas-phase glycan ion produced by electrospray is bound to a sodium cation by non-covalent interactions and is manipulated through the electric fields thanks to the +1 charge of this cation. This singly-sodiated glycan is transferred through a 15 cm ion funnel at 3 to 4 mbar pressure before being transferred into the hexapole in the next differentially pumped stage. Upon leaving the ion funnel, the ion is accelerated through a strong electric field at a significantly lower pressure of $\sim 10^{-2}$ mbar. The ion experiences collisions of significant energy in this region which causes it to fragment. The fragments which carry the sodium charge continue their journey into lower pressure regions where collisions become unlikely and are selected by a quadrupole mass filter for spectroscopic analysis and detection.

From this, it is clear that the ion does not fragment whenever it hits a gas molecule, but rather that certain conditions must be fulfilled before fragmentation can occur. In this chapter, we will cover the mechanisms responsible for collision-induced dissociation (CID) and see how they relate to the fragmentation of glycans.

3.1 Fragmentation of the glycosidic linkage

Fragmentation at the glycosidic linkage is the most commonly observed type of fragmentation in glycans. As discussed in chapter 1.4, this leads to the formation of B, Y, C, and Z fragments. The mechanisms and kinetics of these processes tend to vary greatly, depending on the charge state of the parent ion, so we will focus on studies that have been carried out on singly sodiated sugars, which is the charged state used in all the CID experiments presented in this thesis. Using tandem mass spectrometry experiments, combined with computational methods, Bythell and coworkers proposed mechanisms for the formation of B/Y and C/Z fragments from singly sodiated disaccharides.¹²⁴⁻¹²⁵ Importantly, the activation barriers for B/Y and C/Z fragmentation were calculated to be ~ 230 kJ/mol and ~ 310 kJ/mol, respectively. This corresponds to the general observation that the B/Y fragmentation pathway is generally more abundant in sodiated sugars than the C/Z pathway. Converting these activation energies to electron volts gives us 2.38 eV for B/Y, and 3.21 eV for C/Z fragmentation. The collisions of our glycan ions with the gas must therefore result in the transfer of at least a few electron volts into the ion's internal energy for any fragments to be observed. This

energy transfer must result from some of the ion's kinetic energy being converted into internal energy and this is what will be discussed in the following section.

3.2. Center-of-mass reference frame

To determine how much of an ion's kinetic energy is available to be converted into internal energy upon a collision, let us consider what happens when an ion of mass m , collides with a neutral gas molecule of mass N . To facilitate the description of this process, it is easier to work in the center-of-mass (COM) reference frame instead of that of the laboratory (Figure 3.1), and we will approximate the colliding molecules as point masses.

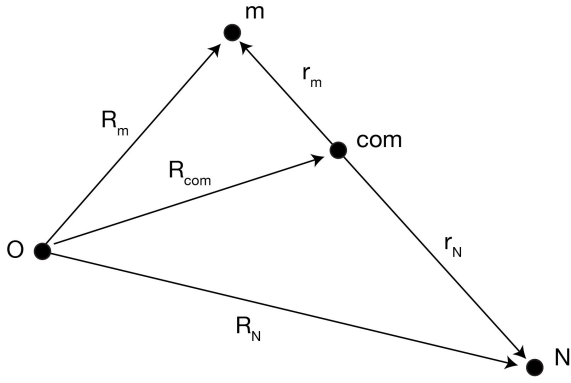


Figure 3.1: Laboratory and center-of-mass (COM) coordinate systems of masses m and N prior to a collision the origin of the laboratory is indicated as O .

When sitting on the COM framework, the sum of momenta of the two masses is by definition equal to zero:

$$m(\mathbf{R}_m - \mathbf{R}_{com}) + N(\mathbf{R}_N - \mathbf{R}_{com}) = 0 \quad 3.1$$

Differentiating \mathbf{R}_{com} with respect to time in the above expression gives \mathbf{v}_{com} :

$$\mathbf{v}_{com} = \mathbf{R}'_{com} = \frac{m\mathbf{R}'_m + N\mathbf{R}'_N}{m + N} \quad 3.2$$

The kinetic energy of the particles m and N relative to each other is given by their velocity vectors \mathbf{r}'_m and \mathbf{r}'_N :

$$E_{rel} = \frac{1}{2}m(\mathbf{r}'_m)^2 + \frac{1}{2}N(\mathbf{r}'_N)^2 \quad 3.3$$

Where \mathbf{r}'_m and \mathbf{r}'_N can be expressed in terms of \mathbf{R}'_m and \mathbf{R}'_N :

$$\mathbf{r}'_m = \mathbf{R}'_m - \mathbf{R}'_{com} = \mathbf{R}'_m - \mathbf{v}_{com} = \frac{N(\mathbf{R}'_m - \mathbf{R}'_N)}{m + N} = \frac{N\mathbf{v}_{rel}}{m + N} \quad 3.4$$

$$\mathbf{r}'_N = \mathbf{R}'_N - \mathbf{R}'_{com} = \mathbf{R}'_N - \mathbf{v}_{com} = \frac{m(\mathbf{R}'_n - \mathbf{R}'_m)}{m + N} = \frac{-m\mathbf{v}_{rel}}{m + N} \quad 3.5$$

Where \mathbf{v}_{rel} replaces the expression $(\mathbf{R}'_m - \mathbf{R}'_N)$. Substituting this into the expression for the kinetic energy gives:

$$E_{rel} = \frac{1}{2} \left(\frac{mN}{m + N} \right) \mathbf{v}_{rel}^2 \quad 3.6$$

If the kinetic energy of the system after the collision is less than the kinetic energy before, then some of the energy was transferred to internal energy in the colliding particles. Because energy is conserved, this amount energy converted into internal energy (Q) must be equal to the change in kinetic energy:

$$Q = \Delta E_{rel} = \frac{1}{2} \left(\frac{mN}{m + N} \right) \mathbf{v}_i^2 - \frac{1}{2} \left(\frac{mN}{m + N} \right) \mathbf{v}_f^2 \quad 3.7$$

We can see that the value of Q will be maximum when $\mathbf{v}_f = 0$, that is the particles stick together after colliding, in which case:

$$Q_{max} = \frac{1}{2} \left(\frac{mN}{m + N} \right) \mathbf{v}_i^2 = \left(\frac{N}{m + N} \right) \frac{1}{2} m \mathbf{v}_i^2 = \left(\frac{N}{m + N} \right) E_{lab} \quad 3.8$$

From this expression, we can see that the mass of the ion and neutral gas target play a role in the energy transferred. The larger the mass of the neutral with respect to the ion, the closer the fraction $\left(\frac{N}{m+N} \right)$ tends to unity, and the larger the transfer of kinetic energy to internal energy. In order to determine be able to determine the kinetic energy of our ions in the collision region, we need to know the electric field through which the ion travel, but also how far the ions will travel on average before colliding with the neutral gas. This distance, known as the mean free path, is pressure-dependent and is the focus of the next section.

3.3 Mean free path and the effects of pressure

Mean free path is the average distance a particle will travel through a gas before colliding with one of the gas molecules. The mean free path λ for an ion of diameter d travelling through an ideal gas is given by the expression:

$$\lambda = \frac{RT}{\sqrt{2}\pi d^2 N_A P} \quad 3.9$$

where R is the ideal gas constant, T is the temperature of the gas, N_A is the Avogadro's number, and P is the pressure of the target gas in the collision region.

In order to better visualize the situation in the collision region, Figure 3.2a shows the part of the instrument presented in Chapter 2.1 where CID occurs, and Figure 3.2b illustrates the voltages across the interface between the ion funnel exit and the hexapole bias.

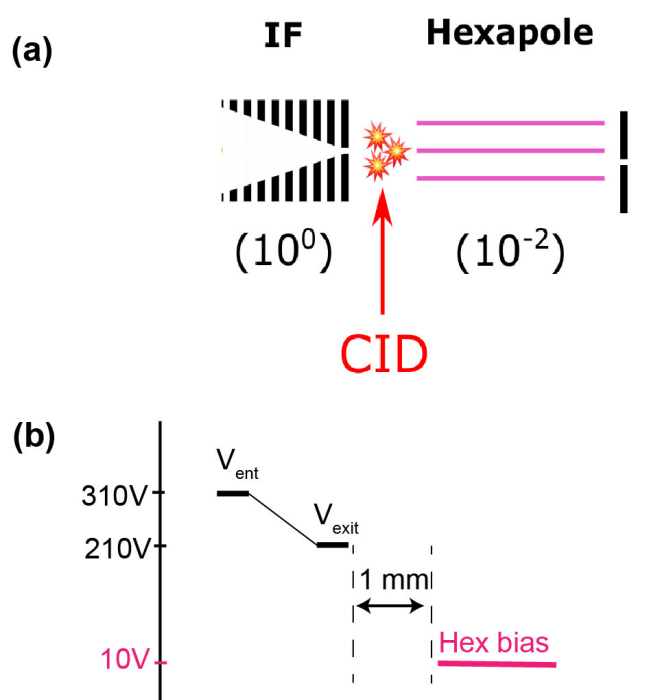


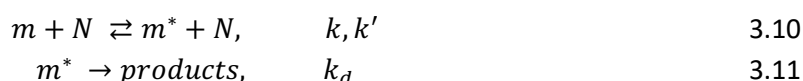
Figure 3.2: close-up illustration of the CID region in the tandem mass spectrometer described in Chapter 2., with (a) the CID region highlighted, and (b) the voltage profiles used to generate fragments.

At a pressure of $P = 10^{-2}$ mbar, the mean free path of a lactose ion ($d \approx 2$ nm) is calculated to be $\lambda \approx 0.2$ mm. This disaccharide ion fragments at the conditions shown in Figure 3.2b, where the ion is accelerated over a 200 V drop across a 1 mm gap between the exit of the ion funnel and the hexapole bias. The electric field in the CID region is therefore 200 V/mm. Because the mean free path is 0.2 mm, the ions undergo on average 5 collisions while traversing this electric field, resulting in 40 eV per collision. However, we know from the previous section that not all this energy is converted into internal energy. Using equation 3.8 and taking nitrogen as the collision gas ($N = 28$), the maximum kinetic energy which is available to be converted into internal energy (Q_{max}) is 2.8 eV. Therefore, a single collision would be enough to cause the activation barrier to form B/Y fragments, and two collisions will be needed to generate C/Z fragments, according to the activation barriers calculated for sodiated lactose.¹²⁴⁻¹²⁵ In reality, the energy transfer will be lower Q_{max} , as this value is calculated making the assumption that the colliding particles stick together after the collision. This will almost never be the case and therefore $Q < Q_{max}$, requiring more than a couple of collisions to induce fragmentation. But since the ions collide on average 5 times while traversing this stage, it seems probable that some of them pick up enough energy to fragment, and we see this experimentally.

From this, we can conclude that our ion gains sufficient internal energy to fragment. How this energy is redistributed within the molecule and how unimolecular dissociation happens are the subject of the next two sections.

3.4 Collisional activation and the two-step process

The process of dissociation of polyatomic molecules due to collisions is described by the Linderman mechanism, shown in equations 3.10 and 3.11. The reaction is assumed to occur as two elementary steps: bimolecular activation and deactivation (equation 3.10) with the rate constants k and k' respectively, and unimolecular dissociation to products with the rate constant k_d (equation 3.11).



A collisionally activated molecule (m^*) can therefore either form products, or undergo a subsequent collision which deactivates it. The process of activation/deactivation is pressure dependent. If we consider a very low-pressure regime, in which our molecule m experiences a single collision with the neutral gas N , the formed activated species m^* will not experience a subsequent deactivating collision, and will therefore form products. Conversely, if the pressure of the gas is high enough, the high frequency of collisions will result in the deactivating process to be significant, to a point where no products will be formed. This is the case in the SLIM IMS device, where high frequency of collisions maintains an equilibrium between the molecules and the drift gas, and no fragmentation is observed in this stage of the device.

It is generally assumed that during CID, the process of activation happens much faster timescale than unimolecular dissociation. This allows the two events to be treated separately as a two-step process. Ion activation can occur through a single, high-energy collision which brings a molecular bond above its dissociation limit, resulting in the breaking of that bond as shown in Figure 3.3a. This is the case of high-energy CID where a single collision, usually in the keV range, resulting in the molecule being excited to a higher electronic state from which it dissociates. In such cases, the energy absorbed during the collision does not have the time to redistribute throughout the molecule, resulting in non-statistical formation of fragments. When ion activation occurs through a series of low-energy collisions (Figure 3.3b), the vibrational states are usually excited and the process of raising the molecule's internal energy above the dissociation threshold is gradual. This allows time for the gained energy to populate the various vibrational modes of the molecule by intramolecular vibrational energy redistribution (IVR) and the fragmentation occurs as a statistical process, consistently taking the fragmentation pathways with the lowest activation barriers. This is the case of low-energy CID in which the collisions are generally in the 1 to 100 eV range.¹²⁶

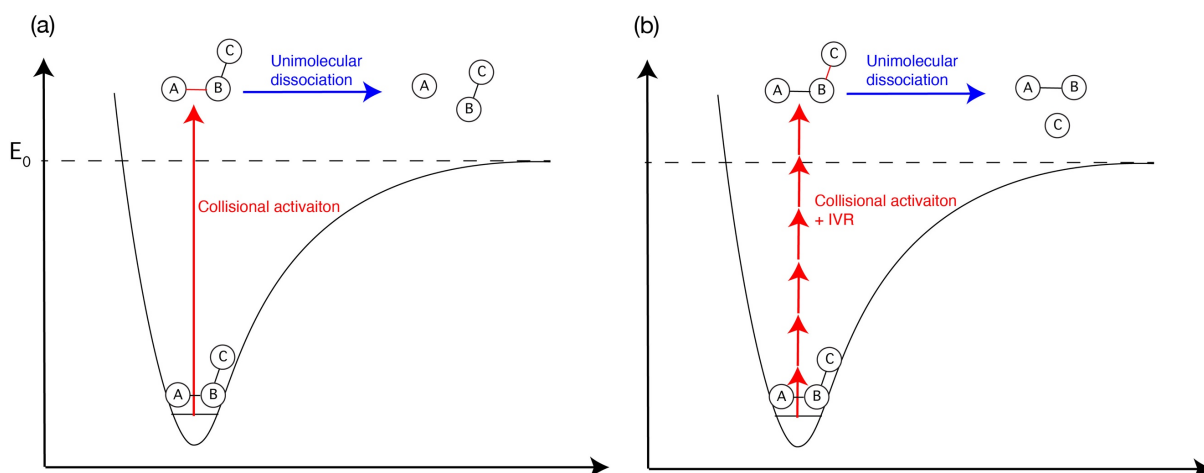


Figure 3.3: illustration of the activation processes leading to unimolecular dissociation by (a) a single high-energy collision, and (b) multiple collisions.

As we calculated in the previous section, collisional energy in our instrument is about 40 eV, putting us in the range of low-energy CID. Therefore, the model in Figure 3.3b applies to our ions, and the energy absorbed by our ions through collisions have the time to redistribute throughout the molecule by IVR. And the formation of fragments is a statistical process.

It does not suffice that the dissociation threshold (E_0) is reached for fragmentation to happen. An excess amount of energy, known as the *kinetic shift*, is required to induce fragmentation on a timescale relevant to the measurement. This has to do with the kinetics of unimolecular dissociation which is described for polyatomic molecules by the Rice, Ramsperger Kassel and Marcus (RRKM) theory.

3.5 Unimolecular dissociation and RRKM theory

When the collisionally activated molecule spontaneously dissociates into products, and the reaction coordinate contains a single barrier, transition state theory can adequately describe the kinetics of the process. However, as is often the case in polyatomic molecules, the potential energy surface is such that there is more than one reaction barrier along the reaction coordinate. Between any two such reaction barriers, there will be a potential well as, shown by the one-dimensional cut of a multi-dimensional potential energy surface in Figure 3.4. A molecule with enough internal energy to cross the first barrier will dissociate into products, but the products may reside for a time in this well as a seemingly stable molecule, before escaping over the second barrier. This temporary trapping is due to some of the total energy of the system flowing out of the reaction coordinate and into the internal degrees of freedom of the system (indicated by the double arrow in Figure 3.4). Consequently, the molecule behaves as though it was bound, even though it has enough energy to dissociate, and only when the energy flows back into the reaction coordinate does the molecule cross the second barrier and form the dissociated products.

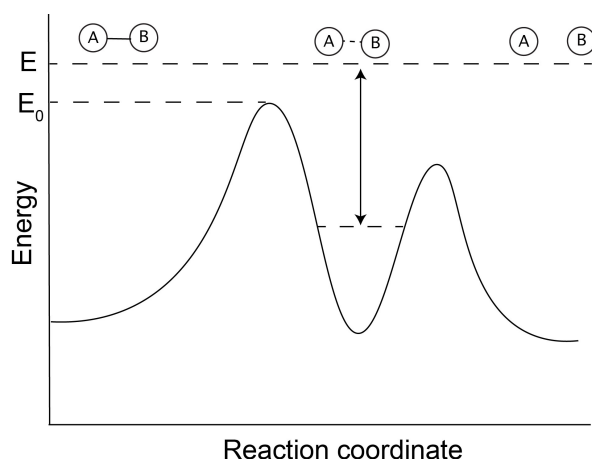


Figure 3.4: illustration of a unimolecular dissociation along a reaction coordinate with two barriers, shown as a one-dimensional cut of a multi-dimensional potential energy surface. After crossing the first barrier, the products can get temporarily trapped in the local minimum if the energy leaves the reaction coordinate and flows into other degrees of freedom before returning and driving the products to dissociation.

To calculate the rate constant of such a process, the Rice, Ramsperger Kassel and Marcus (RRKM)¹²⁷ theory is typically used. This theory is based on two assumptions: (1) statistical redistribution of the vibrational energy among all the vibrational modes of the molecule is achieved on a timescale much smaller than that of the reaction, (2) the formation of reactants to products, crossing of the transition state is irreversible.

For a fragmentation reaction defined by a threshold energy (E_0), RRKM theory provides an equation describing the rate constant of the fragmentation as a function of internal energy:

$$k(E) = \frac{\int_0^{E-E_0} \rho^\ddagger(E') dE'}{h\rho(E)} \quad 3.12$$

where $\rho(E)$ is the density of vibrational states of the reactant, $\rho^\ddagger(E')$ is the density of states on the transition state surface, and h is the Plank's constant. This equation gives the ratio of the total number of states on the transition surface with energies between the threshold energy E_0 and a given energy E to the density of reactant states at this energy E . Furthermore, we can see from equation 3.12 that the rate of unimolecular dissociation is greater than zero only if the ion is above the threshold energy (i.e. $E - E_0 > 0$), and also that the rate of dissociation will increase with energy.

3.6 Competitive pathways and ion relaxation

When an ion has been collisionally activated, unimolecular dissociation is not the only reaction that may occur. Molecular rearrangements can also occur once collisional activation has imparted sufficient energy to cross the activation barriers between different conformers. This tends to happen especially in low-energy CID where the activation process happens gradually, allowing time for the energy to find the reaction coordinate responsible for rearrangements. One consequence of this is

that fragments may be generated from a different conformer than the one that was initially targeted, provided the timescales of rearrangement are shorter than those of collisional activation and dissociation from the initial conformer. Although such rearrangements can be important when studying molecules consisting of a few atoms,¹²⁸ it is often of little importance in analytical applications to larger molecules, such as glycans where multiple conformers are commonly expected. In the particular case of glycans, the primary structure is generally the subject of interest and a fragment that can identify a bond linkage or monosaccharide sequence is valuable information, regardless of whether the parent underwent a conformational change prior to the fragmentation.

Ion relaxation from its collisionally activated state can occur through spontaneous emission of an IR photon, or through collisional deactivation. The spontaneous emission of photons to cool vibrationally excited molecules is a slow process, typically occurring over seconds¹²⁹⁻¹³⁰ and therefore does not kinetically compete with fragmentation. As already discussed in section 3.4, collisional deactivation can also occur, but in the CID region, the pressure of 10^{-2} mbar results in an insufficient number of collisions for this process to be significant.

3.7 Closing comments

In this chapter, we follow the collisional journey of an ion through our instrumental setup. The ion accumulates energy in the CID region, where the pressure is low enough so that collisional deactivation becomes unlikely, while being high enough so that collisions occur within the distance across the electric field. The collisions occur on the order of ~ 40 eV and some of the kinetic energy is converted into vibrational energy upon collision. The mean free path allows for multiple collisions to occur, which gradually raise the internal energy of the ion above the dissociation threshold, the process of IVR ensuring that the energy is statistically distributed among the vibrational modes of the molecule. Hence, the dissociation follows the reaction coordinate with the lowest activation barriers and the rate of dissociation can be described by RRKM theory.

In the following chapters will explore how we can combine this process with infrared spectroscopy and ion mobility to provide ways to identify glycan isomers by breaking them down by CID and studying their fragments. We will also try to gain some insight into the mechanistics of glycan fragmentation.

4. Anomeric retention of glycan C-type fragments

As described in Chapter 1, collision-induced dissociation (CID) of glycans can generate fragments which reflect the structural details of the parent molecule. Recent studies have shown that C_1 fragments generated by CID of lithiated disaccharides and protonated tetra and pentasaccharides retain the anomericity of the glycosidic bond.⁸² If this result can be generalized to larger parent molecules and larger fragments, it would provide a powerful tool for glycan sequencing. When using a spectral database approach, this property could serve, for example, to identify fragments of a parent that is not yet part of the database. By matching the fragments to database entries and using the principle of anomer retention, we can then re-construct the exact structure of the parent glycan, including bond anomericity, and add its IR spectrum as a new entry to our database.

In this chapter, we use messenger-tagging infrared (IR) spectroscopy to investigate the generality of anomer retention upon CID of increasingly large and complex sodiated glycans. Our results demonstrate that anomericity appears to be retained for these glycans, regardless of the fragment size and branching.

The content of this Chapter is adapted with permission from the article: R.P. Pellegrinelli, L. Yue, E. Carrascosa, S. Warnke, A. Ben Faleh, and T.R. Rizzo, "How General Is Anomeric Retention during Collision-Induced Dissociation of Glycans?", JACS 2020. It is available online at: <https://pubs.acs.org/doi/10.1021/jacs.0c00264>.

4.1 Introduction

In glycan analysis, determining the anomericity of the glycosidic bond stands out as a particular challenge. Very recently, Compagnon and co-workers showed spectroscopic evidence that C_1 fragments (Figure 4.1) generated by collision-induced dissociation (CID) of lithiated disaccharides and protonated sugars tetra and pentasaccharides retain the anomeric configuration of the glycosidic bond,⁸² and this has also been investigated by coupling ion mobility with tandem MS.^{72, 131}

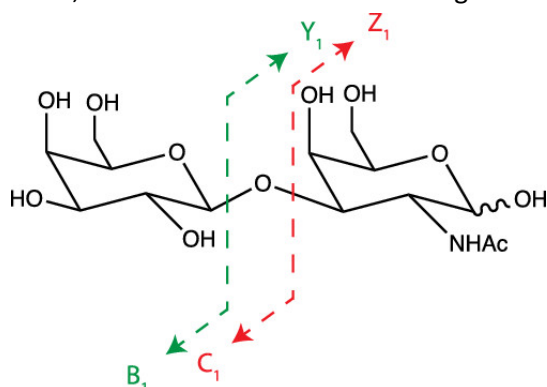


Figure 4.1: Nomenclature for B/Y and C/Z fragments of glycans. It should be noted that both the C and Y fragments carry a hydrogen to form an intact glycan.

This finding raises many questions: How general is anomeric retention in the gas phase? Does it apply to larger, more complex glycans? Does it apply to larger fragments? The answers to these questions are likely to have profound implications for glycan analysis.

The anomericity of the glycosidic bond, which can exist in either the α or β configuration, is commonly determined by coupling exoglycosidase digestion with liquid chromatography.^{42, 50, 53-54} However, this usually involves lengthy incubation times and multiple chromatographic separations. As already discussed in the introduction, techniques such as NMR³³ and X-ray crystallography³² can provide detailed structural information including the anomeric configuration, but they require a relatively large amount of sample, which is often not available in the case of glycans. Branching, bond position, and anomericity can be successfully determined using tandem MS by analyzing the fragments from relatively small glycans,^{52, 55, 132-134} although the latter require observing cross-ring fragments that preserve the anomeric configuration of the glycosidic bond.^{50, 116} Nevertheless, tandem MS is typically unable to fully distinguish between all isomeric forms.

Infrared (IR) spectroscopy is a promising tool for glycan analysis, as the vibrational spectrum is extremely sensitive to the slightest of structural differences. Recently, room-temperature infrared multiple photon dissociation (IRMPD) has been used to fingerprint monosaccharide fragments,⁸² while cryogenic IR spectroscopy has been used by Pagel and coworkers¹³⁵ as well as our group^{89, 94} to identify spectral fingerprints of increasingly complex sets of isomeric glycans. Cryogenic spectroscopy has the advantage of eliminating thermal inhomogeneous broadening, resulting in significantly increased resolution for large molecules with congested vibrational spectra.¹³⁶ In this work, we use cryogenic messenger-tagging infrared spectroscopy and ultrahigh-resolution ion mobility spectrometry (IMS) to investigate the generality of anomeric retention upon CID.

4.2 Experimental approach

The tandem mass spectrometer described in Chapter 2.1 was used in this study and the details of this instrument can be found elsewhere.¹¹³ The sodiated glycan ions were sprayed from a 100 μ M solution of water and methanol (1:1). Fragmentation was induced by collisions in the hexapole at a pressure of 10^{-1} mbar by accelerating the ions through a potential difference between the funnel exit and hexapole bias. A potential difference of ~ 200 V is used to fragment sodiated glycans. Fragments of a specific m/z are selected by a first quadrupole mass filter and sent to a cryogenic octupole ion trap enclosed in a copper housing. For sodiated species, the trap is maintained at 60K, ions are cooled by collisions with a cold gas mixture containing He/N₂ (90/10) and tagged with a weakly bound nitrogen molecule. The tagged ions are irradiated every other trapping cycle by a single IR pulse from an optical parametric oscillator (OPO) before being sent through a second quadrupole mass filter and detected by a channeltron.

4.3 Mass spectra of CID fragments

The generation of C fragments from the sodiated glycans did not always yield a high ion intensity. As pointed out in Chapter 1.4, B and Y fragments were often the main fragmentation product for sodiated species, and this may be rationalized by the reaction barriers for the B/Y transition states being lower than that of the C/Z pathways, as discussed in Chapter 2.1.¹²⁴⁻¹²⁵ The mass spectrum of the singly

sodiated disaccharide Gal α (1–3)GalNAc and tetrasaccharide LNnT, both of which were studied in this work, are shown in Figure 4.2 as a function for different potential differences between the ion funnel and the hexapole. Fragments identified from glycosidic cleavages are highlighted. It is clear from both spectra that the fragments highlighted are not present at low potential differences, but only appear after a certain amount of activation, representing the dissociation threshold. Increasing the potential difference from 130 V to 220 V on Gal α (1–3)GalNAc (Figure 4.2a), increases the yield of B₁ and Y₁ fragments without noticeably increasing the C₁ fragment. This means that experiments investigating the C₁ fragment of this molecule could be carried out at lower collision energy than that required for another molecule like LNnT. However, for the sake of consistency, all CID experiments of sodiated sugars in this chapter were run at ~200 V.

The mass spectrum of LNnT (Figure 4.2b) contains ambiguous peaks, with the fragment at m/z 550 corresponding to either a B₃ or a Z₃ fragment and the fragment at m/z 568 being either a C₃ or Y₃ fragment. The fragment at m/z 550 could be identified by O¹⁸ labelling at the reducing end OH. If the fragment is a Z₃, a mass shift of +2 a.u. will be observed, since Z fragments carry the reducing end OH, while the B₃ fragment would not show any mass shift. This however was not done, as these fragments are not of interest in the context of this chapter. The fragment at m/z 568 is however important to the goal of this work. If it is C₃, it could expand our study of anomeric retention to fragments containing three monosaccharide units. Unfortunately, this fragment was identified as a Y₃ fragment by spectroscopy (section 4.6) and does not tell us anything about the anomeric configuration of the glycosidic bond.

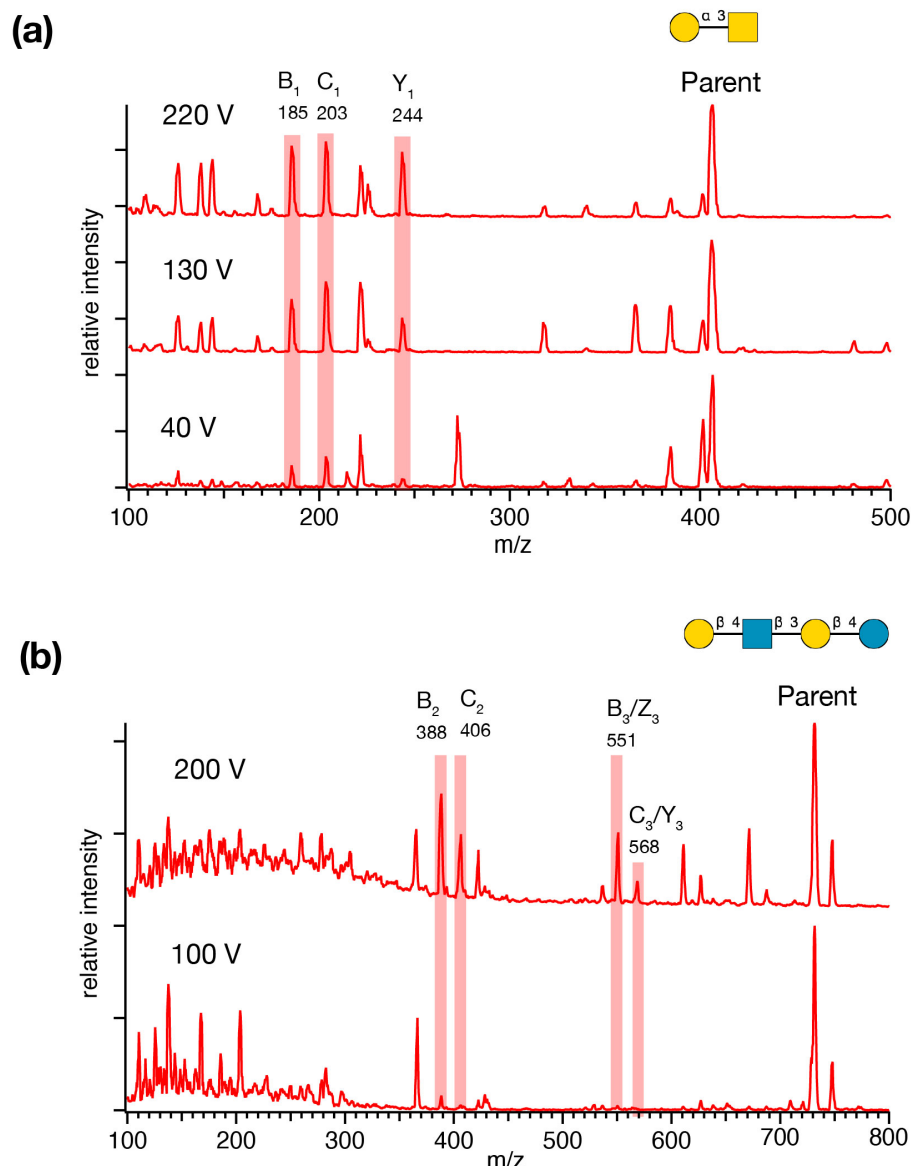


Figure 4.2: Mass spectra of the disaccharide Gal α (1-3)GalNAc (a) and the tetrasaccharide LNnT (b) at different potential differences (indicated) across the CID region. Identified fragments from glycosidic cleavages are indicated and highlighted.

4.4 Cryogenic infrared spectrum of a monosaccharide

The infrared spectrum of the sodiated monosaccharide GalNAc is shown in Figure 4.3a. The 3200 – 3750 cm^{-1} range scanned by our OPO corresponds to the stretching modes of the NH and OH functional groups. The spectrum shows six vibrational bands, while the molecule only contains five oscillators in this energy range (one NH and four OH). This indicates that more than one conformer must be present. The assignments of these bands can be partially done based on textbook knowledge of the vibrational energies of the oscillators present in the molecule. The distinct band between 3300 and 3350 cm^{-1} is characteristic of a secondary amine N-H stretch, while the bands above 3580 cm^{-1} represent the free O-H stretching region. The vibrations observed in the 3450 – 3470 cm^{-1} region correspond to an OH group which is slightly bound, either intramolecularly or to the sodium cation.

These vibrational transitions have been observed for cryogenic gas-phase ions and in some cases have been assigned either by calculation and/or isotopic labelling.¹³⁷⁻¹³⁹

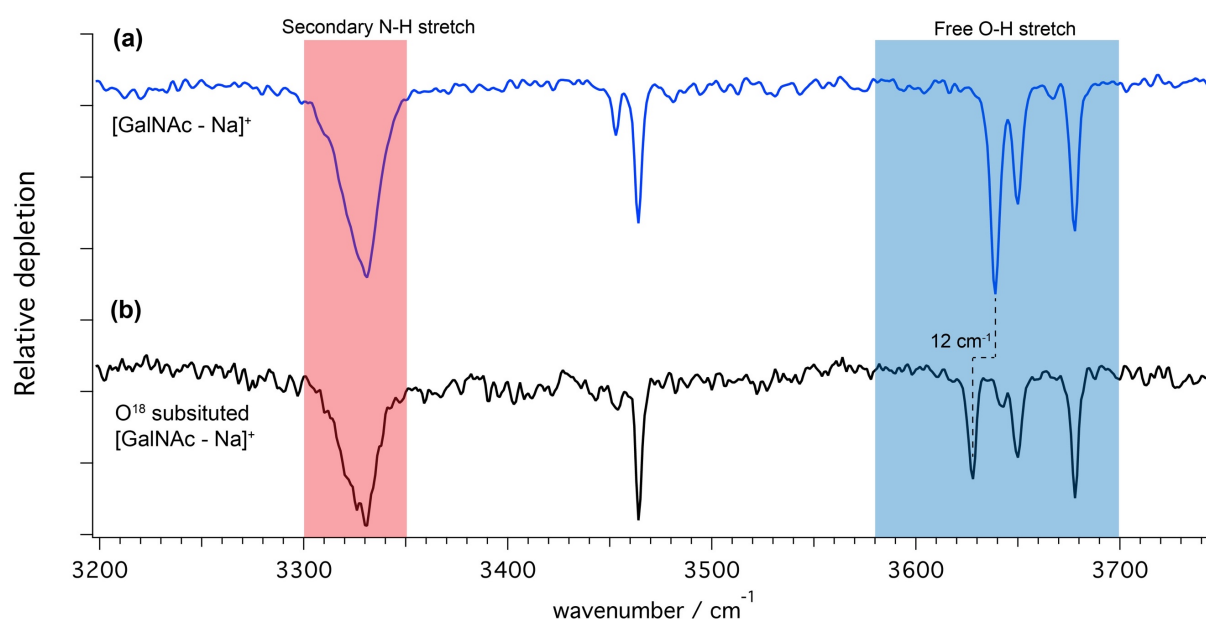


Figure 4.3: CryogenicIR spectra of the singly sodiated monosaccharide GalNAc. The spectral regions corresponding to different molecular oscillators are indicated. (a) the spectrum of the natural monosaccharide, (b) the spectrum of GalNAc with O¹⁸ labelling at the anomeric OH.

Although it is impossible to assign the OH bands based purely in intuition, we could expect the C6-OH to be the freest OH as it is somewhat removed from the rest of the molecule and therefore would therefore be in the free OH region. A study done by Schindler *et al* seems to support the idea that the C6-OH is among the freest in the OH region.¹⁴⁰ One hydroxyl which is easy to assign is the C1-OH. Dissolving the monosaccharide in H₂O¹⁸ will exchange the O¹⁶ of this carbon to the O¹⁸ isomer. This will change reduced mass of this OH oscillator, resulting in a shift in vibrational frequency corresponding to -12 cm⁻¹. This shift is clearly visible in Figure 4.3b, and we can therefore assign this band to the anomeric OH stretch.

4.5 Spectroscopic investigation of the anomeric retention of C fragments

We first tested anomeric retention in the C₁ fragments of Gal α (1-3)GalNAc and Gal β (1-3)GalNAc by comparing their cryogenic vibrational spectra (Figures 4.4a, d) with those of the methylated α and β anomers of galactose (Figures 4.4b, c).

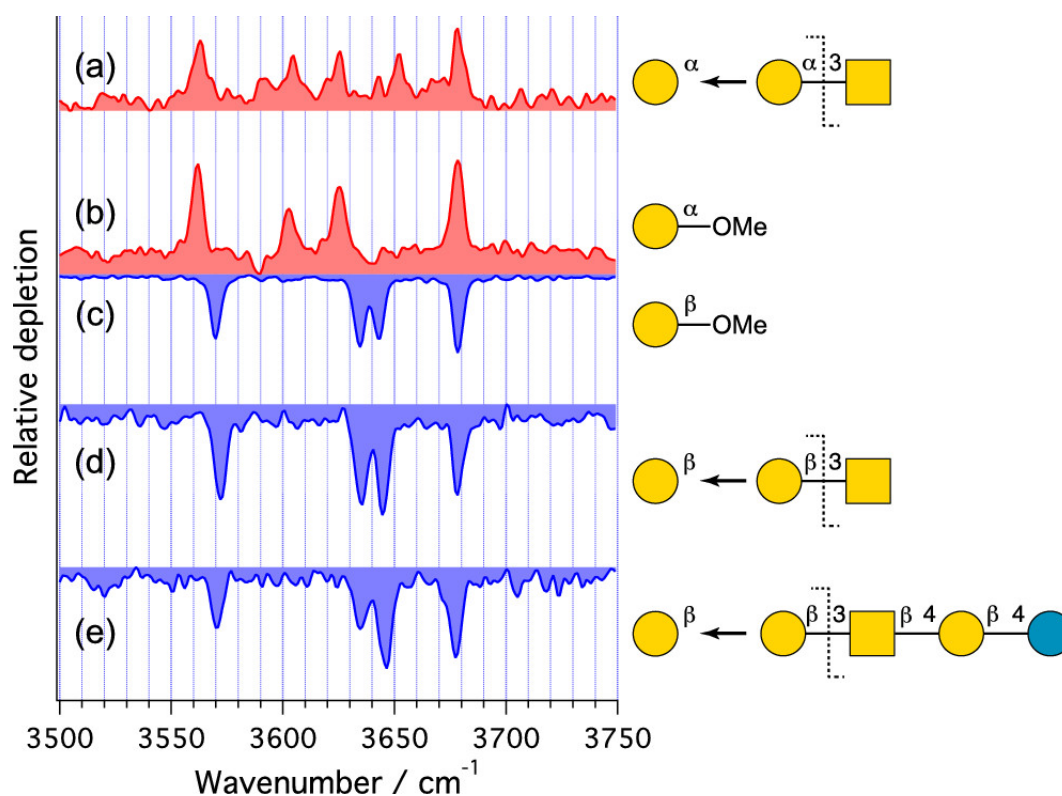


Figure 4.4: Cryogenic vibrational spectra of the C₁ fragments of galactose-containing disaccharides (a, d) and of a tetrasaccharide (e) and their comparison to the methylated anomers of galactose (b, c).

Because methylated galactose does not interconvert at the anomeric carbon, the spectra of the substituted monosaccharides should provide a good model of anomerically pure galactose, except for the absence of the anomeric OH stretch band, which occurs at 3652.5 cm⁻¹ in the α anomer and 3644.5 cm⁻¹ in the β anomer. Figure 4.4e shows the IR spectrum of the C₁ fragment generated from a tetrasaccharide Galβ(1-3)GalNAcβ(1-4)Galβ(1-4)Glc. All spectra of the C₁ fragment, which is itself an intact galactose, show a clear correspondence with those of the respective methylated galactose anomer. This demonstrates that C₁ fragments produced from an α glycosidic linkage represent the anomerically pure α monosaccharide, and that fragmentation of the β glycosidic linkage gives the anomerically pure β monosaccharide, irrespective of the size of the initial glycan.

To test whether anomer retention also occurs in N-acetylated C-fragments of glycans, we performed similar experiments on two disaccharides and a trisaccharide containing GalNAc at the nonreducing end. Figure 4.5 compares spectra of C₁ fragments to the isomer-specific spectra of the monosaccharide GalNAc obtained using an apparatus that employs ultrahigh-resolution IMS based on structures for lossless ion manipulations (SLIM)^{121, 141} to separate the two anomers before measuring their spectra.⁹²

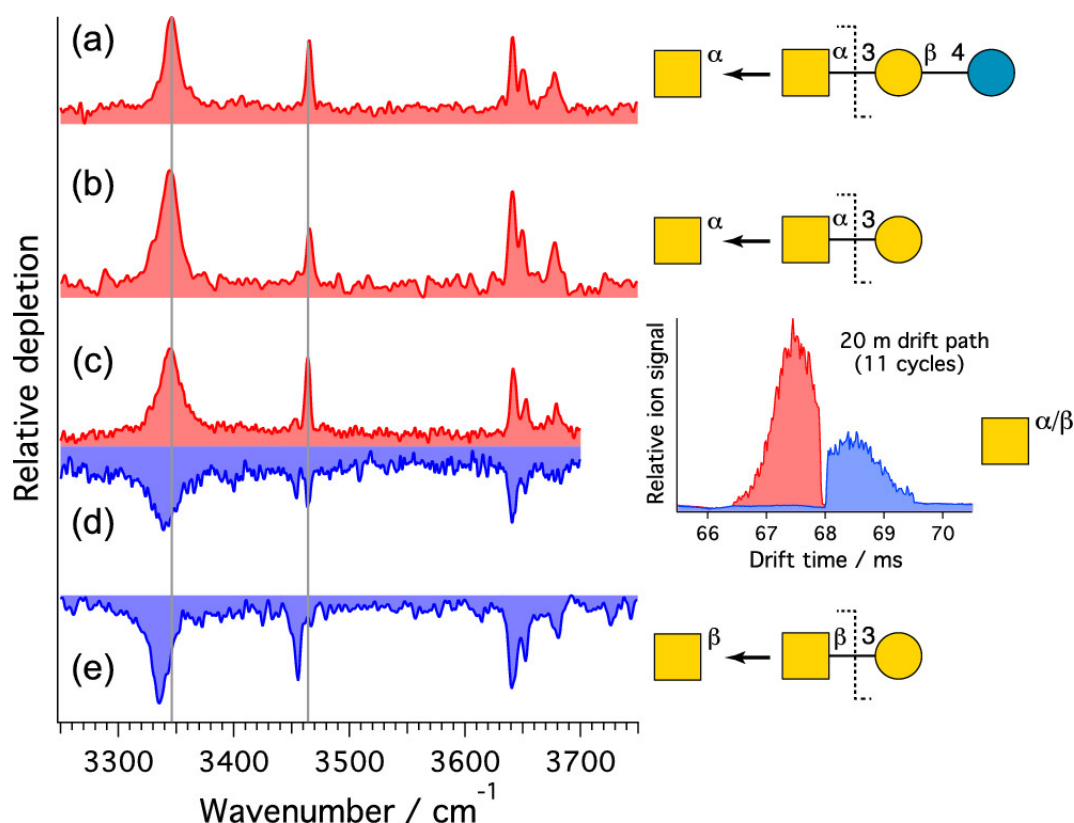


Figure 4.5: Cryogenic vibrational spectra of C_1 fragments of glycans with GalNAc at the nonreducing end. Inset: High-resolution arrival time distribution of GalNAc.

Two ion-mobility peaks for GalNAc were resolved after 11 cycles on the SLIM board, which represents a total drift path of ~ 20 m. The vibrational spectrum of the ions contained in the first mobility peak (Figure 4.5c) matches that of the C fragments generated from an α glycosidic linkage (Figures 4.5a, b), while the spectrum of the ions in the second mobility peak (Figure 4.5d) matches the fragment generated from a β glycosidic linkage (Figure 4.5e). It should be noted that because the two mobility peaks were not baseline separated, vibrational bands from the major component (Figure 4.5c) appear in the spectrum of the minor component (Figure 4.5d), but with reduced intensity. However, one can see that the peak at 3465 cm^{-1} , for example, is absent from the spectrum of Figure 4.5e, suggesting that the GalNAc fragment from GalNAc β (1–3)Gal is anomerically pure.

Although we have not assigned the two ion mobility peaks (inset, Figure 4.5c, d) to the α and β anomers, we have shown previously that for small sodiated saccharides structurally similar to those presented in this work, the two mobility peaks observed by ultrahigh-resolution IMS separation correspond to the α and β anomers.⁹² Furthermore, the fact that the spectrum of the C_1 fragment generated at an α glycosidic linkage corresponds exclusively to the spectrum from the first mobility peak, and likewise for the β fragment and second mobility peak, provides strong evidence that the two mobility peaks observed correspond to the α and β anomers. If mutarotation were to occur upon fragmentation, one would expect a mixture of anomers in the fragment spectra, which is not observed here. There is thus strong evidence that the presence of the N-acetyl group does not affect anomeric retention upon dissociation to form a C_1 fragment.

In order to evaluate the generality of anomeric retention further, analogous experiments were carried out on the C₂ fragments of the human milk oligosaccharides LNnT and LNnH. In Figure 4.6, we show the cryogenic vibrational spectra of the C₂ fragment from these species and compare them to the spectra of the α and β anomers of Gal β (1–4)GlcNAc (Figures 4.6a, b), which we separately measured after separation by SLIM-based ion mobility.¹⁴²

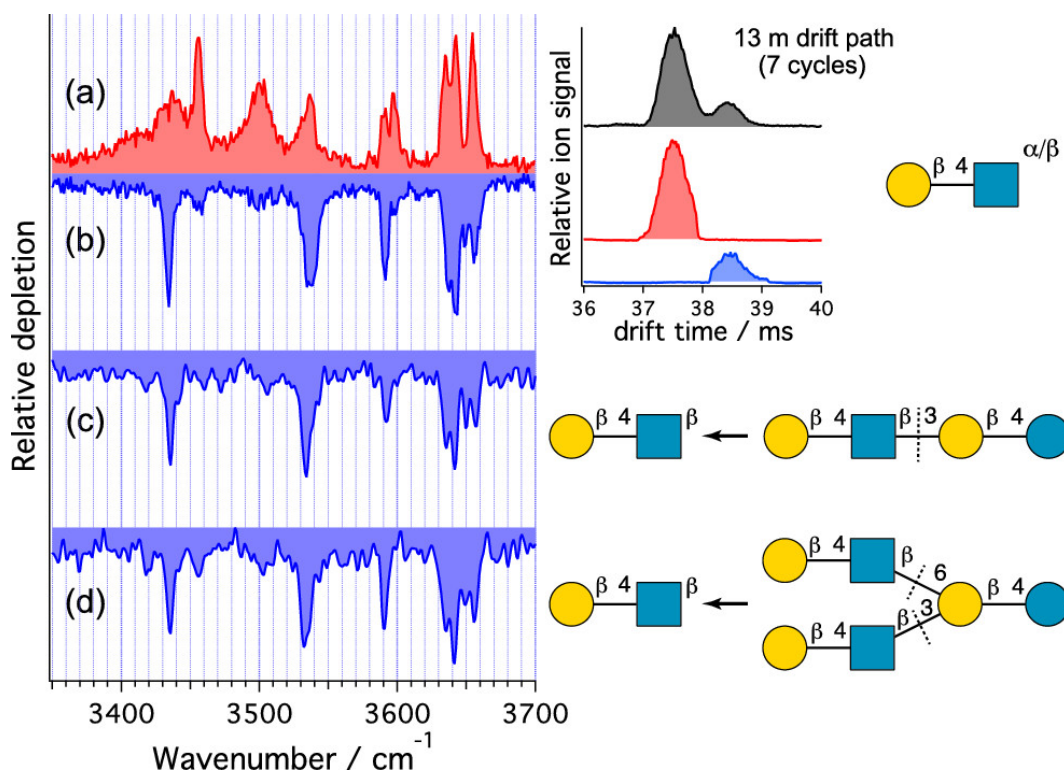


Figure 4.6: Cryogenic vibrational spectra of the C₂ fragments from LNnT (c) and LNnH (d) compared to those from the separated anomers of Gal β (1–4)GlcNAc (a, b). Inset: high-resolution arrival time distribution of Gal β (1–4)GlcNAc.¹⁴²

The spectra of the C₂ fragments from both LNnT (Figure 4.6c) and LNnH (Figure 4.6d) show a good match with the spectrum of the slower mobility peak of Gal β (1–4)GlcNAc (Figure 4.6b). This indicates that C₂ fragments of the linear tetrasaccharide LNnT and the branched hexasaccharide LNnH also retain the anomericity of the glycosidic bond.

These results clearly indicate that mutarotation does not occur for sodiated glycans in the gas phase under the collision energies used. This is in agreement with previous findings on sodiated sugars¹⁴³ and indicates that the barrier for gas-phase mutarotation of such cationized species must be significantly higher than those for fragmentation. A computational study performed on neutral, isolated tetrose saccharides reported activation barriers of mutarotation to be ~ 1.86 eV.¹⁴⁴ This is less than the fragmentation barriers which were calculated for sodiated disaccharides.^{124–125} It is therefore very likely that the cation plays an important role in increasing the barrier of mutarotation.

Furthermore, the process of ring closing in the gas phase to produce the opposite anomer is very unfavourable from an entropy viewpoint. It may be that ring opening does occur along with

fragmentation in some cases. This might account for the extra bands observed in Figure 4.4a, where both the α anomer of galactose and its open-ring form might be produced by CID. This is however not observed for any of the other C fragments, their spectra matching which all show the exact number of bands as their respective standards sprayed from solution and investigated under non-fragmenting conditions.

4.6 Spectroscopic identification of an ambiguous fragment

The tetrasaccharide LNnT produced a fragment at m/z 568 (Figure 4.2b) which could correspond to a C_3 or a Y_3 fragment. To identify this fragment, we measured its IR spectrum (Figure 4.7a) and compared it to that of the trisaccharide Gal β (1–4)GlcNAc β (1–3)Gal (Figure 4.7b), which would have the same structure as the C_3 fragment. The two spectra in Figure 4.7 are very different, with almost no matching band positions. This indicates that the m/z 568 fragment is not C_3 , but the Y_3 fragment, and therefore does not carry any information on the anomericity of the glycosidic bond that was broken to form the fragment.

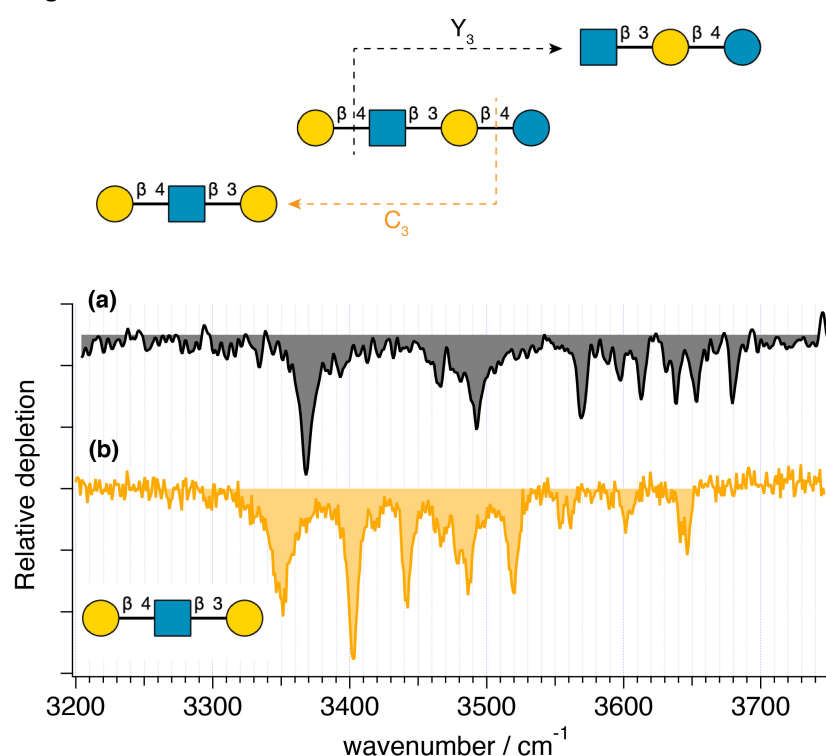


Figure 4.7: Cryogenic IR spectrum of m/z 568 fragment generated from LNnT and corresponding to two possible structures, C_3 and Y_3 (a). IR spectrum of the trisaccharide Gal β (1–4)GlcNAc β (1–3)Gal with the same structure as the C_3 fragment from LNnT (b).

4.7 Conclusions

Our results on sodiated glycan fragments extend the findings by Compagnon and coworkers⁸² in a significant way. The higher spectroscopic resolution afforded by cryogenic IR spectroscopy, together with ultrahigh-resolution ion mobility, provides us with the capability of identifying the anomeric forms of larger CID fragments by comparing them to anomERICALLY pure reference compounds. Our observation of anomer retention in the fragmentation of glycans as large as hexasaccharides (Figure

4.6d) and the fact that it occurs for fragments larger than C₁ (Figure 4.6c and 4.6d) suggest that it may be the rule rather than the exception, arising from the large barriers for mutarotation in the gas phase. If further studies confirm this generality, it would open new possibilities for determination of the primary structures of biologically relevant glycans and provide an important new tool for glycomics.

5. A new glycan sequencing strategy coupling ion-mobility-selected CID and messenger-tagging IR spectroscopy

Ultra-high resolution ion mobility spectrometry (IMS) can achieve the separation of glycan isomers that differ only in the anomericity of a single glycosidic bond. Adding a spectroscopic dimension allows for these separated structures to be identified based on their vibrational fingerprints. However, every reducing sugar in solution consists of a mixture of α and β anomers at the reducing end, which can also be separated by ultra-high resolution IMS. Being able to determine which mobility peaks observed in IMS come from the α and β reducing anomers and to be able to get a spectroscopic fingerprint for these anomerically pure species gives a twofold advantage:

1. It to distinguish which mobility peaks separated by IMS come from differences in the glycosidic linkage, and which arise from reducing end anomers. The former indicates the presence of different glycan structures which is biologically important, while the latter can be disregarded from a biological point of view.
2. The spectra of isolated α and β reducing anomers can be used as standards to identify C-fragments that retain the anomericity of the glycosidic bond as discussed in Chapter 4. This circumvents the need to purchase standards which have been locked into either the α or β configuration by permethylation at the reducing end, such standards often being very costly and challenging to produce.

The work presented in this chapter is centered around the fact that Y-fragments are intact glycans that carry the reducing end OH. A mid-sized glycan may separate into its α and β reducing anomers by ion mobility, but unless we have the corresponding reducing-end permethylated standards, it is impossible to spectroscopically determine which one is which. Although such anomerically pure standards are rare or even non-existent for sugars containing three or more saccharide units, they are easily obtainable for some common mono- and disaccharides. Therefore, a Y_1 or a Y_2 fragment were to be generated from a parent glycan which has been mobility-separated into its two reducing anomers, the spectra of the fragment could be matched to that of an anomerically pure standard and therefore the separated parent species identified. The spectra of each reducing anomer of the parent can then be added to our spectral database and used to further glycan studies.

5.1 Introduction

The combination of IMS with tandem MS methods have allowed for the separation, and in some cases identification, of various glycan isomers. For instance, a cyclic IMS instrument has been recently used to separate and partially identify the isomers of a set of pentasaccharides based on their fragmentation pattern.¹⁴⁵⁻¹⁴⁶ Although providing significant advances in the field of glycan analysis, IMS-MS studies alone are unable to provide unambiguous identification of all the possible isomers, such as assigning a specific drift peak to a single reducing-end anomer.

Combining IMS with cryogenic messenger tagging spectroscopy has allowed our group to distinguish between the various isomers present within a certain glycan.¹⁴⁷ Nevertheless, the vast number of possible structures make it challenging to interpret complex vibrational spectra of larger oligosaccharides and determine the specific isomeric form. Moreover, the size of most glycans put them out of reach of current theoretical methods that are typically used to associate vibrational bands to a certain structure. This problem can be overcome by using a database of spectral fingerprints constructed using glycan standards,⁹²⁻⁹³ however it is often difficult to obtain standards of pure isomeric forms.

Breaking down glycans into smaller fragments by CID prior to spectroscopic investigation can simplify the interpretation of the spectra. This approach relies on breaking the molecule of interest into C- or Y-type fragments,¹⁰³ which are themselves intact glycans, and then matching their IR spectra to a database of known standards. As has been shown in the previous chapter, this technique has revealed that for alkali metal complexed C-type fragments, the anomericity of the glycosidic linkage is retained.^{72, 82, 112, 148} However, many glycosidic linkages preferentially produce B- or Y-type fragments rather than C-type fragments, and this is a limiting factor to using only the latter to sequence glycan structure. In this work, we explore how Y fragments, which carry the anomeric OH, can be used to assign the anomers of a set of mobility-separated oligosaccharides. In this chapter, we show a systematic approach, combining mobility-selective CID and cryogenic IR spectroscopy, which can identify the anomers of large glycans using only a small set of anomerically pure and commercially available mono- and disaccharide standards. The spectra of the precursor molecules can then be assigned to a single anomer and added to our database, providing us with a spectral library of complex molecules for which anomerically pure standards are often unavailable.

5.2 Experimental approach

Experiments were run on a home-built instrument that couples SLIM-based IMS to a tandem mass spectrometer, equipped with a cryogenic octupole ion trap, as described in Chapter 2.2. Fragmentation can be achieved through collisions in the SLIM ion guide at a pressure of 10^{-1} mbar by increasing the potential difference between the IMS bias and the ion guide entrance to ~ 120 V.

The oligosaccharides galacto-N-biose (Gal β 1-3GalNAc), N,N'-diacetylchitobiose (GlcNAc β 1-4 GlcNAc), methyl 2-acetamido-2-deoxy- α -D-glucopyranoside (GlcNAc- α -OMe), methyl 2-acetamido-2-deoxy- β -D-glucopyranoside (GlcNAc- β OMe), lactose, and lactose were purchased from Carbosynth (UK). The trisaccharide Man-1 and the tetrasaccharide lacto-N-neotetraose (LNnT) were purchased from Dextra (UK). The disaccharides methyl- α -lactoside and methyl- β -lactoside were purchased from Synthese (Canada). All samples were used without further purification and diluted in a 50:50 water-methanol solution to a concentration of ~ 70 μ M. Only the singly sodiated cations were investigated in this work. Helium was used as both a drift gas for IMS and collision gas for CID, while a He/N₂ mix (90:10) was pulsed into the cryogenic ion trap for both cooling and messenger tagging.

5.3 Spectroscopic study Y fragments generated by CID of mobility-selected precursors

Evidence of mobility-selected CID. The singly sodiated trisaccharide Man-1 ($m/z = 609$), which is part of the core structure for all N-glycans¹⁴⁹, was fragmented on a commercial Q-TOF (Waters Premier)

and its major fragments identified (Figure 5.1A). The trisaccharide was then resolved into two peaks after a single pass on the SLIM board of our home-built instrument, corresponding to a 7.5 meter pathlength (Figure 5.1B). This is in accordance with the distributions observed in ion mobility studies of similar reducing sugars and has been speculated, and in some cases confirmed, to be due to the α and β anomers.^{80, 91, 145} To search for CID products, the first quadrupole was set to the expected fragment masses from Figure 5.1A, and the potential difference between the SLIM bias and SLIM ion guide entrance was increased until fragments were observed (Figure 5.1C). Optimal fragmentation was achieved for a voltage difference of $\sim 120\text{V}$ at a pressure of $\sim 10^{-1}$ mbar.

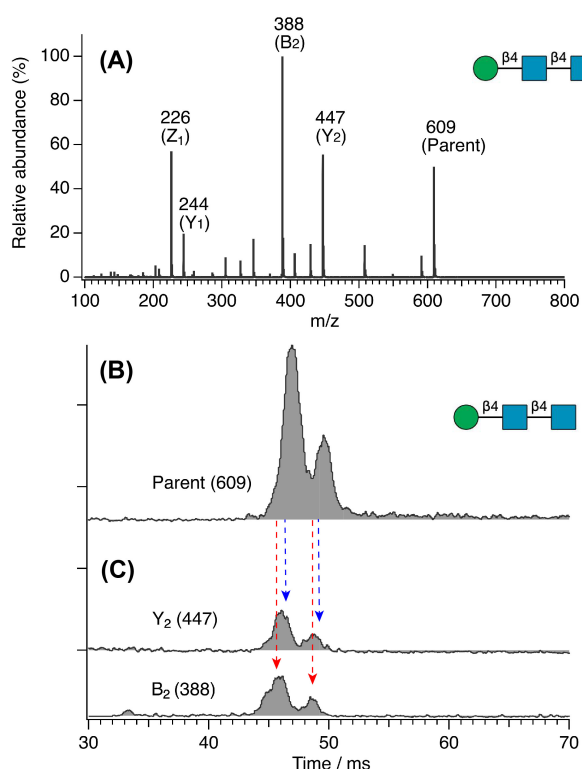


Figure 5.1: (A) Fragmentation pattern of $[\text{Man-1+Na}]^+$, measured on a Q-ToF Premier (Waters). (B) ATD of $[\text{Man-1+Na}]^+$ measured after one cycle on the SLIM-IMS device. (C) Fragments generated from the mobility-separated parent after the IMS stage corresponding to the fragments observed on the Q-TOF.

The sodiated Y_2 ($m/z = 447$) and B_2 ($m/z = 338$) fragments were observed. The fact that they arrive at the same time as the parent molecule excludes the possibility that these species are generated in solution, as they would have separated from their precursors due to their distinct mobility. This confirms that they correspond to fragments of the mobility-separated trisaccharide.

5.3.1 Disaccharide Gal(β -4)GalNAc

To test our ability to identify mobility-separated anomers based on the IR spectra of their Y fragments, we chose a simple disaccharide, galacto-N-biose, which is a core structure of mucin-type O-glycans.¹⁵⁰ Its arrival-time distribution was resolved into two peaks after two cycles along the SLIM separation path (Figure 5.2A).

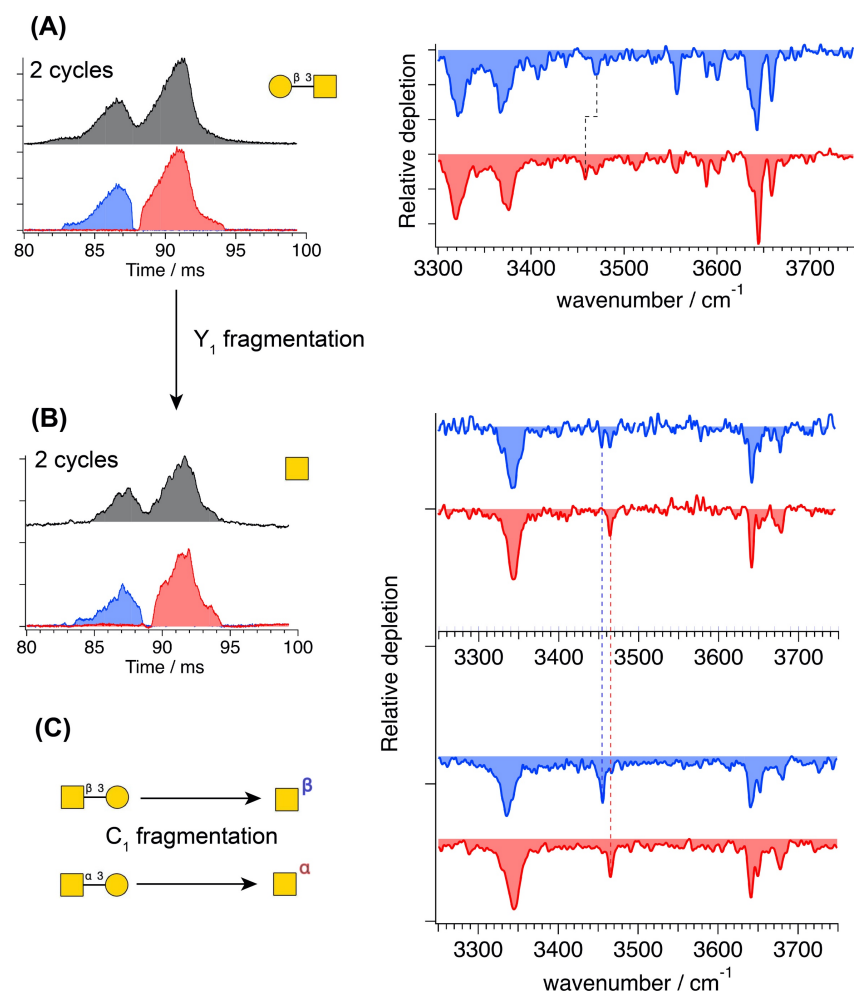


Figure 5.2: (A) Arrival-time distribution of the sodiated disaccharide Gal(β-3)GalNAc after two SLIM cycles and the associated IR spectra. (B) IR spectra of the Y₁ fragments, GalNAc, generated from each mobility peak of the disaccharide. (C) Anomerically pure IR spectra of GalNAc generated by C₁ fragmentation of the disaccharides GalNAc(α-3)Gal and GalNAc(β-3)Gal. Red indicates the α anomer and blue the β anomer, assigned after comparing the spectra of the Y₁ fragments to the anomerically pure standards.

These two mobility peaks give distinct IR spectra, with the first (blue) having a strong band at 3557 cm⁻¹ which is attenuated in the IR spectrum of the second (red) mobility peak. Moreover, the band at 3471 cm⁻¹ in the spectrum of the first mobility peak shifts to 3458 cm⁻¹ in that of the second. To determine whether the two mobility peaks of Figure 5.2A correspond to different anomers of the disaccharide, we measured infrared spectra of the Y₁ fragments generated from each one (Figure 5.2B). We then compared them to spectra of pure anomers of GalNAc (Figure 5.2C), which were generated by C₁ fragmentation of the reverse sequence disaccharides, GalNAc(α-3)Gal and GalNAc(β-3)Gal, and which retain the anomericity of the glycosidic bond.³⁴ The spectrum of the Y₁ fragment from the first mobility peak shows a clear band at 3454 cm⁻¹, which is the signature feature in the spectrum of the β anomer, while the Y₁ fragment coming from the second mobility peak shows a distinct band at 3464 cm⁻¹, identifying it as the α-anomer (Figure 5.2C). Based on the baseline mobility of the two species, contamination from one peak to the other seems very unlikely. Therefore, the

band at 3464 cm^{-1} in the Y_1 fragment from the first mobility peak (blue) most likely comes from a second conformer within the β anomer, with a vibration which happens to coincide with the position of the α -anomer. This phenomenon has already been observed during double resonance experiments performed on protonated glucosamine and should be kept in mind as a potential limitation for spectroscopic identification.¹⁵¹ Nevertheless, we conclude that the first mobility peak of the sodiated disaccharide parent molecule, galacto-N-biose, comes from the β -anomer while the second mobility peak is from the α -anomer, allowing us to associate the corresponding IR spectra to each anomer. These can now be added to a spectroscopic database as identifiers of the α - and β -anomers of galacto-N-biose.

5.3.2 Trisaccharide MAN-1

As shown in Figure 5.1B, Man-1 can be separated into two mobility peaks after a single pass. The IR spectrum of each peak is similar yet distinct (Figure 5.3A). Since anomerically pure standards for Man-1 are not readily available, identification of these two species is performed by examining their fragments. The Y_2 fragments were generated from each mobility peak and their IR spectra measured (Figure 5.3B). Although very similar, the relative intensities of the bands at 3433 cm^{-1} and 3457 cm^{-1} can be used to distinguish them. The species corresponding to the faster peak in the ATD (red) has a weak band at 3433 cm^{-1} in its IR spectrum followed by a strong band at 3457 cm^{-1} , whereas the slower peak in the ATD (blue) has a strong band at 3433 cm^{-1} followed by a weak band at 3457 cm^{-1} .

These spectra were then compared to those of the corresponding disaccharide, N,N'-diacetylchitobiose, mobility-separated after two cycles (Figure 5.3C). By matching these spectra to those of the Y_2 fragments, we conclude that the first mobility peak of Man-1 corresponds to the second mobility peak of N,N'-diacetylchitobiose and second mobility peak of Man-1 to the first mobility peak of N,N'-diacetylchitobiose. This seeming inversion is because the Y_2 fragments carry the ATD of the parent molecule and therefore do not correspond the drift time of N,N'-diacetylchitobiose. These assignments are based on spectra that differ only in the relative intensities of the bands. This is not what is typically expected from the IR spectra of reducing anomers, where a shift in band position is commonly observed. We must therefore be cautious when drawing these conclusions, and work currently is being carried out to confirm whether the species separated in these experiments are indeed the reducing anomers.

Finally, Y_1 fragments of the mobility-separated N,N'-diacetylchitobiose were generated (Figure 5.3D). Since the C_1 and Y_1 fragments of this disaccharide are isomeric, a separate experiment was carried out in which the reducing end hydroxyl was labelled with O^{18} and the CID spectrum taken in our Q-TOF. A shift of the fragment at mass from 244 to 246 was observed (see Figure 5.4), leading to the conclusion that Y_1 fragments were being formed, since C_1 fragments would not have been affected by the isotopic label. The IR spectra of the Y_1 fragments were then compared to those of the anomerically pure methylated monosaccharides, GlcNAc- α -OMe and GlcNAc- β -OMe (Figure 5.3E). The methylation of the reducing end OH prevents the mutarotation in solution, locking the sugar into a single anomer. From the bands at 3447 cm^{-1} , 3528 cm^{-1} , and 3549 cm^{-1} we conclude that the Y_1 fragment from the second mobility peak matches the spectrum of GlcNAc- α -OMe, indicating that this is the α -anomer. The absence of these signature bands in the Y_1 fragments from the first peak suggests that this is the β -anomer. It is worth mentioning that the spectra of the Y_1 fragments possess a clear band at 3640 cm^{-1} , which is absent in spectra of the methylated standards, and this is due to the reducing end OH

band as has been observed in previous studies.^{29,35} Furthermore, GlcNAc- β OMe has an extra band at 3427 cm^{-1} , which is not present in the fragment IR spectrum. This may be due to slight structural changes resulting from the methyl group replacing the hydrogen on the reducing end.

Using this result, we can work backwards, assigning every mobility peak and every IR spectrum to either the α -anomer (coded red) or the β -anomer (coded blue), providing a wealth of anomer-specific spectra that can be added to our database and serve as building blocks when analyzing larger N-glycans.

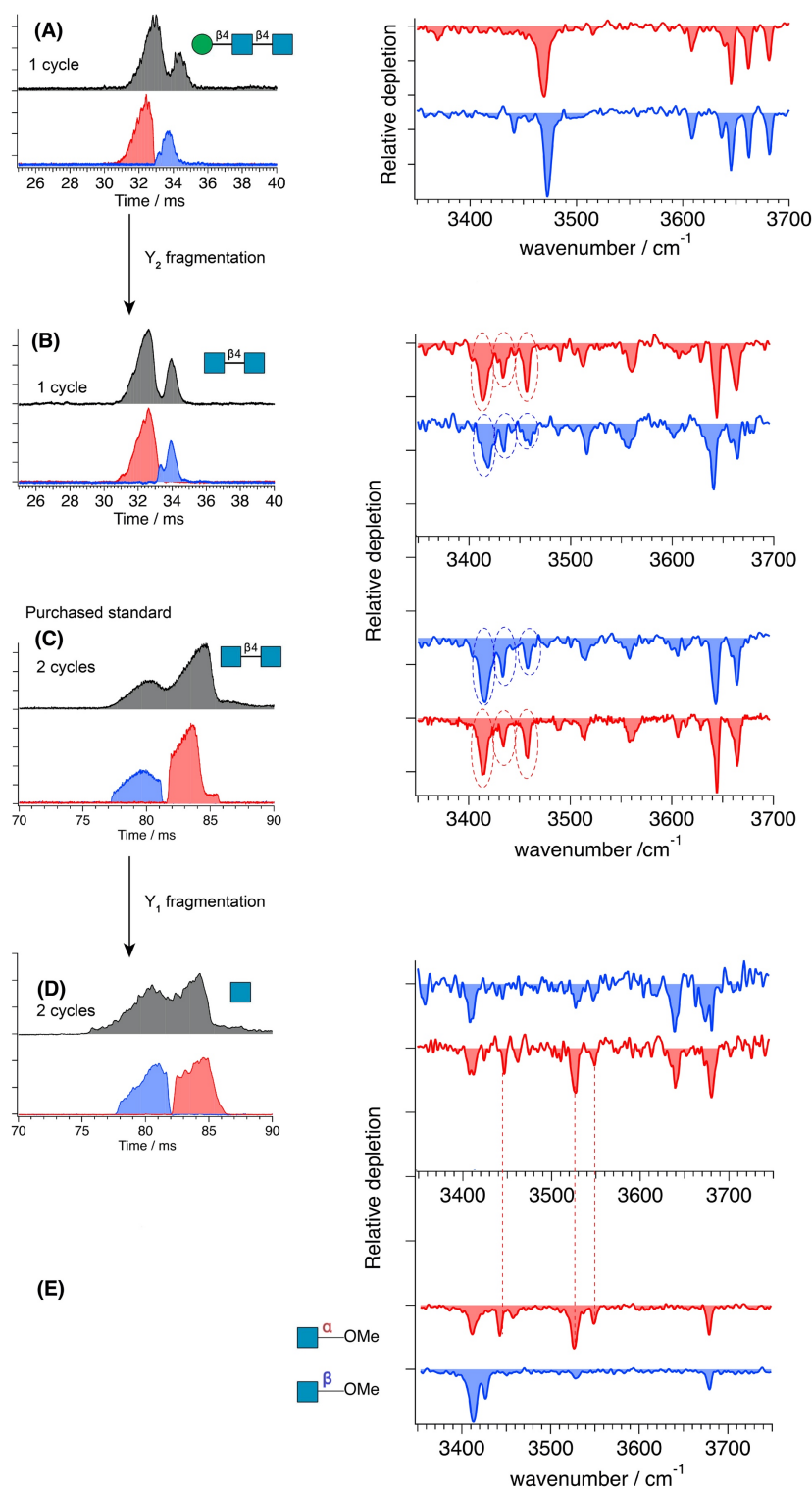


Figure 5.3: (A) Mobility-separated IR spectra of the precursor trisaccharide [Man-1+Na]⁺. (B) Spectra of the Y₂ fragments generated from the mobility-separated precursor. (C) Mobility separation and IR spectra of the purchased standard N,N'-diacetylchitobiose corresponding to the Y₂ fragment. (D) Spectra of the Y₁ fragment generated from the mobility separated N,N'-diacetylchitobiose. (E) IR spectra of anomerically pure monosaccharides GlcNAc- α -OMe and GlcNAc- β -OMe. Red indicates identified α anomers and blue the β anomers.

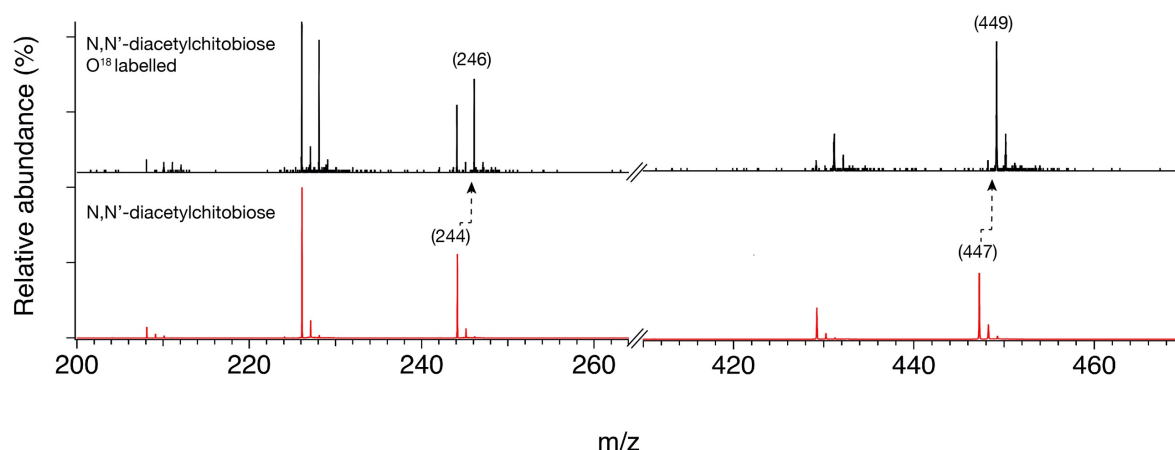


Figure 5.4: Fragmentation studies of O^{18} labelled N,N' -diacetylchitobiose performed on a Q-ToF (Waters Premier). The shift of the fragment from m/z 244 to 246 indicates that it is a Y fragment, as O^{18} substitutes the oxygen at the reducing end.

5.3.3 Tetrasaccharide LNnT

To extend our method to a larger, more complex oligosaccharide, we investigated the human milk tetrasaccharide, LNnT. Separating into two well-resolved peaks after two cycles, the ATD indicates the presence of two isomers with distinguishable IR spectra (Figure 5.5A), which we believe to be the α and β reducing-end anomers. To assign them, we apply the same procedure of breaking the mobility-separated species into fragments for which we have anomerically pure standards. The relevant fragment produced by CID of the mobility-separated LNnT is the Y_2 fragment, corresponding to the common disaccharide lactose. The IR spectra of the fragments (Figure 5.5B) are clearly distinguishable, with one band shifting from 3558 cm^{-1} in the spectrum of the faster peak in the ATD (blue) to 3545 cm^{-1} in the second peak (red), and the two highest frequency bands being inverted in their relative intensities. These spectra were compared to those of the anomerically pure methyl- α -lactoside and methyl- β -lactoside (Figure 5.5C). The band at 3545 cm^{-1} clearly identifies the second peak as the α -anomer, while the band at 3558 cm^{-1} identifies the first peak as the β -anomer. The small blue shift ($+4\text{ cm}^{-1}$) of these bands in the methylated standards as well as the differences in the 3630 cm^{-1} to 3660 cm^{-1} range can be attributed to the OMe group replacing the OH at the anomeric carbon, which has an effect on the coupled network of OH oscillators.

These results confirm that the isomers of the parent LNnT separated by ion mobility are indeed the two reducing-end anomers, and that the first peak in the ATD corresponds to the β -anomer while the second peak is the α -anomer. Furthermore, the anomer-specific IR spectra of both lactose and LNnT that we obtained can be used in a spectroscopic database for analyzing human milk oligosaccharides.

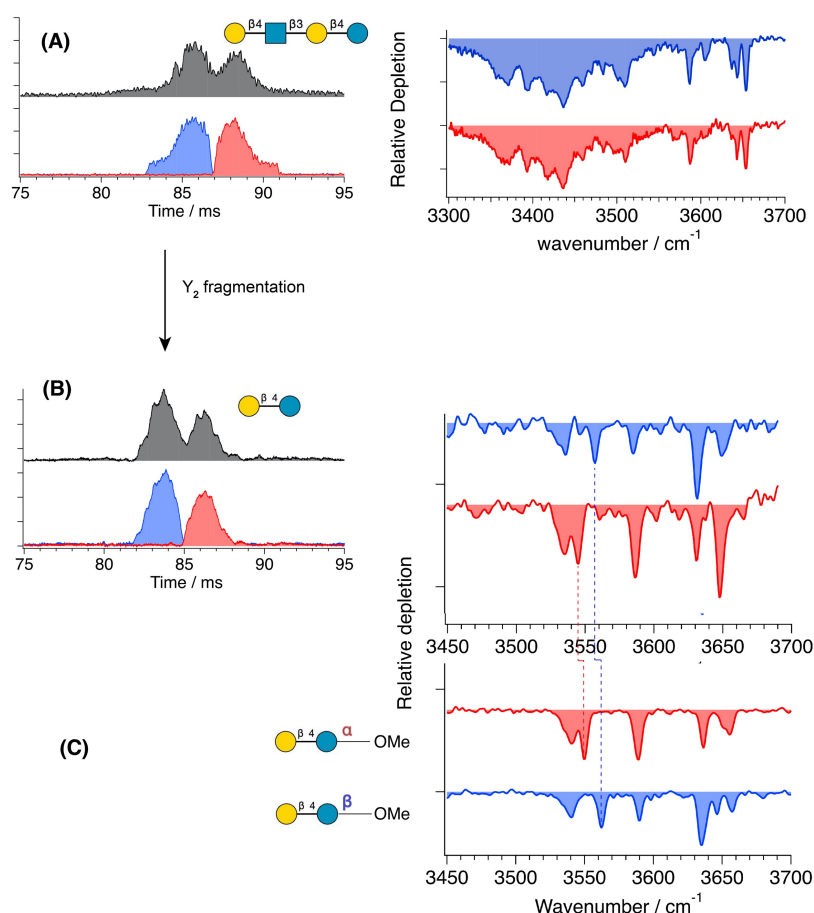


Figure 5.5: Mobility separation and corresponding IR spectra of the precursor $[\text{LNnT}+\text{Na}]^+$ (A), IR spectra of the Y_2 fragments (lactose) generated from the mobility-separated precursor (B), and the anomerically pure IR spectra of methyl- α -lactoside and methyl- β -lactoside (C). Colours red and blue indicate identified α and β anomers, respectively.

5.3.4 Pentasaccharide maltopentaose

Maltopentaose is commonly used in the preparation of dextran ladders for capillary electrophoresis.¹⁵² After two cycles on the SLIM board, singly sodiated maltopentaose separates into three peaks. The IR spectra of the first two peaks were measured and show clear, distinct features (Figure 5.6A). The ATDs obtained are similar to those found for maltopentaose in previous ultra-high resolution ion mobility studies, and it is believed that the two major peaks come from the reducing anomers, while the third peak may come from an open-ring configuration.^{141, 146} To test this, we measure the IR spectra of the Y_4 fragments generated from the major mobility peaks of the parent molecule (Figure 5.6B). Previous O^{18} labelling experiments have confirmed that the fragment is Y_4 and not C_4 which would have the same mass.²⁴ The spectra of the Y_4 fragments were compared to the mobility-separated spectra of maltotetraose, which is the corresponding tetrasaccharide (Figure 5.6C). A comparison shows that the spectrum of the Y_4 fragment generated from the first mobility peak of the parent corresponds to that of the second mobility peak of maltotetraose, with distinct bands matching at 3438, 3463, and 3511 cm^{-1} . The spectrum of the Y_4 fragment generated from the second mobility peak of the parent glycan matches that of the first mobility peak of maltotetraose,

with their unique bands matching at 3426, 3469, and 3516 cm^{-1} . We therefore conclude their structural correspondence, and the seeming inversion is merely due to the fact that the Y_4 fragments carry the mobility of the parent molecule.

Only the first IMS peak of maltotetraose was fragmented due to the low abundance of the second peak. The Y_2 fragment, corresponding to the common disaccharide maltose, was generated and its IR spectrum measured (Figure 5.6D). A separate MS^2 experiment involving O^{18} labelling of the reducing was carried out on our Q-Tof to confirm that the Y_2 fragment was being formed and not the C_2 (Figure 5.7). This spectrum was then compared to the spectra of the anomerically pure methyl- α -maltoside and methyl- β -maltoside (Figure 5.6E). The band positions at 3505, 3600, and 3640 cm^{-1} clearly identify the Y_2 fragment as being the β reducing anomer. This indicates that first mobility peak of maltotetraose, as well as the second mobility peak of maltopentaose, are the β anomers. This supports the claim that the two major mobility peaks of maltopentaose are due to the α and β reducing anomers by identifying the second mobility peak as the β anomer.

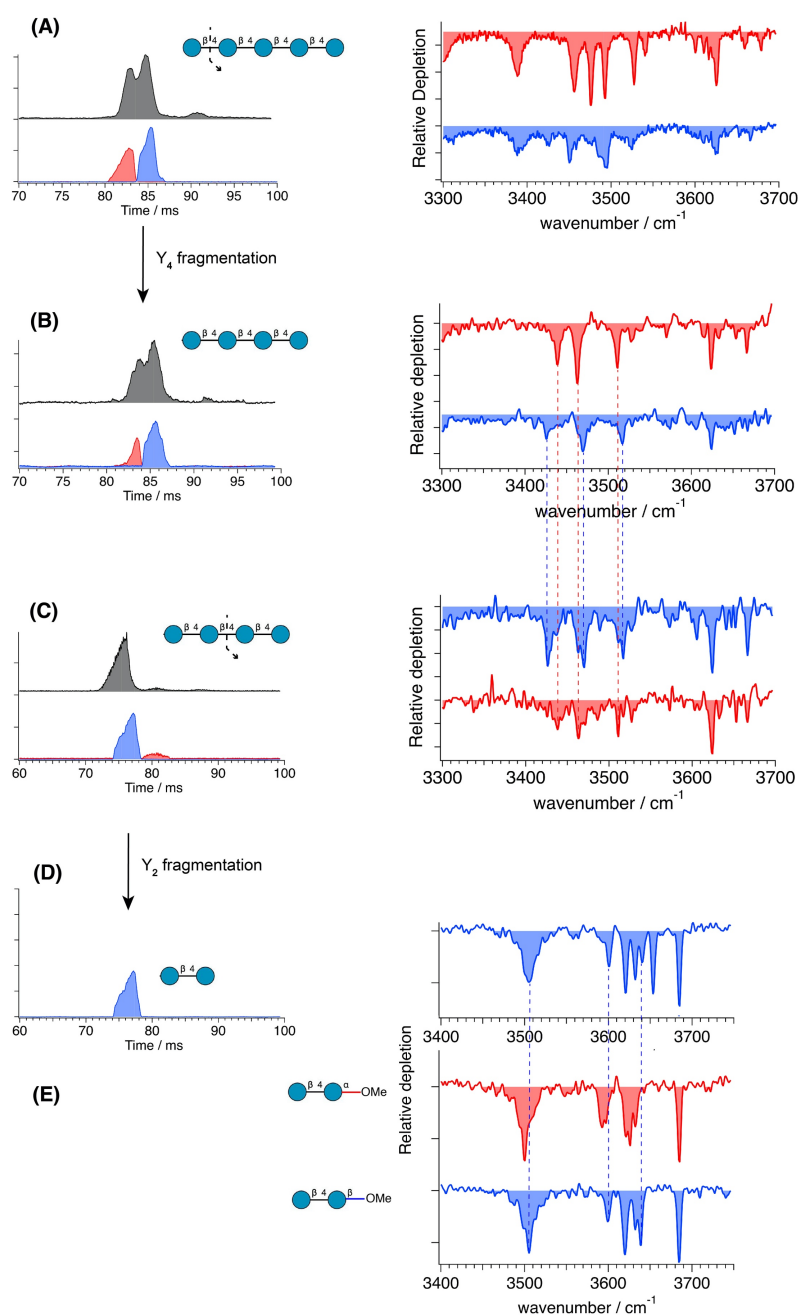


Figure 5.6: Mobility separation and IR spectra of the singly sodiated precursor, maltopentaose (A). IR spectra of the Y₄ fragments (maltotetraose) generated from the mobility separated precursor (B). Mobility-separated IR spectra of singly sodiated purchased standard maltotetraose (C). IR spectrum of the Y₂ fragment (maltose) generated from the first mobility peak of maltotetraose (D), and comparison with anomerically pure methyl- α -maltoside and methyl- β -maltoside (E).

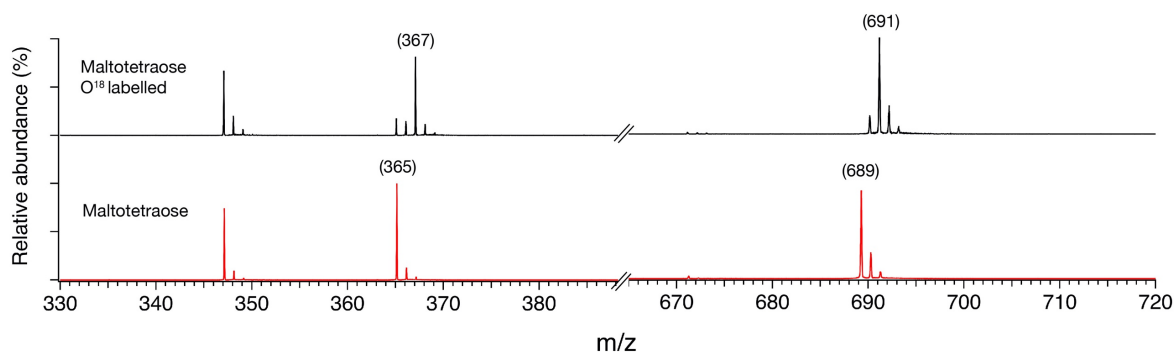


Figure 5.7: Fragmentation studies of O¹⁸ labelled maltotetraose performed on a Q-Tof (Waters Premier). The shift of the fragment from m/z 365 to 367 indicates that it is a Y fragment, as O¹⁸ substitutes the oxygen at the reducing end.

5.4 Comparison of mobility-separated disaccharides to their permethylated standards

In the previous section, the studies of LNnT and maltopentaose were not fragmented to a monosaccharide for the reducing-end anomers to be assigned. The reason for this is that the disaccharides corresponding to the Y₂ fragments (namely lactose and maltose), give a mixture of C₁ and Y₁ fragments upon collision-induced dissociation, which, have the same mass. For this reason, corresponding disaccharides, with the reducing end locked into a single anomer by permethylation, were used to identify the anomericity of the Y₂ fragments. This leads to an interesting question: if we mobility-resolve the non-methylated disaccharides in our IMS device, how will their spectra compare to those of the anomERICALLY pure standards?

Singly sodiated lactose separated after one cycle on the SLIM board into two baseline resolved peaks, each giving a distinct IR spectrum (Figure 5.8A), analogous to those obtained from the Y₂ fragment of LNnT (Figure 5.5B). When compared to the IR spectra of methyl- α -lactoside and methyl- β -lactoside (Figure 4.8B), we observe the same characteristic band at 3545 cm⁻¹ that identifies the second mobility peak to be the α anomer. Similarly, the band at 3558 cm⁻¹ identifies the first mobility peak as the β anomer and we observe the same 4 cm⁻¹ shift in the positions of these bands with respect to the methylated standards, as observed when comparing the Y₂ fragments of LNnT. We therefore conclude that the two mobility peaks of lactose, resolved on our SLIM device correspond to the α and β anomers, with the first peak being the β anomer and the second peak being the α anomer.

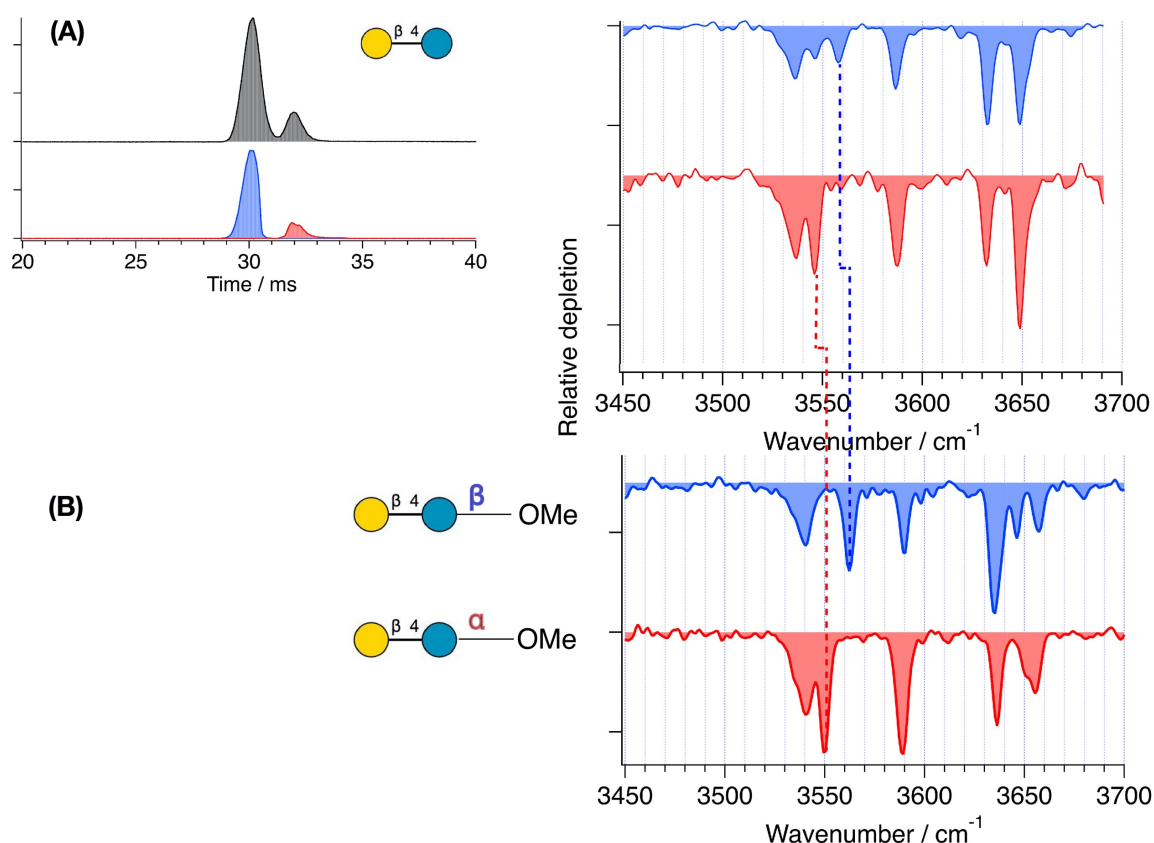


Figure 5.8: Mobility separation and IR spectra of singly sodiated lactose (A). Comparison with the anomerically pure IR spectra of methyl- α -lactoside and methyl- β -lactoside (B). Red and blue indicate the identified α and β anomers respectively.

The same experiment was performed on singly sodiated maltose, but unlike the other molecules studied in this chapter, maltose separated into three mobility peaks of comparable intensity after a single pass on the SLIM device (Figure 5.9A). The IR spectra of each of these mobility peaks were measured, the first and third giving very similar spectra, while the spectrum of the middle peak was distinct. When compared to the anomerically pure permethylated standards (Figure 5.9B), the band positions at 3504 cm^{-1} and 3590 cm^{-1} indicate that both the first and third mobility peaks both share the structure of the α anomer. This is further supported by a lack of the band at 3640 cm^{-1} , which is a clear identifier of the β anomer. This indicates a behaviour that has not been observed so far, two molecules with the identical primary structure arriving at different drift times. This could be attributed to the α anomer having two conformers which separate during IMS, but the similarity of the two spectra make this explanation unlikely, as two conformers which are different enough to be easily separated by IMS should show more spectral differences than what is observed here. A more likely explanation is that a fraction of the α anomer travels through the SLIM as either as a dimer or as a solvent adduct, which then breaks into the bare monomer upon entering the lower pressure regions. This will result in the α anomer appearing at two different drift times as is observed here, one corresponding to the drift time of the bare molecule and the other to that of its dimer or solvent adduct. If this is indeed the case, then the process of dimerization or cluster formation must be anomer specific, since this is only observed for the α anomer. The β anomer is clearly identified as the middle peak in the ATD.

Closer inspection of the spectra of the first and third mobility peaks show that they are not completely identical. The main differences lie in the relative intensities of the relative at 3620 cm^{-1} and 3630 cm^{-1} which are slightly inverted, as well as the band at 3504 cm^{-1} which is narrower in the spectrum from the first peak. These slight differences may indicate that the two species, although both the α anomer, may have a slightly different three-dimensional structures due to the fact that one of them may have travelled through the SLIM path while being complexed to some other molecule, which then separated from the ion on entering high vacuum. However, no definitive conclusion can be drawn from the current data, and further investigations should be carried out if similar situations are encountered in the future.

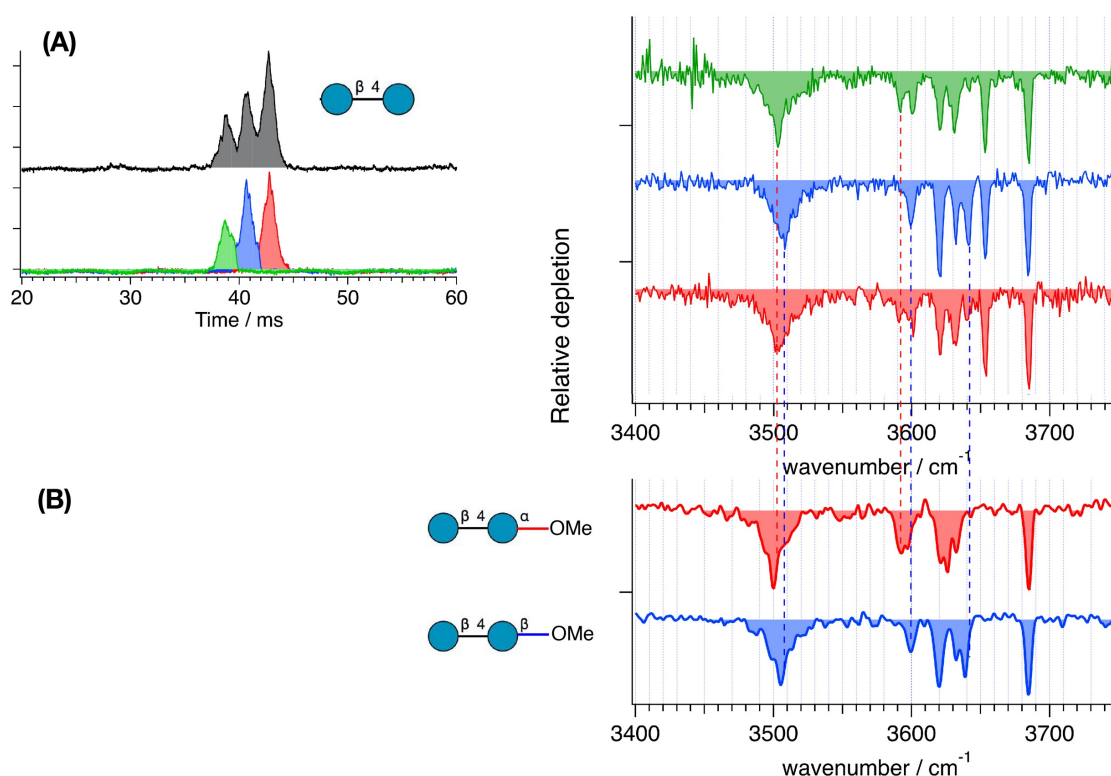


Figure 5.9: Arrival time distribution of sodiated maltose and the IR spectrum of each sliced peak (A). Comparison to the anomerically pure methyl- α -maltoside and methyl- β -maltoside (B).

5.5 Conclusions

In this work, we have demonstrated how the combination of ion-mobility-selective CID with cryogenic IR spectroscopy can be implemented in a sequential manner to identify the reducing-end anomers of biologically relevant oligosaccharides. By exploiting the fact that Y fragments retain the anomeric information of their parent structures, we are able to identify the mobility separated anomers of larger glycans by spectroscopically matching their fragments to anomerically pure, commercially available mono- and disaccharides.

This method allows us to obtain the anomerically pure IR fingerprints of large molecules for which methylated standards are often not obtainable. These fingerprints can in turn be used as standards to assign structures to even larger, more complex oligosaccharides. Ultimately, a sufficiently large

database can be created, allowing for rapid structural identification of large, unknown oligosaccharides.

In the case of glycans cleaved from a protein, there will always be an equilibrium between reducing-end anomers in solution, where the mutarotation reaction that converts them can easily occur. However, these anomers often give rise to multiple peaks in the arrival-time distributions observed using ion mobility, which can complicate the use of IMS for glycan analysis. We demonstrate here that IR spectra of individual, reducing-end anomers can be used to assign the peaks in an ion mobility ATD, allowing one to distinguish them from other isomeric forms.

More broadly, the general approach employed here can be used to identify the other types of CID fragments, which will help in piecing together the primary structure of isomerically complex glycans.

6. Unravelling the structures of sodiated β -cyclodextrin and its fragments

In this chapter, we study the common cyclic oligosaccharide, β -cyclodextrin. We present the cryogenic infrared spectra of its alkali metal-complexes and of its main dissociation products generated by collision-induced dissociation. We characterized the parent molecule by ultra-high resolution ion mobility and cryogenic messenger-tagging infrared spectroscopy. Unlike the fragments presented in the previous chapters, the fragments of β -cyclodextrin all form from breaking two glycosidic linkages. We observe a set of sodium-cationized fragments that differ in mass by 162 u, corresponding to B-type or Z-type fragments, and measure their cryogenic infrared spectra. For the m/z 347 fragment ion, electronic structure calculations indicate that the lowest energy 2-ketone ion structure (B_2 fragment) is consistent with experimental spectra. For the m/z 509 fragment ion, both the 2-ketone B_3 and Z_3 calculated structures are consistent with the experimental data. However, the calculated vibrational spectra of the lowest-energy theoretical structures of the larger m/z 671 ions are not consistent with experiment, indicating either that we are trapping a higher energy conformation or we fail to model one or more specific interactions effectively (i.e., either by sampling or the choice of computational chemistry model).

This chapter is adapted with permission from the article: J. Rabus, R.P. Pellegrinelli, A.H. AbiKhodr, B.J. Bythell, T.R. Rizzo and, E. Carrascosa, "Unravelling the structures of sodiated β -cyclodextrin and its fragments", *Phys. Chem. Chem. Phys.*, 2021,**23**, 13714-13723. It is available online at <https://doi.org/10.1039/D1CP01058A>. All the experimental measurements were made in our laboratory, while the quantum chemical calculations were performed by our collaborators, B. J. Bythell and J. Rabus.

6.1 Introduction

The synthesis and biomedical applications of large cyclic molecular systems have received growing attention, mainly due to their ability to bind selectively to substrates based on non-covalent interactions.¹⁵³ Crown ethers are arguably the most popular and best investigated host molecules for complexing metal ions and are widely used in organic and supramolecular chemistry.¹⁵⁴ Cyclic oligosaccharides occur both naturally and synthetically, and they share similar properties with crown ethers in being able to act as a host for metal cations, organometallic complexes, and biologically relevant molecules.¹⁵⁵ Among the advantages of these compounds is their relative ease of derivatization, allowing for a suitable functional group to be attached to the cyclic oligosaccharide, which can alter their affinity to a certain enantiomer and thus make them good chiral selectors. This is of great interest in separation techniques such as liquid chromatography and capillary electrophoreses.¹⁵⁶⁻¹⁵⁷

The best-known cyclic oligosaccharides are cyclodextrins (CDs), which are produced enzymatically from starch and occur in three different configurations: α , β , and γ , made up of 6, 7, and 8 D-glucopyranose units, respectively, and linked together by α -(1-4) glycosidic bonds.¹⁵⁸ The non-toxicity

and inexpensive synthesis of cyclodextrins has made them the molecules of choice for many applications including drug delivery, cosmetics, and food processing.¹⁵⁹⁻¹⁶² Very recently, a modified β -CD has been shown to have broad spectrum anti-viral properties, including against herpes and Zika.¹⁶³

The properties of cyclodextrins arise from their unique conical cylindrical structure, with the hydroxyls pointing outwards while the glycosidic oxygens and the hydrogens line the interior,¹⁶⁴ leading to a hydrophobic zone inside the cylinder, and a hydrophilic zone on the exterior. This allows CDs to form complexes with a wide variety of compounds, ranging from nonpolar molecules that are captured in the hydrophobic cavity, to polar molecules and ions which preferentially interact with the outer polar surface. Because of this feature, cyclodextrins are water soluble and can be used to bring poorly soluble compounds into aqueous solution by enclosing them in their hydrophobic cavity. For β -CD, the C2 and C3 hydroxyls form a complete hydrogen-bonded network on the wide rim, while the C6 hydroxyls form a separate network on the narrow rim, resulting in a rigid structure (Figure 6.1).¹⁶⁵

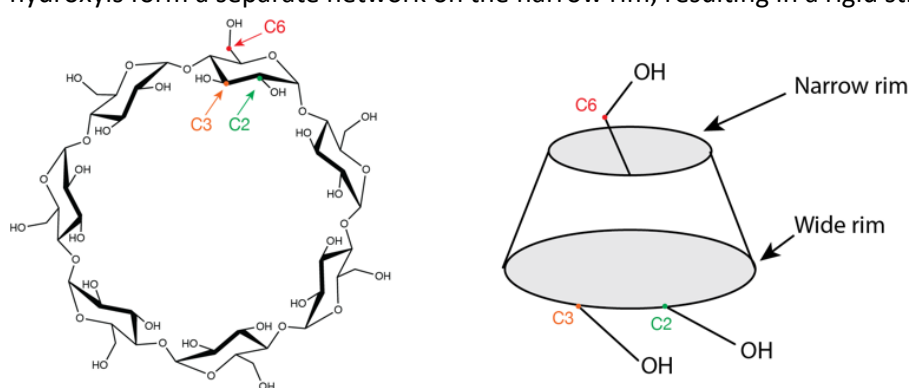


Figure 6.1: Schematic representation of β -cyclodextrin, with its conical structure represented on the right. The carbon atoms connected to the hydroxyls are labelled C2, C3 and C6 for one glucose unit.

Complexation of CDs with guest molecules and ions can distort these structures. It is therefore important to identify these subtle structural details and determine how they affect the physicochemical and biological properties of these species. For this purpose, techniques are needed that can isolate, control and probe molecules. Tandem mass spectrometry (MS^n) coupled with soft-ionization techniques, such as electrospray ionization (ESI) and matrix-assisted laser desorption (MALDI), has emerged as a key tool to investigate large molecules and complexes.¹⁶⁶ Mass spectrometry has thus been used to study many properties of cyclodextrins, including their host-guest interaction with various organic molecules, their binding selectivity with different metal cations, and their fragmentation patterns in the gas phase.¹⁶⁷⁻¹⁷² MS coupled to collision-induced dissociation (CID) is often used in biomedical and pharmaceutical contexts to reconstruct the primary structure and binding characteristics of complexed and functionalized CDs. For instance, fragmentation spectra can help determine the chirality of target analytes present in CD-based host-guest complexes,¹⁷³⁻¹⁷⁴ as well as identify regioisomers of functionalized CDs.¹⁷¹ Furthermore, studies that use CDs to promote or catalyze the synthesis of biodegradable products rely on CID-MS studies to determine the number and structural arrangement of derivative host units attached to the CD guest, and consequently optimize the synthetic strategy.¹⁷⁵⁻¹⁷⁶ The homomolecular nature of cyclodextrins makes them interesting models for CID studies, because they are limited to three types of fragmentation: B/Y, C/Z and cross-ring fragmentation.¹⁰³ Fragmentation of β -CD-metal cation complexes by CID has primarily shown a series of product cations separated by 162 u, which corresponds to a dehydrated glucose unit that

requires fragmentation of two glycosidic linkages.^{103, 177-178} In addition, other cross-ring fragmentation channels have been observed, especially for anions.⁷⁴

In this work, we apply the unique combination of tandem MS with ion mobility spectrometry (IMS) and cryogenic IR spectroscopy to investigate sodiated β -CD and spectroscopically probe its CID products. Understanding which fragmentation pathway(s) is (are) responsible for product ions will provide insight into potential dissociation mechanisms of oligosaccharides which, until now, remain only partially understood.

6.2 Methods

6.2.1 Experimental Details

To explore the fragmentation characteristics and corresponding structural signatures of $[\beta\text{-CD}+\text{Na}]^+$, tandem mass spectrometry, collision-induced dissociation and laser spectroscopy are combined in a homebuilt instrument, schematically depicted in Chapter 2.1, the details of which have been previously reported.¹¹³

β -Cyclodextrin (purchased from Sigma Aldrich and used with no further purification) was dissolved in a water-methanol (1:1) mixture at 0.1 mM concentration, complexed to group I cations, and introduced into the gas phase via nano-electrospray (nESI). In the case of sodiated β -CD cations, these were accelerated through a potential difference of ~ 240 V into the hexapole ion trap at 10^{-2} mbar, creating fragments via CID. The parent ions or fragments were selected by the first quadrupole mass filter and sent to the cryogenic octupole trap. Here messenger tagging spectroscopy was performed at 50-60K using N_2 as a molecular tag. The spectra were normalized to the OPO power, which varies slightly over the range of the scan.

To investigate whether multiple isomers coexist in the gas phase for the studied species, analogous solutions of sodiated β -CD and α -CD were electrosprayed into a recently developed ultrahigh-resolution ion mobility spectrometer attached to a cryogenic trap and a time-of-flight mass spectrometer.⁹² The ion mobility device allows for separation path lengths of over 10 meters and has demonstrated the ability to separate structurally analogous saccharide anomers. Thus, structural differences arising from differing hydrogen bonding arrangements, ring deformations (chair, boat, skew), and sites of sodiation should be well resolved.

6.2.2 Computational approach

To understand the formation mechanism and structure of the observed fragments, theoretical simulations were carried out on the three smallest fragment ions. As previously,^{83, 106, 125, 179} simulations were performed using the genetic algorithm tool Fafoom¹⁸⁰⁻¹⁸¹ to enable effective characterization of the potential energy surface. The structures were optimized using the MMFF94 force field.¹⁸²⁻¹⁸⁶ This approach samples a wide range of ring structures incorporating multiple chair, boat, and skew forms, enabling a thorough interrogation of the potential energy surface. All oxygen sites had sodium cations added using custom scripts to generate starting points for the calculations. Geometry optimizations of the resulting candidate conformations were performed with the Gaussian 09 software package¹⁸⁷ at the HF/3-21G, B3LYP/6-31G(d), and B3LYP/6-31+G(d,p) levels of theory.¹⁸⁸⁻

¹⁹⁰ For the putative charged fragments of the largest species with m/z 671, a combination of a preliminary PM6 optimization with a HF/3-21g single point energy calculation was performed prior to the aforementioned series of calculations. Degenerate structures were removed at each stage, and only the most competitive non-degenerate structures were optimized at each successively realistic level of theory. Additional, targeted manual adjustment and supplementation of the structural pool analysed were performed to reduce the chance that chemically relevant species had been neglected. Subsequent simulations utilizing the CREST package,¹⁹¹⁻¹⁹³ which systemically places a sodium ion at each lone pair of the molecule, with subsequent molecular dynamics using a semiempirical engine followed by B3LYP/6-31G(d) and B3LYP/6-31+G(d,p) calculations broadened the pool of low (and high) energy candidate structures but failed to generate new global minima. All minima were tested by vibrational analysis (all real frequencies). The potential energy surface generated combined the zero-point energy correction (ZPE) to the electronic energy (E_{el} , 0 K) for improved accuracy ($\Delta E_{el+ZPE,0K}$). The related, standard enthalpy (ΔH_{298K}), Gibbs free energy (ΔG_{298K}), and entropy (ΔS_{298K}) corrections to 298 K were also determined. Calculated B3LYP/6-31+(d,p) vibrational frequencies were utilized for comparisons with the experimental spectra. A scaling factor of 0.955 was used for all vibrational frequencies and a 5 cm^{-1} full width at half maximum Lorentzian line shape was employed for comparison to the experimental spectra. Targeted single point calculations at the M06-2X, and ω b97X-D levels of theory were also performed on the selected minimum energy structures to help address variability. Subsequent targeted M06-2X and ω b97X-D optimizations and frequency calculations with 6-31+G(d,p) basis sets on m/z 671 candidates were consistent with the B3LYP data.

6.3 Results and Discussion

6.3.1 CID mass spectrum

Figure 6.2 presents mass spectra of sodiated β -CD under largely non-dissociative conditions (a) and CID conditions (b). The spectrum in Figure 6.2(b) exhibits the $[\beta\text{-CD}+\text{Na}]^+$ precursor ion mass at m/z 1157, as well as a sequence of lower mass peaks at m/z 995, 833, 671, 509 and 347.

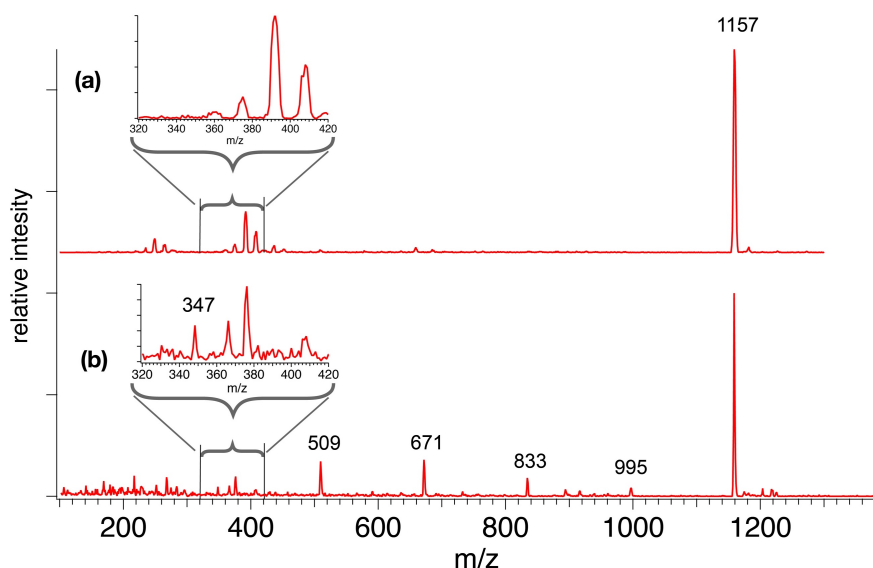


Figure 6.2: CID-MS of sodiated β -CD and its fragments, carried out with a potential difference of 100 V (a) and 240 V (b) in our tandem mass spectrometer. Consecutive loss of 162 m/z is observed from the parent at 240 V, while no fragments are observed at 100V.

This series indicates spacings of 162 u, a fragment moiety that has been previously observed^{171, 177} and corresponds to a singly charged, dehydrated glucose monosaccharide. Detection and analysis of the monomeric dehydrated glucose fragment at m/z 185 was not attempted, mainly due to the increased number of overlapping ions in the low mass range. A minor peak at m/z 893 corresponds to the loss of 264 mass units and is ascribed to a minor cross-ring fragmentation process also observed in previous investigations.^{74, 177} The masses corresponding to the three- and four-glucose unit fragments (m/z 509 and m/z 671) appear as the most intense CID products, whereas formation of two- and six-residue fragments appear with much lower intensity.

It is difficult to determine whether the fragmentation occurs in a sequential or simultaneous manner. However, similar peaks and relative intensities are produced in a commercial time-of-flight (ToF) spectrometer (Waters Q-ToF Premier, Figure 6.3(a)) and our home-built instrument. To further investigate this, a series of CID experiments at increasing collision energies were performed on the Q-ToF, and all the main fragments appeared at the same energy threshold, providing no evidence for a sequential process (see Figure 6.3(b)).

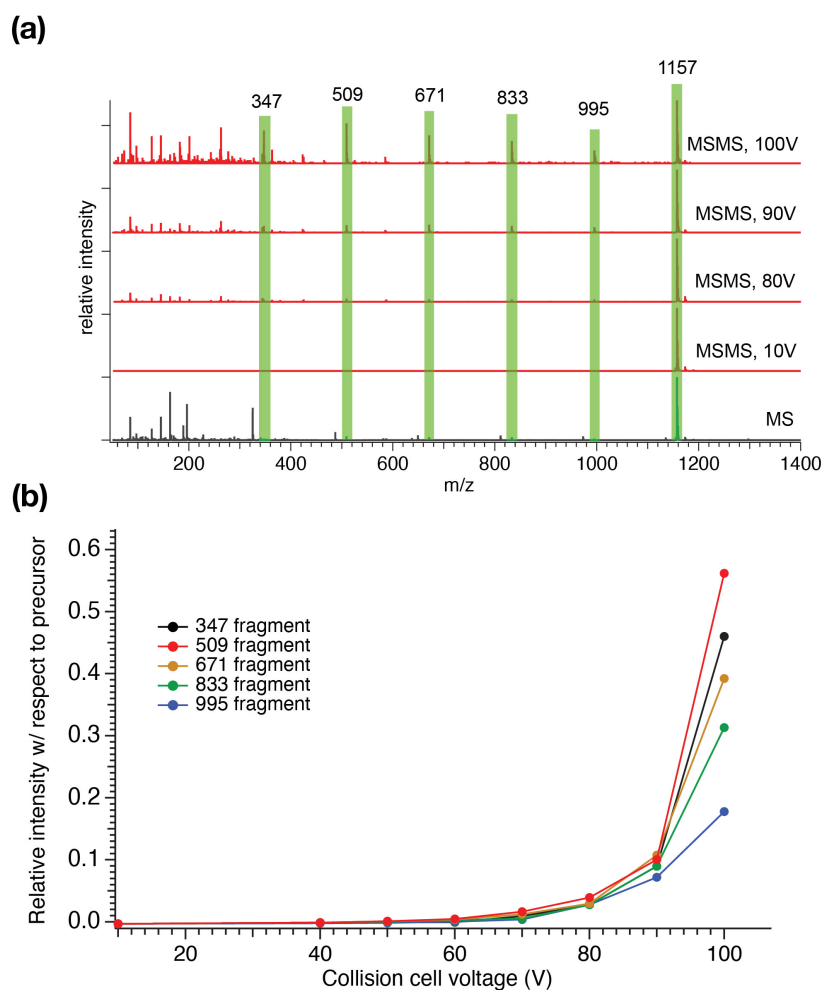


Figure 6.3: (a) MS and MS² spectra of sodiated β -CD at different fragmentation energies in the collision cell of a commercial QToF spectrometer (Waters Permier). The MS spectrum shows the presence of protonated fragments either already present in solution or produced *in-source*. Formation of the main sodiated fragments starts at voltage difference of around 80V between the quadrupole bias and the collision cell bias. The main fragment masses are marked by green shaded areas. (b) Relative intensity of CID fragments of sodiated β -CD normalized to the precursor intensity as a function of collision cell energies on a commercial QToF spectrometer (Waters Permier).

6.3.2 Ion mobility and cryogenic IR action spectra of sodiated α -CD and β -CD

Precursor $[\beta\text{-CD}+\text{Na}]^+$ ions can adopt different conformations depending on the relative orientation of the OH groups at both the narrow and wide rims of the conical cylindrical structure (Figure 6.1). The relative orientation of these donor-acceptor hydrogen bonding networks at both edges of the molecule can potentially lead to four different combinations, depending whether the hydrogen bonding pattern is clockwise (cw) or counter-clockwise (cc): cc-cc, cc-cw, cw-cc and cw-cw.¹⁹⁴ Distortion of these symmetric conformations through inclusion of Na^+ might significantly increase the number of conformers. To evaluate whether electrosprayed $[\beta\text{-CD}+\text{Na}]^+$ ions form a distribution of conformers, additional experiments were carried out using a recently designed instrument that combines ultrahigh-resolution travelling-wave ion mobility spectrometry (IMS) using structures for lossless ion manipulation (SLIM),^{141, 195} with cryogenic infrared spectroscopy to provide isomer-specific structural identification of complex molecules.⁹² In this work, sodiated β -CD was cycled through the

IMS section of this apparatus over a total length of ~ 17 meters, which has been shown to be sufficient to separate small structural differences.¹⁴² However as shown in Figure 6.4(b), only one primary, well-resolved peak was observed in the arrival time distribution (ATD) under these conditions. A similar experiment on the six-member cyclic structure $[\alpha\text{-CD}+\text{Na}]^+$ also reveals a single peak in the ATD (Figure 6.4 (a)). These results can be potentially interpreted in three ways: (1) the monomodal ATDs demonstrate the presence of a single, stable gas-phase conformer for both sodiated α - and β -CD; (2) both cyclodextrins consist of multiple stable conformers (with different relative orientations of the hydrogen bonding networks, or different coordination number between the Na^+ and CD, for example) that are so structurally similar that they cannot be separated using our SLIM-IMS device; or (3) the monomodal ATD results from multiple conformers that rapidly interconvert.

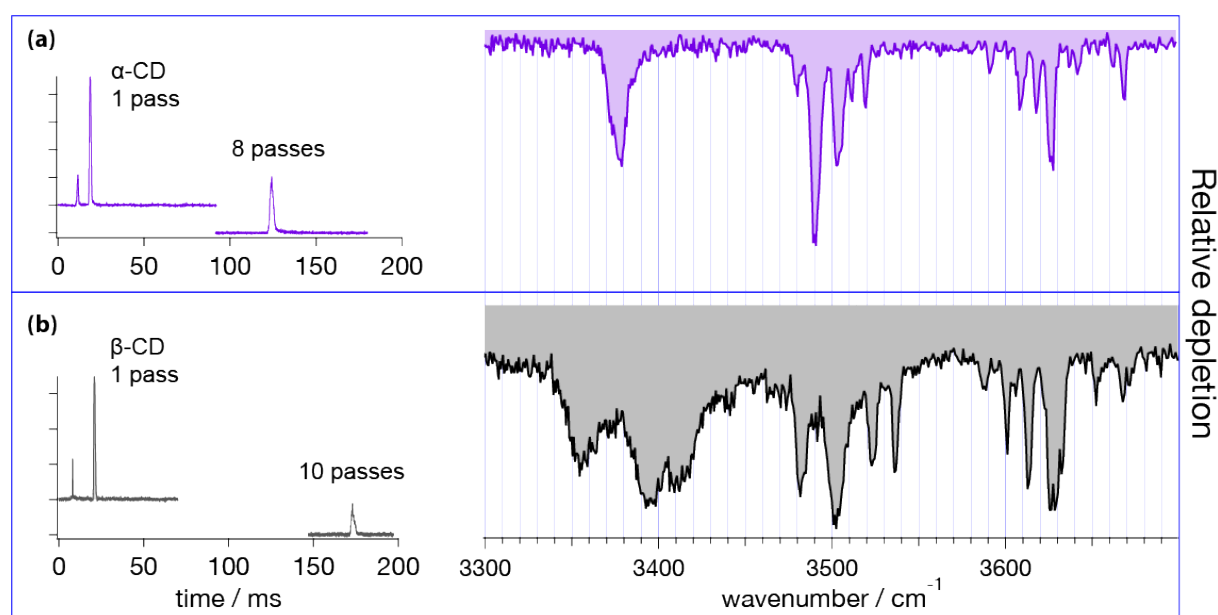


Figure 6.4: Arrival times of $[\alpha\text{-CD}+\text{Na}]^+$ (a) and $[\beta\text{-CD}+\text{Na}]^+$ (b) and their corresponding cryogenic IR spectra. Note that the fast ATD peak in the left panels of (a) and (b) corresponds to doubly charged dimers of the corresponding cyclodextrins that cannot be discriminated by our quadrupole mass filter and are propelled faster through the IMS buffer gas due to their doubly charged character.

Option (3) appears highly unlikely, given the rigid geometry of both sodiated β -CD and α -CD and the consequent significant strain associated with the concerted rearrangement of the hydrogen-bonded hydroxyl groups. We cannot completely rule out the possibility of (2), that structurally similar $[\alpha\text{-CD}+\text{Na}]^+$ or $[\beta\text{-CD}+\text{Na}]^+$ conformers are present within the same ATD peak. Structural changes resulting from different coordination numbers of the sodium cation will likely lead to structural distortions easily resolved by our ion mobility device. Even if two or more cyclodextrin conformers would have such similar CCS that our SLIM-IMS is unable to resolve them, corresponding calculations would also not be able to reproduce the slight difference in CCS, as the resolution of our IMS instrument exceeds the accuracy of such calculations. As discussed more fully below, cryogenic IR spectroscopy is highly sensitive to structural differences, and the number of bands in each of the spectra of Figure 6.4 is consistent with presence of single conformers. Thus, the most straightforward conclusion from the data of Figure 6.4 is that both sodiated α - and β -CD exist as single conformers in the gas phase.

The cryogenic IR spectra corresponding to the monomodal ATD distributions of sodiated α - and β -CD

shown in Figure 6.4 were obtained by gating the monomer ATD peak, storing and tagging the corresponding ions in a cryogenic ion trap, and monitoring the depletion of tagged species as a function of IR wavenumber using a ToF spectrometer. Both IR spectra show similarities, with three distinct regions of IR transitions representing three types of OH oscillators. The lowest energy range of the spectra (3330-3450 cm^{-1}) exhibits broad bands for both $[\alpha\text{-CD+Na}]^+$ and $[\beta\text{-CD+Na}]^+$. The $[\alpha\text{-CD+Na}]^+$ spectrum presents a slightly asymmetric feature at 3375 cm^{-1} , while the spectrum of $[\beta\text{-CD+Na}]^+$ shows three distinct bands with maxima at 3355, 3395 and 3410 cm^{-1} . Previous theoretical studies on neutral and metal-complexed CDs predict a tight hydrogen bonded network between the C6 hydroxyls on the narrow rim, and find that Na^+ and other metal cations preferentially coordinate with these hydroxyls.¹⁹⁶⁻¹⁹⁹

Additional cryogenic IR spectra of $\beta\text{-CD}$ complexed to other group I metal cations (Figure 6.5) demonstrate that the ionic radius strongly affects the bands below 3450 cm^{-1} . The IR spectra in this wavenumber region show three major bands for all complexed $\beta\text{-CD}$ cations, whereas only the complexes with Cs^+ and Rb^+ show significant spectral similarity. These experimental findings support the notion that the C6 hydroxyls are binding sites for the metal cations, but also hint to the formation of additional hydrogen bonding networks between these C6 OHs, which vary in number and strength depending on the complexed metal cation. For instance, the small Li^+ will be complexed by a reduced amount of C6 O-atoms, thus likely promoting one or more strong hydrogen bonds between the hydroxyls undergoing metal complexation and other neighbouring free C6 OHs. Such a strong hydrogen bond could be the reason for the broad low energy band centred at 3225 cm^{-1} , which is only present in the IR spectrum of $[\beta\text{-CD-Li}]^+$. Furthermore, the spectrum of $[\beta\text{-CD-Li}]^+$ shows two unique transitions at 3553 cm^{-1} and 3572 cm^{-1} which are not present in any of the other metal-complexed spectra. Since these bands occur only for the Li^+ cation, it is possible that they correspond to two of the C6 hydroxyl groups which escaped the strong hydrogen bonding network localized around the Li^+ . In contrast to the lithium case, the large radii Cs^+ and Rb^+ cations will be complexed by many of the seven C6 hydroxyl groups of $\beta\text{-CD}$, preventing the strong hydrogen bonds predicted for the Li^+ complex. These symmetry considerations agree with the theoretical predictions of Gamez and coworkers, which find a trivalent coordination of the C6 hydroxyls for the $[\alpha\text{-CD-Li}]^+$ complex, whereas the lowest energy $[\alpha\text{-CD-Cs}]^+$ complex consists of five C6 Oxygens binding to the metal cation.¹⁹⁹ Based on these arguments, an even stronger symmetric complexation could be inferred from the $[\alpha\text{-CD-Na}]^+$ spectrum (Figure 6.4(a)), where the presence of one single transition centred at 3370 cm^{-1} plausibly arises from a structural arrangement with the C6 hydroxyls binding to the metal cation, leading to a network of concerted hydrogen bonds. In contrast, the low energy spectral region in sodiated $\beta\text{-CD}$ hints to a more asymmetric binding pattern to the metal cation

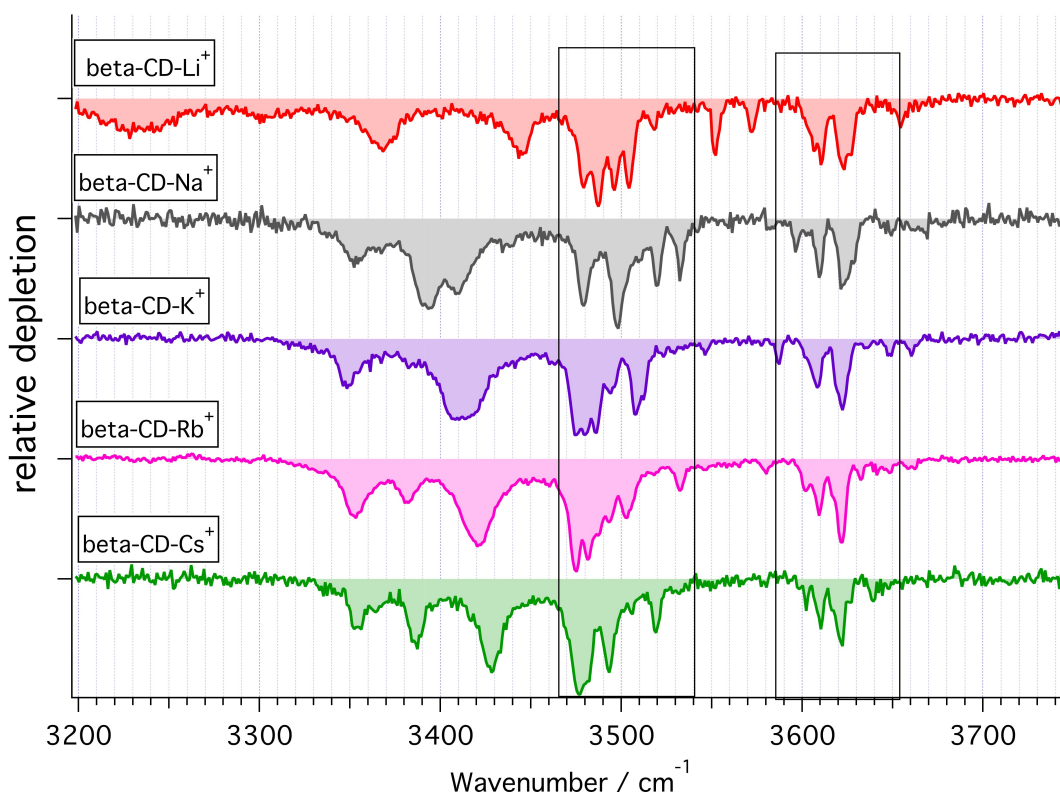


Figure 6.5: Cryogenic IR spectra of β -CD complexed with group I cations. The two marked areas denote the transitions associated to the C2 and C3 OH oscillators.

The differences between sodiated α - and β -CD in this spectral region can be thus attributed to different sodium binding patterns and consequent symmetry distortions of the two molecules. In summary, we assign these low energy transitions to the C6 hydroxyl stretch vibrations and associate the differences in this region to the number of metal-binding C6 hydroxyls as well as the resulting strength of additional intramolecular hydrogen bonds between these OHs.

The higher energy part of the spectra shows two groups of narrow transitions in the 3450-3550 cm^{-1} and 3560-3700 cm^{-1} ranges. Based on the above assignment, these oscillators correspond to the C2 and C3 hydroxyls located on the wider rim. Theoretical studies have repeatedly shown that these hydroxyls form a hydrogen-bonded network that can adopt two different configurations around the rim (cw and ccw), either with the C3 hydroxyls hydrogen-bonded to the partially free C2 hydroxyls of the adjacent glucose moieties, or the reversed configuration. While these two possible configurations prevent us from assigning the groups of IR transitions to specific hydroxyls, the 3450-3550 cm^{-1} and 3560-3700 cm^{-1} transitions correspond to the hydrogen-bonded and partially free hydroxyls on the wide rim, respectively. The similarity between sodiated α - and β -CD in these spectral regions further supports that the metal cation does not bind here, but rather at the narrow rim.

6.3.3 Cryogenic IR spectra of CID fragments

Sodiated fragments of $[\beta\text{-CD}+\text{Na}]^+$ were produced by collision-induced dissociation between the ion funnel and the hexapole followed by m/z selection in the first quadrupole and storage in the cryogenic trap, where their IR spectra were recorded (Figure 6.6(a-f)). These spectra provide well-resolved

transitions that can be used to help determine the structure(s) of the fragment ions. Note that the IR spectrum of the precursor sodiated β -CD (Figure 6.6(f)) obtained on the mass spectrometer discussed in Chapter 3.1 is highly consistent with the $[\beta\text{-CD+Na}]^+$ spectrum (Figure 6.4(b)) obtained using the IMS-MS device. This spectral comparison demonstrates that the conformational landscape of sodiated β -CD is similar in both instruments. Following all above arguments, we expect that the CID fragments of Figure 6.2(b) are produced from a single $[\beta\text{-CD+Na}]^+$ conformer.

To associate the observed spectroscopic features with a specific structure, compositional sampling simulations followed by electronic structure and vibrational frequency calculations were performed on the sodiated fragments containing 2, 3, and 4 residues (m/z 347, 509, and 671, respectively).

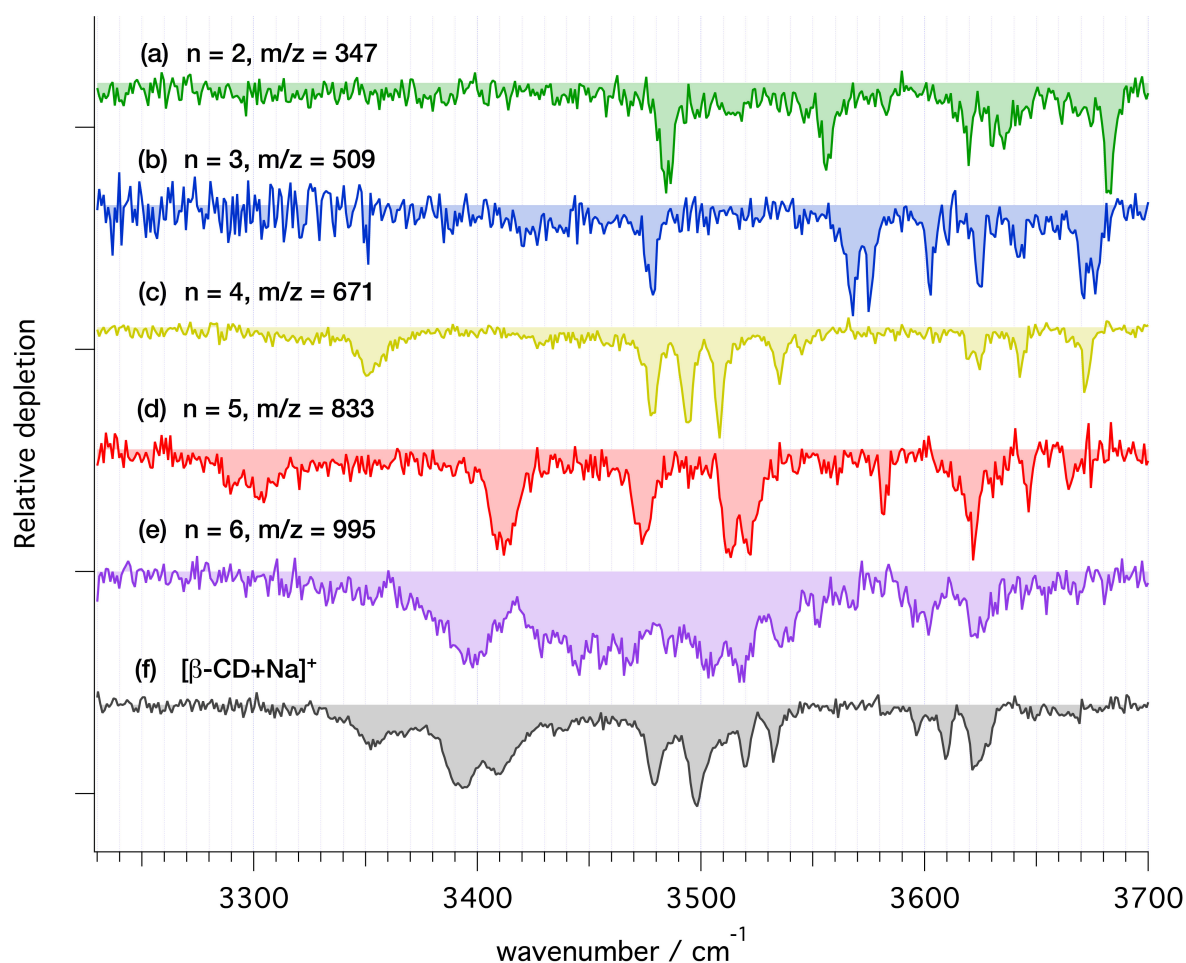


Figure 6.6: Cryogenic IR spectra of the main CID fragments of $[\beta\text{-CD+Na}]^+$ (a-e) and the parent ion (f). The index n refers to the number of monosaccharides in each fragment.

The spectra of the 2- and 3-residue sodiated fragments (Figure 6.6(a, b)) exhibit a series of well-resolved bands above 3530 cm^{-1} as well as one band in the $3480\text{-}3490\text{ cm}^{-1}$ range. Neither spectrum show bands below 3470 cm^{-1} . In both cases, the observed number of transitions match the expected number of OH stretch vibrations if one assumes that there is only a single conformer. The most distinct IR signatures are observed for the 4-residue fragment (Figure 6.6(c)). The three clumps of well-resolved bands resemble the spectral features observed for $[\alpha\text{-CD-Na}]^+$ (see Figure 6.4(a)). Synthesis

of similar cyclic tetrasaccharides has been previously carried out,²⁰⁰⁻²⁰¹ and very recently the first synthesis of a 4-member cyclodextrin was reported.²⁰² However, both the significant strain imposed on the glucose units²⁰³ together with the predicted high barrier to re-cyclization make the formation of a 4-member cyclodextrin unlikely. Despite this, we tested this hypothesis computationally, as discussed below.

In contrast to the spectra of the smaller fragments, the 5- and 6-residue ions (Figure 6.6(d-e)) exhibit a significant number of broad bands at lower wavenumber, which are characteristic of hydrogen-bonded OH stretch vibrations. The spectrum of the 5-residue fragment contains a few weak bands in the 3280-3320 cm^{-1} range, four strong broad features in the 3400-3550 cm^{-1} range, as well as several weaker transitions at higher wavenumber. There are fewer bands for this fragment than the number of OH oscillators, indicating that some bands overlap. The 6-residue fragment (Figure 6(e)) exhibits a less resolved IR spectrum, with overlapping bands across the entire range between 3360-3630 cm^{-1} . Comparing the $n=6$ fragment to the isomeric $[\alpha\text{-CD+Na}]^+$ (Figure 6.4(a)) reveals a difference in the number, position, and breadth of the bands, which may reflect the difference between a more symmetric, rigid, cyclic structure and an open, asymmetric one. The spectroscopic differences between the $n=6$ fragment and $[\alpha\text{-CD+Na}]^+$ thus imply the presence of a substantial energy barrier to re-cyclization of the CID fragment. Rather, one (or several) open fragment structure(s) must be stabilized and kinetically trapped in its (their) potential minimum (minima) through collisional cooling.

6.3.4 Comparison with Theory

Simulations of the 2-, 3-, and 4-residue fragments resulted in a significant number of low energy conformations. For the 2- and 3-residue fragments, simulations predict four distinct types of energetically stable structures (Figure 6.7), with an additional cyclic form found for the 4-residue dissociation product.

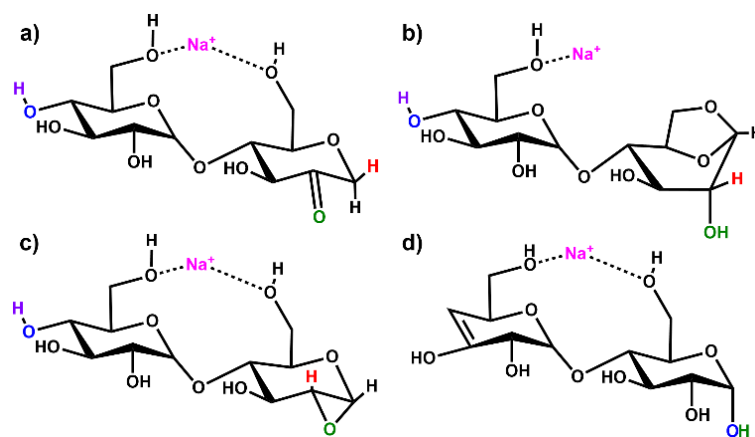


Figure 6.7: Putative ion structure types potentially formed from $[\beta\text{-CD+Na}]^+$, illustrated for the 2-residue, m/z 347 species: (a) 2-ketone B_2 ; (b) 1,6-anhydro B_2 ; (c) 1,2-anhydro B_2 ; and (d) Z_2 ion.

Three of the four fragments are B ions, while the remaining fragment species is a product of a Z-type fragmentation. Our B3LYP data support 2-ketone B-type fragments^{106, 179, 204-205} as the lowest energy structures. The mechanistically less likely to be formed 1,6-anhydro B ion structure¹²⁴⁻¹²⁵ is next followed by the epoxide 1,2-andydro structures, which are consistently least energetically favourable

($\geq 85 \text{ kJ mol}^{-1}$). The Z fragments are predicted to be 10-20 kJ mol^{-1} higher in energy than the 2-ketone B ion structures. Large basis set M06-2X and ω b97X-D single-point calculations predict the 2-ketone and 1,6-anhydro terminated B ion structures and the Z ion structures to be of similar relative energy. All levels of theory substantially disfavour the strained 1,2-anhydro terminated B ion structures. The lowest energy structures of each type of fragment are shown in following Figures, and the corresponding relative energies are indicated in Tables A1-A3 of the appendix.

For the 2-residue fragment (m/z 347), Figure 6.8 depicts the comparison between the experimental spectrum and the IR transitions calculated for the lowest energy B_2 and Z_2 ion structures. This result strongly suggests formation of a 2-ketone B_2 ion structure (Figure 6.7a). Consequently, we assign: (1) the $\sim 3485 \text{ cm}^{-1}$ band to the symmetric O-H stretch of the carbon 3 hydroxyl of residue 2, H-bonded to the adjacent ketone oxygen and the O-H of the carbon 2 hydroxyl of residue 1 (also H-bonded); (2) the 3556 cm^{-1} band to the asymmetric stretch of the same hydroxyl groups; (3) the 3620 cm^{-1} band to the carbon 4 hydroxyl of residue 1, O-H stretch; (4) the 3630 cm^{-1} band to the carbon 3 hydroxyl of residue 1, O-H stretch; (5) the 3636 cm^{-1} band to the carbon 6 primary hydroxyl of residue 2, O-H stretch; and (6) the 3683 cm^{-1} band to the carbon 6 primary hydroxyl of residue 1, free O-H stretch. Following these assignments, and in contrast to the cyclic structures proposed for the metal complexes (Figure 6.5), the low energy bands observed for the sodiated ring-opened β -CD fragments do not necessarily relate to the C6 hydroxyls.

The proposed mechanism for this fragmentation process is presented in Figure 6.9 and is adapted from earlier proposals for linear systems.^{106, 179, 204-205} Other candidate fragmentation pathways are detailed in Figure A1 of the appendix. The mechanism involves abstraction of a carbon 2 hydroxyl proton, formation of a ketone, and a 1,2-hydride shift with concerted glycosidic bond cleavage.^{106, 179, 204-205} This ring opening simultaneously creates the first 2-ketone and a new C4 hydroxyl group from the cleaved glycosidic linkage. i.e., nominally a linear B_7 2-ketone terminated structure. Further dissociation of a second glycosidic bond in an identical manner results in generation of 2-residue and 5-residue structures with the sodium cation in an ion-molecule complex.¹²⁴ Provided the complex has sufficient lifetime, a competition for the sodium cation ensues in which the fragment with the larger sodium affinity should most frequently predominate.¹²⁴⁻¹²⁵ If the 2-residue fragment separates with the sodium attached, an m/z 347 ion is detected, and if the 5-residue fragment separates with the sodium attached, an m/z 833 ion is detected.

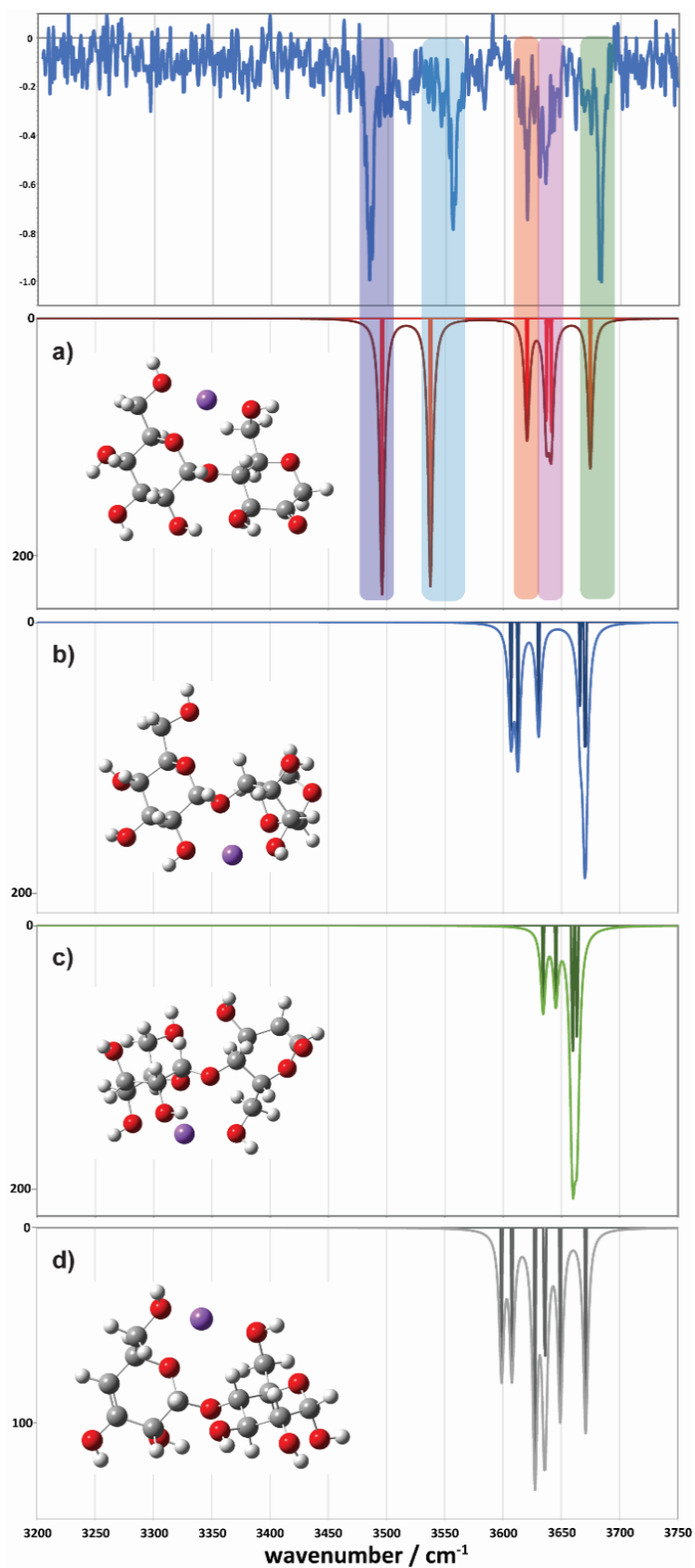


Figure 6.8: Comparison between the experimental (top) and simulated IR spectra for the m/z 347 fragment. (a) represents the ketone, (b) the 1-6 anhydro, (c) the 1-2 anhydro and (d) the Z fragment structures.

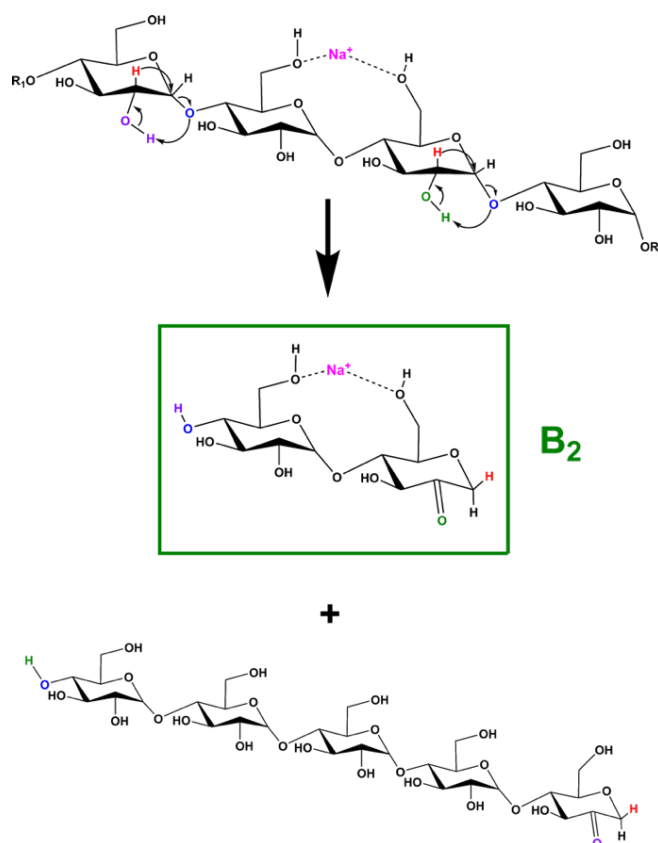


Figure 6.9: Proposed fragmentation mechanism for the formation of the m/z 347 fragment

Comparison between experimental and theoretical IR spectra of the 3-residue fragment is less conclusive (Figure 6.10). None of the theoretical spectra of the lowest energy structures are perfectly consistent with experiment. The lowest energy 2-ketone B_3 -type structure is reasonably consistent with experiment (Figure 6.10a, mean deviation = 5.9 cm^{-1} , $R^2 = 0.97$). However, the Z_3 -type structure shows a similar quality of fit (Figure 6.10d, mean deviation = 12.0 cm^{-1} , $R^2 = 0.94$). In contrast, the 1,2-anhydro B_3 prediction lacks sufficient intermediate energy bands and there is no evidence to support any population of the 1,6-anhydro B_3 structure. The latter is consistent with structural arguments against the feasibility of the cross-ring proton transfers necessary to generate these structures from alpha linked sugars as illustrated in Figure A1c of the appendix.

If our tentative assignment of the 2-ketone B_3 or the Z_3 ion structure for the m/z 509 peak is correct, this offers a potential explanation for the origin of the m/z 671 spectrum —that is, analogous 3-residue and 4-residue structures together with a sodium cation comprise the ion-molecule complex formed following dissociation of the 2 glycosidic bonds. As both neutrals are of similar size and comprise the same functional groups, similar sodium affinities should be expected, enabling both ions to be formed and detected, provided the ion-molecule complex has sufficient lifetime to enable sodium cation transfer between the fragments.¹²⁴

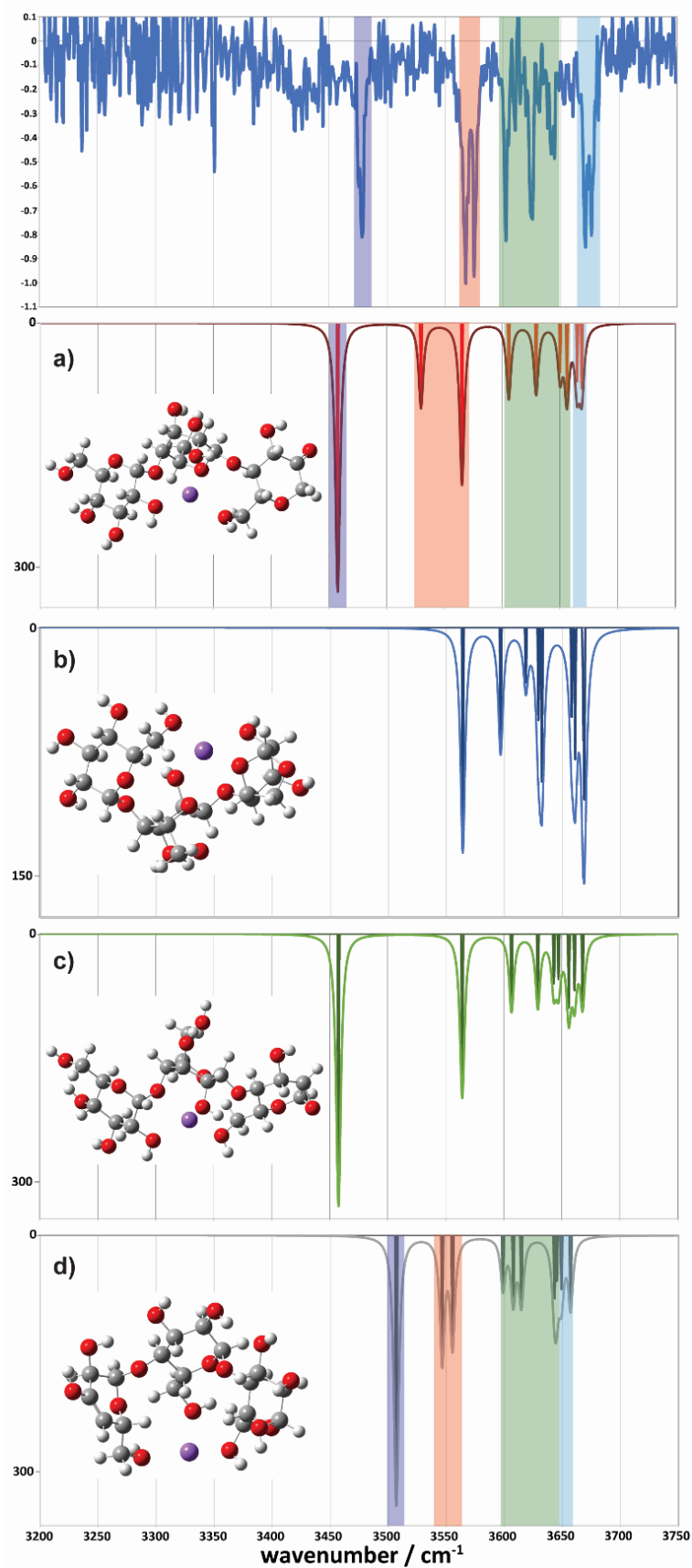


Figure 6.10: Comparison between the experimental (top) and simulated IR spectra for the m/z 509 fragment. (a) represents the ketone, (b) the 1-6 anhydro, (c) the 1-2 anhydro B_3 and (d) the Z_3 fragment structures.

Following this argument, either a 2-ketone B₄ or a Z₄ structure would be expected for the 4-residue fragment, but none of the lowest energy 2-ketone B₄ nor Z₄ theoretical spectra are particularly consistent with the experimental spectrum for *m/z* 671 (Figure A2 of the appendix). This is similarly true for the other fragment structure types including potential cyclic candidate structures.

However, we did locate a low energy 2-ketone B₄ structure that was far more consistent with the experimental spectrum (Figure 6.11). The broad bands at low wavenumber correspond to strongly H-bonded C6-OH stretches (predicted at 3290 and 3377 cm⁻¹), consistent with the broad feature at ~3310-3380 cm⁻¹. The bands at intermediate wavenumber correspond to a mixture of H-bonded environments (C3-OH, C6-OH, C2-OH, C2-OH, C2-OH) at 3473, 3502, 3520, 3546, and 3566 cm⁻¹, respectively. The bands at high wavenumber (3602, 3616, 3626, and 3662 cm⁻¹) comprise three C3-OH stretches and a free C6-OH stretch.

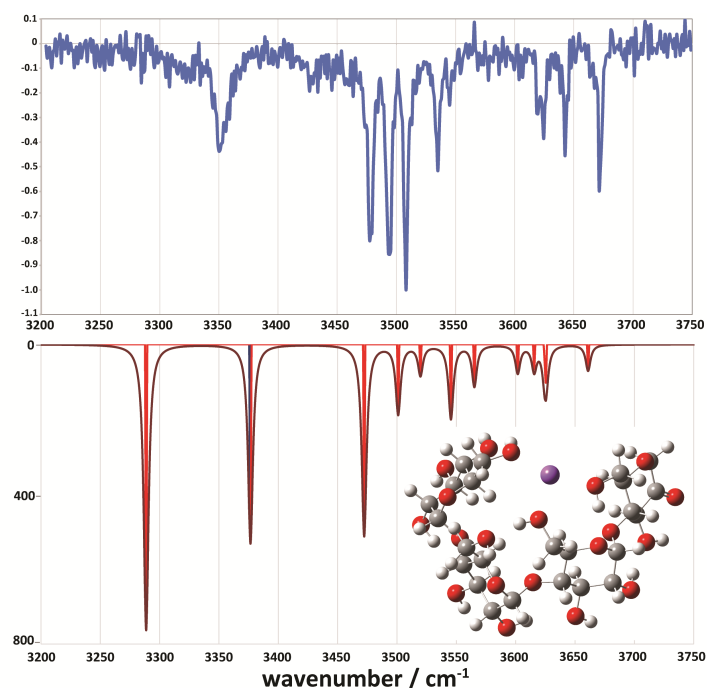


Figure 6.11: Comparison between the experimental (top) and simulated IR spectra for the *m/z* 671 fragment. The simulated spectrum represents a 2-ketone B₄ structure at 7.9 kJ/mol.

6.4 Conclusions

This work reports fingerprint vibrational spectra for a series of metal complexed β-CD cations, focusing on sodiated β-CD and its CID products. We obtain distinct, well-resolved infrared spectra for each of the main fragments. Simulations followed by electronic structure and vibrational frequency calculations were performed for the 2-, 3-, and 4-residue ions corresponding to B or Z ion structures and compared to the experimental results. The main findings of this work are:

- (1) Collisional activation of [β-CD+Na]⁺ results in a series of fragment ions differing by 162 u. Cryogenic IR spectroscopy experiments on the major fragment ions provide well-resolved vibrational fingerprints in the 3200-3750 cm⁻¹ spectral region.

(2) Our combined experiments and calculations support the formation of a single gas-phase conformer in each of the m/z 347, 509, and 671 species. The experimental spectrum for $n=5$ suggests formation of a single fragment conformer, while that for the 6-residue fragment suggests the presence of more than one stable conformer.

(3) There are four main types of potential fragmentation products for the 2-, 3-, and 4-residue fragments. For the 2-residue fragment, the predicted lowest energy 2-ketone-type fragment is clearly the most similar to the experimental spectrum. For the 3-residue fragment, both the predicted lowest energy 2-ketone-type and Z_3 -type fragments show significant similarities to the experimental spectrum. The 4-residue fragment is also most consistent with a 2-ketone type structure, which in turn would support the same for the 3-residue fragment (Figure 6.9). Thus, all the fragments seem to form 2-ketone structures.

(4) The results presented here also demonstrate that cryogenic IR spectroscopy and theory can be used to directly relate spectroscopic patterns in CD-metal cationic complexes to the location and degree of coordination between the host CD and the metal ion.

In a broader context, this work demonstrates the potential of our method to unravel atomic-level structural features of complex biomolecular systems that can help address key macromolecular functions.

7. Conclusions

In this thesis, we presented cryogenic IR spectra of glycans, and their fragmentation products generated by CID. We used ultra-high resolution IMS to separate reducing-end glycan anomers, allowing us to obtain the IR spectra of the separated anomers and their CID fragments. The addition of a new ultra-high resolution IMS stage to a homebuilt tandem mass spectrometer, and its characterization was described in detail in Chapter 2. After discussing the underlying mechanisms behind ion activation and unimolecular dissociation leading to CID of glycans in Chapter 3, the cryogenic IR spectra of C-type and IMS-selected Y-type glycan fragments, were presented in the subsequent chapters. These provide complementary information for the development of a spectroscopic glycan database that will ultimately be able to unambiguously identify the exact structure of any glycan. The cyclic oligosaccharide β -cyclodextrin was studied in the final chapter using IR spectroscopy, ultra-high resolution IMS, and CID. The structural arrangement of the hydroxyls on the molecule as well as the binding sites for metal cations were predicted from the measured IR spectra. Spectra of the CID fragments were compared to electronic structure calculations, giving insight into the potential structures of the B-type and Z-type fragments produced.

Our study of glycan C-type fragments, presented in Chapter 4, significantly extends initial studies performed by the Compagnon group which shows that lithiated and protonated C_1 fragments retain the anomericity of the glycosidic bond at their reducing end for sugars up to pentasaccharides. We show this to be the case for C_1 and C_2 fragments, generated from both linear and branched parent oligosaccharides, comprising of up to six sugar units. Our cryogenic IR spectroscopy provides sufficient resolution to clearly distinguish the anomers of glycans containing several sugar units, allowing us to easily determine that the C fragments consist of a single anomer, corresponding to that of the anomericity glycosidic bond from which it was generated. This discovery provides a powerful new tool for glycomics. It allows for a clear determination of the anomericity of glycosidic bonds within a glycan, which has been challenging up to this point.

The development of ultra-high resolution IMS has greatly benefitted the field of glycan analysis, allowing for rapid separation of isomers of very similar structures. The identification of the structures separated by IMS is not always trivial, as every reducing sugar possesses two anomers at the reducing end, which interconvert freely in solution, but lock into either the α or β configuration when transferred into the gas phase. These reducing-end anomers can be separated by ultra-high resolution IMS, resulting in extra mobility peaks being observed when studying glycans. In Chapter 5, we use the IR spectra of Y fragments, generated from parent glycans separated by ultra-high resolution IMS, to assign the peaks separated by ion mobility to the reducing α and β anomers. This is important from an analytical perspective. When analyzing a mixture of isomeric glycans by IMS, it is important to know which mobility separated species come from different glycosidic linkages and which ones come from the anomers at the reducing end. Our approach allows us to take a spectral fingerprint of the α and β reducing anomers of glycans, allowing them to be distinguished from other structures.

The work presented in chapters 4 and 5 play a fundamental role in the development of a spectroscopic glycan database, which would be ultimately be able to unambiguously identify any glycan's exact

structure, down to the anomericity of every glycosidic bond and the reducing end hydroxyl. The determination of glycosidic bonds in larger, more complex structures than those presented in this thesis can be achieved using C fragments, while the database of anomerically pure glycan spectra can be expanded using ultra-high resolution IMS followed by Y-fragmentation. Current work, expanding on the research presented here, is aimed at determining the exact structures of large glycans such as Man-8, which until now is not fully understood. This will result in significant advances in the field of glycomics, ultimately leading to a better understanding of glycosylation and opening the door to new types of glycan-based therapeutics.

After having studied the C and Y fragments for linear and branched oligosaccharides, we investigated the cyclic molecule, β -cyclodextrin (CD). Although this molecule is better known for its industrial uses, it is an oligosaccharide and an understanding of its fragmentation could be beneficial in understanding the fragmentation of other glycans. Chapter 6, provides insight into β -CD's hydrogen-bonding network and metal-complexation sites as well as possible fragmentation mechanisms. The groups of vibrational bands observed in the molecule's IR spectrum could be related to the different hydroxyl groups present on β -CD, by measuring the spectra of the different complexes between β -CD and alkali metal cations. The IR spectra of the main fragmentation products of β -CD were measured and the three smallest fragments compared to electronic structure calculations, performed by our collaborators B. J. Bythell and J. Rabus. Correspondence between the experimental and calculated data indicate that the 2-membered fragment corresponds to a B_2 ion with a 2-ketone structure, while the 3-membered fragment spectrum shows correspondences with both the 2-ketone B_3 and Z_3 calculated structures. Although none of the calculated lowest-energy structures correspond to the spectrum of the 4-membered fragment, a low energy structure corresponding to the 2-ketone B_4 was found which is consistent with the experimental data. This supports the hypothesis that all the fragments formed are of 2-ketone structures. These findings give insights into the structures of CID fragments of glycans, as well as provide evidence supporting proposed fragmentation mechanisms of sodium-complexed sugars. This, combined with future works, can be used to gain a better understanding of the fragmentation pathways of metal-complexed oligosaccharides.

As already stated, future work should focus on expanding the spectroscopic database of glycans, using a combination of IMS, C fragments and Y fragments to assign an IR spectrum to every glycan structure observed in the gas phase. Priority should be placed on fragments that are common to certain classes of glycans. For example this work characterized N,N'-diacetylchitobiose, which is a core structure for N-glycans, and N-acetyllactosamine and lactose for human milk oligosaccharides. Larger characteristic sequences could be identified and included to the database, reducing the number of steps required to identify some large, unknown oligosaccharide. Furthermore, spectroscopic studies of B fragments could allow for extra leverage on determining glycans primary structure. As seen in chapter 6, several structures were proposed for the B fragments, the 2-ketone structure appearing to best match our experimental spectra. Nevertheless, it would be worthwhile to investigate if the preferred structure of the B fragment is dependent on the anomericity and/or the connectivity of the glycosidic bond, as seems to be indicated by recent works.⁷¹⁻⁷² This would allow for B, C and Y fragments to be used in complementary fashion, leading to an even better characterization of glycan structure.

Appendix: Fragmentation mechanisms, calculated spectra, and relative energies of the candidate fragment ion structures of β -cyclodextrin

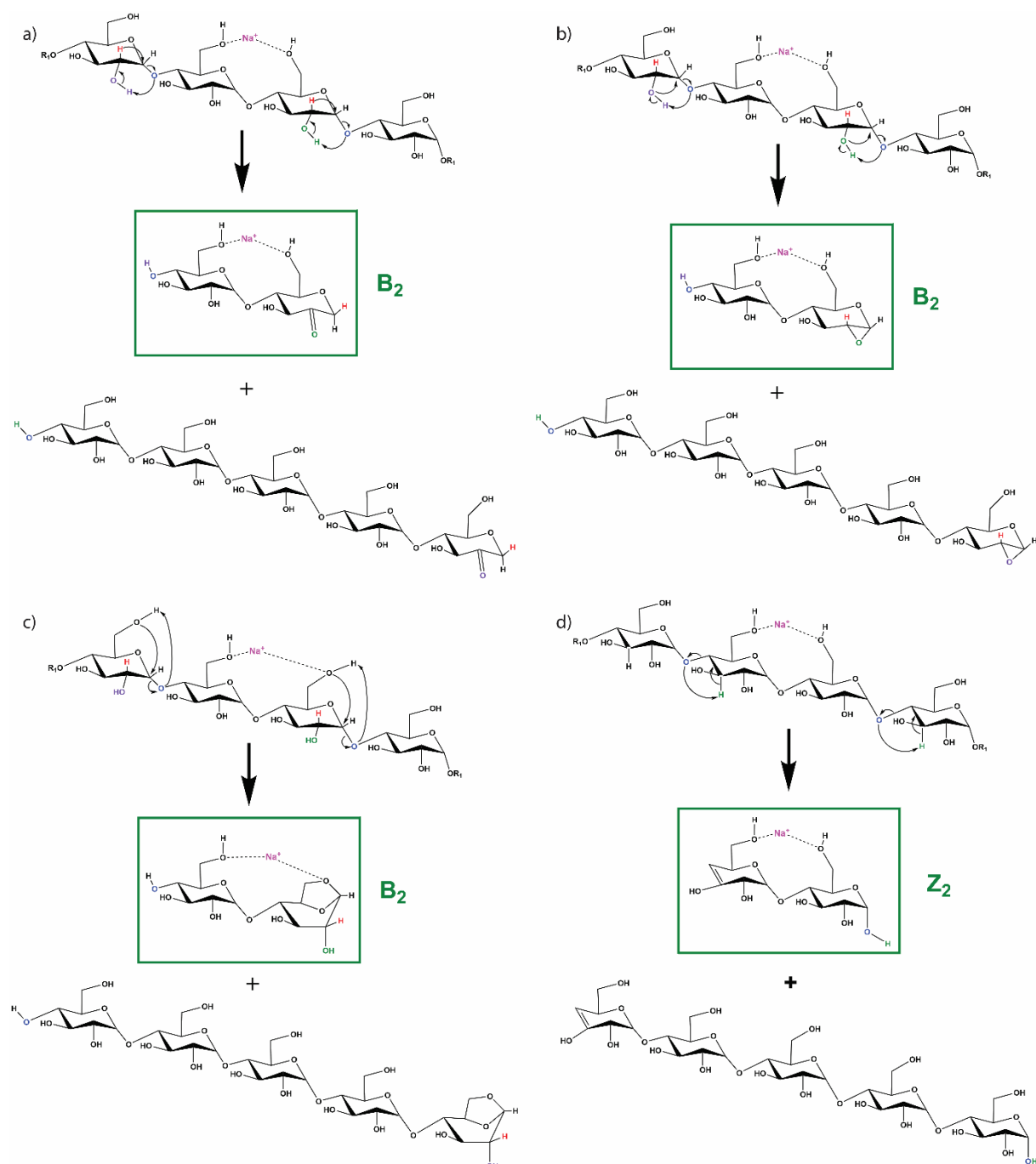


Figure A1: Simplified mechanisms for glycosidic bond dissociation in $[\beta\text{-CD}+\text{Na}]^+$ leading to the (a) 2-ketone B₂ ion, (b) the 1,2-anhydro B₂ ion, (c) the 1,6-anhydro B₂ ion products and the (d) Z₂ ion product. The latter involves formation of an alkene bond between C3 and C4 of the non-reducing end of the product ion.

Expt:

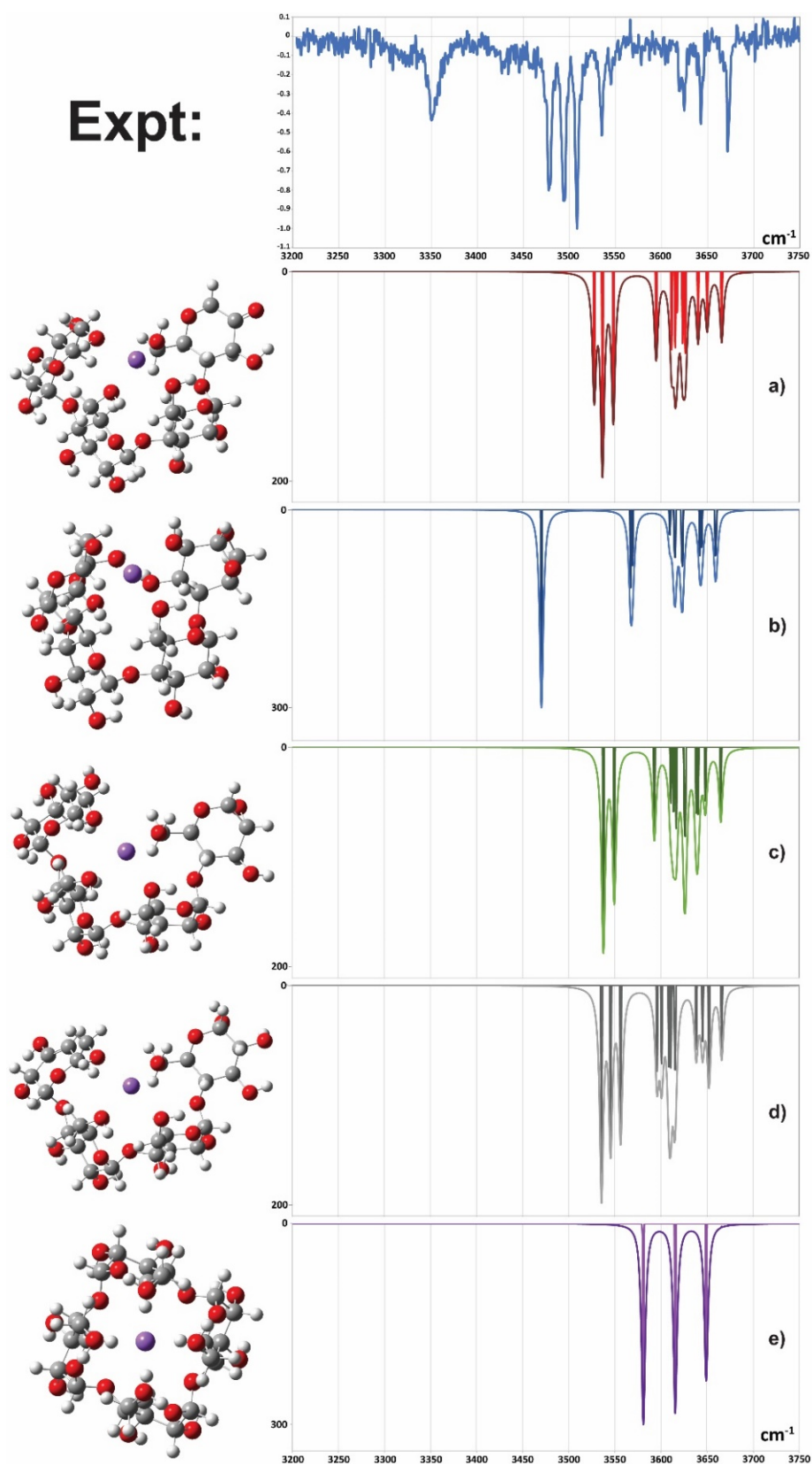


Figure A2: Comparison of m/z 671 lowest energy theoretical spectra with the experimental IR spectrum: lowest energy (a) 2-ketone B_4 ion structure; (b) 1,6-anhydro B_4 ion structure; (c) 1,2-anhydro B_4 ion structure; (d) Z_4 ion structure; (e) Cyclic ion (symmetrical) calculated at the B3LYP/6-31+G(d,p) level of theory.

Table A1. Relative energies of m/z 347 minima. Superscript “a” indicates single point calculations performed using the structure of each type calculated at the B3LYP/6-31+G(d,p) level of theory. Energies in kJ mol^{-1} .

m/z 347 Structures	$\Delta E_{\text{el,0K+ZPE}} (\Delta G_{298\text{K}})$ B3LYP/6-31+G(d,p)	$\Delta E_{\text{el,0K}}$ M06-2X/6-311+G(2d,p) ^a	$\Delta E_{\text{el,0K}}$ wB97XD/6-311+G(2d,p) ^a
Ketone B ₂	0 (0)	7.0	0
Z ₂	14.9 (12.8)	14.4	15.8
1,6-andydro B ₂	22.2 (24.2)	0	3.4
1,2-andydro B ₂	106.4 (106.2)	84.8	90.0

Table A2. Relative energies of m/z 509 minima. Superscript “a” indicates single point calculations performed using the structure calculated at the B3LYP/6-31+G(d,p) level of theory. Energies in kJ mol^{-1} .

m/z 509 Structures	$\Delta E_{\text{el,0K+ZPE}} (\Delta G_{298\text{K}})$ B3LYP/6-31+G(d,p)	$\Delta E_{\text{el,0K}}$ M06-2X/6-311+G(2d,p) ^a	$\Delta E_{\text{el,0K}}$ wB97XD/6-311+G(2d,p) ^a
Ketone B ₃	0 (0)	9.9	0
Z ₃	21.8 (32.0)	21.3	19.5
1,6-andydro B ₃	29.2 (44.8)	0	0.3
1,2-andydro B ₃	86.5 (92.0)	83.7	85.5

Table A3. Relative energies of m/z 671 minima. Superscript “a” indicates single point calculations performed using the structure calculated at the B3LYP/6-31+G(d,p) level of theory. Energies in kJ mol^{-1} .

m/z 671 Structures	$\Delta E_{\text{el,0K+ZPE}} (\Delta G_{298\text{K}})$ B3LYP/6-31+G(d,p)	$\Delta E_{\text{el,0K}}$ M06-2X/6-311+G(2d,p) ^a	$\Delta E_{\text{el,0K}}$ wB97XD/6-311+G(2d,p) ^a
Ketone B ₄	0 (0)	0	0
Z ₄	11.5 (14.9)	2.0	11.0
1,6-andydro B ₄	41.6 (37.5)	1.4	4.2
Cyclic	56.3 (73.4)	58.6	10.2
1,2-andydro B ₄	89.0 (90.2)	74.4	83.4
Z ₄ ring-open	68.7 (63.7)	75.6	74.3
Z ₄ ring-open II	69.7 (57.4)	88.0	89.4

Acknowledgements

Obtaining the title of PhD would not have been possible if I had not had the good fortune to meet a collection of wonderful people who helped me through my journey. I will try to do justice to some of the key figures who have helped me grow into the scientist (yes, I can consider myself as such today!) I have become.

First and foremost, I would like to express my utmost gratitude to my PhD supervisor, Prof. Thomas R. Rizzo, a great scientist with a big heart, who took a chance on me and gave me the creative room and resources to develop my potential as a researcher.

Next, I would like to thank Dr. Eduardo Carrascosa and Dr. Yue Lei for having had the patience to teach me all the insider details about working with complex research instruments. It was by working alongside these two brilliant scientists that I finally “made the switch”, transitioning from a hesitant master student, uncertain of the outcome of every move, to a confident PhD, able to make intelligent decisions and take calculated risks.

I also thank Prof. Mark Muyskens, who came all the way from Wisconsin, USA, to do research in our lab, and ended up spending most of his time helping me fix the octupole cold trap, after I melted it by accident. His laid-back attitude and good humour really helped me through the darkest period of my doctoral thesis, when I was seriously considering just quitting and joining the army.

A great thanks to Dr. Stephan Warnke and Dr. Vasyl Yatsyna, who both provided excellent support and insights whenever needed.

My thanks goes out to the other PhD students of the group (past and present), in particular Dr. Valeriu Scutelnic who initiated me to this field of research and spent endless hours, discussing both technical and theoretical concepts with me when I was in my first year. Dr. Natalia Yalovenko for sharing lots of fun moments, teaching me Russian and being my guide at conferences. Dr. Ahmed Ben Faleh for being a great colleague and also my special friend. I would also like to mention the PhD students who will be graduating soon after me: Irina Dyukova, Pryanka Bansal, and Ali H. AbiKhodr. It has been a pleasure working with such promising new talent and I am convinced that they still have much to bring to our field of research.

Although sometimes forgotten, the very essence of our lab is reliant on the excellence of our mechanical and electronic workshops. I cannot overstate how the team of mechanics, headed by André Fattet and Yves Morier, has come up with ingenious solution whenever we needed to (re)-design a vacuum flange, or an ion lens, or a vacuum chamber, ... the list goes on and on. In the same way, Benjamin Charles Le Geyt, and his team at the electronic workshop has been able to work wonders in helping me design custom-made little devices which suit our specific (and often pressing needs).

And finally, I would like to thank my mother for having encouraged my love for science from an early age, and my little sister for having always been supportive throughout the ups and downs of life. I would not have been able to make it without you.

There are two more people that have positively impacted my life in these last four years in a way that I did not think was possible: my beloved wife Océanne, and my son Anakin. *Océanne, merci d'avoir été là pour moi durant ces quatre ans, merci de m'avoir supporté pendant les périodes difficiles, et d'avoir toujours cru en moi. Tu es la femme que tout homme rêvera d'avoir. Et Anakin, quand tu seras en âge de lire ça, tu t'en souviendras probablement plus de cette période de ta vie, mais te voir commencer à marcher, commencer à parler et simplement grandir m'a toujours apporté de la joie, même quand rien d'autre n'allait dans la vie. Tu étais ma motivation principale pendant toute cette thèse.*

And that's about it! Thank you, dear reader, for having made it to the end. I hope that some aspect of this thesis will be helpful to you or even a source of inspiration for your research.

Bye !

Robert

Curriculum Vitae

Robert Pellegrinelli

Research activity

June 2017 – Present : **Graduate research assistant for structural determination and sequencing of complex glycans at EPFL, Lausanne, Switzerland.**

- Work with and develop state-of-the-art analytical technologies for structural characterisation of complex oligosaccharides.
- Fingerprint large, N-linked glycans by cryogenic infrared spectroscopy.
- Characterize anomericity of glycosidic bonds by combining using ultra-high resolution ion mobility with tandem mass spectrometry (MS²) and cryogenic spectroscopy.
- Sample preparation of N-linked glycans produced from enzymatic reactions by HPLC, for MS and spectroscopic studies.
- Extensive troubleshooting experience on home-built and commercial analytical equipment.

Key achievements: Discover a fundamental property of glycan fragmentation providing an important new tool for glycomics. Develop a new analytical procedure that will allow to significantly reduce time and cost of developing a spectral database for glycans.

September 2016 – April 2017 : **QC specialist for the electrochemical corrosion of boron doped diamond (BDD) electrodes at CONDIAS GmbH, Itzehoe, Germany.**

- Develop and implement a new method for testing the electrochemical performance and long-term stability of prototype BDD electrodes.
- Install, calibrate and operate a cyclic voltammetry setup using Ag/AgCl electrode.
- Perform industrial-scale electrolysis for stability testing.

Key achievements: Propose an improvement in the standard operating procedure (SOP) of the quality control (QC) department, providing a better control over the performance quality of the product.

Teaching experience

September 2014 – December 2020 : **Teaching assistant for undergraduate courses at EPFL, Lausanne, Switzerland.**

- Coordinate livestream of lectures over Zoom for over 100 students, answering questions in the online chat and ensuring image and audio quality.
- Translate course material from English to French on short notice.
- Compile exercise series for general physics courses.
- Grade exams for first year bachelor's general physics and general chemistry both in English and French.
- Support bachelor students throughout exercise and exam review session for general physics and general chemistry courses.

Transferable skills

Presentation skills : excellent presenter, comfortable in front of large audiences. Successfully presented the group's research in a talk at the 67th ASMS Conference on Mass Spectrometry and Allied Topics in Atlanta, Georgia.

Computer skills : expert Microsoft Office and Igor Pro user, good knowledge of other systems including LaTeX, Matlab and gnuplot. Familiar with mass spectrometry and chromatography software (MassLynx™).

Interpersonal skills : team work mentality, averting unnecessary conflict through good and frequent communication.

Education

June 2017 – June 2021: **PhD in Chemistry and Chemical Engineering**, Ecole Polytechnique Fédérale de Lausanne.

September 2015 – April 2017: **MSc in Molecular and Biological Chemistry**, Ecole Polytechnique Fédérale de Lausanne.

September 2013 – June 2015: **BSc in Chemistry and Chemical Engineering**, Ecole Polytechnique Fédérale de Lausanne.

Languages

Native English speaker, fluent in French. Basic communication in German.

Publications

Jordan Rabus^{II}, **Robert P. Pellegrinelli**^{II}, Ali H. AbiKhodr, Benjamin J. Bythell, Thomas R. Rizzo and, Eduardo Carrascosa^{II}. "Unravelling the structures of sodiated β -cyclodextrin and its fragments." *Physical Chemistry Chemical Physics* 23, (2021): 13714-23.

Robert P. Pellegrinelli, Lei Yue, Eduardo Carrascosa, Stephan Warnke, Ahmed Ben Faleh, and Thomas R. Rizzo. "How General Is Anomeric Retention During Collision-Induced Dissociation of Glycans?". *Journal of the American Chemical Society* 142, no. 13 (2020/04/01/ 2020): 5948-51.

Carrascosa, Eduardo, **Robert P Pellegrinelli**, Thomas R Rizzo, and Mark A Muyskens. "Cryogenic Infrared Action Spectroscopy Fingerprints the Hydrogen Bonding Network in Gas-Phase Coumarin Cations." *The Journal of Physical Chemistry A* 124, no. 48 (2020): 9942-50.

Dyukova, Irina, Eduardo Carrascosa, **Robert P. Pellegrinelli**, and Thomas R. Rizzo. "Combining Cryogenic Infrared Spectroscopy with Selective Enzymatic Cleavage for Determining Glycan Primary Structure." *Analytical Chemistry* 92, no. 2 (2020/01/21 2020): 1658-62.

Warnke, Stephan, Ahmed Ben Faleh, **Robert P. Pellegrinelli**, Natalia Yalovenko, and Thomas R. Rizzo. "Combining Ultra-High Resolution Ion Mobility Spectrometry with Cryogenic Ir Spectroscopy for the Study of Biomolecular Ions." [In en]. *Faraday Discussions* 217, no. 0 (2019/07/22/ 2019): 114-25.

Bibliography

1. Fenn, J. B.; Mann, M.; Meng, C. K.; Wong, S. F.; Whitehouse, C. M., Electrospray ionization—principles and practice. *Mass Spectrometry Reviews* **1990**, *9* (1), 37-70.
2. Hillenkamp, F.; Karas, M.; Beavis, R. C.; Chait, B. T., Matrix-assisted laser desorption/ionization mass spectrometry of biopolymers. *Analytical chemistry* **1991**, *63* (24), 1193A-1203A.
3. Gowda, G. A. N.; Djukovic, D., Overview of Mass Spectrometry-Based Metabolomics: Opportunities and Challenges. In *Mass Spectrometry in Metabolomics: Methods and Protocols*, Raftery, D., Ed. Springer New York: New York, NY, 2014; pp 3-12.
4. Yates, J. R., Mass spectrometry: from genomics to proteomics. *Trends in Genetics* **2000**, *16* (1), 5-8.
5. Trock, B. J., Application of metabolomics to prostate cancer. *Urologic Oncology: Seminars and Original Investigations* **2011**, *29* (5), 572-581.
6. Williams, M. D.; Reeves, R.; Resar, L. S.; Hill, H. H., Metabolomics of colorectal cancer: past and current analytical platforms. *Analytical and Bioanalytical Chemistry* **2013**, *405* (15), 5013-5030.
7. Abbassi-Ghadi, N.; Kumar, S.; Huang, J.; Goldin, R.; Takats, Z.; Hanna, G. B., Metabolomic profiling of oesophago-gastric cancer: A systematic review. *European Journal of Cancer* **2013**, *49* (17), 3625-3637.
8. Shah Svati, H.; Kraus William, E.; Newgard Christopher, B., Metabolomic Profiling for the Identification of Novel Biomarkers and Mechanisms Related to Common Cardiovascular Diseases. *Circulation* **2012**, *126* (9), 1110-1120.
9. Rhee, E. P.; Gerszten, R. E., Metabolomics and Cardiovascular Biomarker Discovery. *Clinical Chemistry* **2012**, *58* (1), 139-147.
10. Chace, D. H.; Kalas, T. A., A biochemical perspective on the use of tandem mass spectrometry for newborn screening and clinical testing. *Clinical Biochemistry* **2005**, *38* (4), 296-309.
11. Rashed, M. S., Clinical applications of tandem mass spectrometry: ten years of diagnosis and screening for inherited metabolic diseases. *Journal of Chromatography B: Biomedical Sciences and Applications* **2001**, *758* (1), 27-48.
12. Mamas, M.; Dunn, W. B.; Neyses, L.; Goodacre, R., The role of metabolites and metabolomics in clinically applicable biomarkers of disease. *Archives of Toxicology* **2011**, *85* (1), 5-17.
13. Nemes, P.; Vertes, A., Ambient mass spectrometry for in vivo local analysis and in situ molecular tissue imaging. *TrAC Trends in Analytical Chemistry* **2012**, *34*, 22-34.
14. Harkewicz, R.; Dennis, E. A., Applications of Mass Spectrometry to Lipids and Membranes. *Annual Review of Biochemistry* **2011**, *80* (1), 301-325.
15. Hart, P. J.; Francese, S.; Claude, E.; Woodroffe, M. N.; Clench, M. R., MALDI-MS imaging of lipids in ex vivo human skin. *Analytical and Bioanalytical Chemistry* **2011**, *401* (1), 115-125.
16. Andersson, M.; Groseclose, M. R.; Deutch, A. Y.; Caprioli, R. M., Imaging mass spectrometry of proteins and peptides: 3D volume reconstruction. *Nature Methods* **2008**, *5* (1), 101-108.
17. Polfer, N. C.; Oomens, J., Vibrational spectroscopy of bare and solvated ionic complexes of biological relevance. *Mass Spectrometry Reviews* **2009**, *28* (3), 468-494.
18. Varki, A., Biological roles of glycans. *Glycobiology* **2017**, *27* (1), 3-49.
19. Rudd, P. M.; Elliott, T.; Cresswell, P.; Wilson, I. A.; Dwek, R. A., Glycosylation and the immune system. *Science* **2001**, *291* (5512), 2370-2376.
20. Stanley, P.; Cummings, R.; Varki, A.; Cummings, R. D.; Esko, J. D.; Stanley, P.; Hart, G. W.; Aebi, M.; Darvill, A. G.; Kinoshita, T.; Packer, N. H.; Prestegard, J. H.; Schnaar, R. L.; Seeberger, P. H., *Essentials of Glycobiology*. 2017.
21. Stanley, P.; Cummings, R. D., Structures common to different glycans. **2017**.
22. Le Mercier, P.; Mariethoz, J.; Lascano-Maillard, J.; Bonnardel, F.; Imbert, A.; Ricard-Blum, S.; Lisacek, F., A Bioinformatics View of Glycan–Virus Interactions. *Viruses* **2019**, *11* (4).
23. Wang, C.-C.; Chen, J.-R.; Tseng, Y.-C.; Hsu, C.-H.; Hung, Y.-F.; Chen, S.-W.; Chen, C.-M.; Khoo, K.-H.; Cheng, T.-J.; Cheng, Y.-S. E., Glycans on influenza hemagglutinin affect receptor binding and immune response. *Proceedings of the National Academy of Sciences* **2009**, *106* (43), 18137-18142.
24. Das, S. R.; Hensley, S. E.; David, A.; Schmidt, L.; Gibbs, J. S.; Puigbò, P.; Ince, W. L.; Bennink, J. R.; Yewdell, J. W., Fitness costs limit influenza A virus hemagglutinin glycosylation as an immune evasion strategy. *Proceedings of the National Academy of Sciences* **2011**, *108* (51), E1417-E1422.

25. Shajahan, A.; Supekar, N. T.; Gleinich, A. S.; Azadi, P., Deducing the N- and O-glycosylation profile of the spike protein of novel coronavirus SARS-CoV-2. *Glycobiology* **2020**, *30* (12), 981-988.
26. Walls, A. C.; Park, Y.-J.; Tortorici, M. A.; Wall, A.; McGuire, A. T.; Veesler, D., Structure, Function, and Antigenicity of the SARS-CoV-2 Spike Glycoprotein. *Cell* **2020**, *181* (2), 281-292.e6.
27. Clark, M. A.; Douglas, M.; Choi, J., *Biology 2e*. OpenStax: 2018.
28. Shurer, C. R.; Kuo, J. C.-H.; Roberts, L. M.; Gandhi, J. G.; Colville, M. J.; Enoki, T. A.; Pan, H.; Su, J.; Noble, J. M.; Hollander, M. J.; O'Donnell, J. P.; Yin, R.; Pedram, K.; Möckl, L.; Kourkoutis, L. F.; Moerner, W. E.; Bertozzi, C. R.; Feigenson, G. W.; Reesink, H. L.; Paszek, M. J., Physical Principles of Membrane Shape Regulation by the Glycocalyx. *Cell* **2019**, *177* (7), 1757-1770.e21.
29. Pigman, W.; Isbell, H. S., Mutarotation of Sugars in Solution. In *Advances in Carbohydrate Chemistry*, Wolfrom, M. L.; Tipson, R. S., Eds. Academic Press: 1968; Vol. 23, pp 11-57.
30. Laine, R. A., Invited Commentary: A calculation of all possible oligosaccharide isomers both branched and linear yields 1.05×10^{12} structures for a reducing hexasaccharide: the Isomer Barrier to development of single-method saccharide sequencing or synthesis systems. *Glycobiology* **1994**, *4* (6), 759-767.
31. Varki, A.; Cummings, R. D.; Aebi, M.; Packer, N. H.; Seeberger, P. H.; Esko, J. D.; Stanley, P.; Hart, G.; Darvill, A.; Kinoshita, T.; Prestegard, J. J.; Schnaar, R. L.; Freeze, H. H.; Marth, J. D.; Bertozzi, C. R.; Etzler, M. E.; Frank, M.; Vliegthart, J. F. G.; Lütke, T.; Perez, S.; Bolton, E.; Rudd, P.; Paulson, J.; Kanehisa, M.; Toukach, P.; Aoki-Kinoshita, K. F.; Dell, A.; Narimatsu, H.; York, W.; Taniguchi, N.; Kornfeld, S., Symbol Nomenclature for Graphical Representations of Glycans. *Glycobiology* **2015**, *25* (12), 1323-1324.
32. Wormald, M. R.; Petrescu, A. J.; Pao, Y.-L.; Glithero, A.; Elliott, T.; Dwek, R. A., Conformational Studies of Oligosaccharides and Glycopeptides: Complementarity of NMR, X-ray Crystallography, and Molecular Modelling. *Chemical Reviews* **2002**, *102* (2), 371-386.
33. Vliegthart, J. F. G.; Dorland, L.; Halbeek, H. v., High-Resolution, ¹H-Nuclear Magnetic Resonance Spectroscopy as a Tool in the Structural Analysis of Carbohydrates Related to Glycoproteins. In *Advances in Carbohydrate Chemistry and Biochemistry*, Tipson, R. S.; Horton, D., Eds. Academic Press: 1983; Vol. 41, pp 209-374.
34. Lundborg, M.; Widmalm, G., Structural Analysis of Glycans by NMR Chemical Shift Prediction. *Analytical Chemistry* **2011**, *83* (5), 1514-1517.
35. Battistel, M. D.; Azurmendi, H. F.; Yu, B.; Freedberg, D. I., NMR of glycans: Shedding new light on old problems. *Progress in Nuclear Magnetic Resonance Spectroscopy* **2014**, *79*, 48-68.
36. Lu, G.; Crieffeld, C. L.; Gattu, S.; Veltri, L. M.; Holland, L. A., Capillary Electrophoresis Separations of Glycans. *Chemical Reviews* **2018**, *118* (17), 7867-7885.
37. Ruhaak, L. R.; Hennig, R.; Huhn, C.; Borowiak, M.; Dolhain, R. J. E. M.; Deelder, A. M.; Rapp, E.; Wührer, M., Optimized Workflow for Preparation of APTS-Labeled N-Glycans Allowing High-Throughput Analysis of Human Plasma Glycomes using 48-Channel Multiplexed CGE-LIF. *Journal of Proteome Research* **2010**, *9* (12), 6655-6664.
38. Guttman, A.; Herrick, S., Effect of the Quantity and Linkage Position of Mannose(α1,2) Residues in Capillary Gel Electrophoresis of High-Mannose-Type Oligosaccharides. *Analytical Biochemistry* **1996**, *235* (2), 236-239.
39. Kotani, N.; Takasaki, S., Analysis of 2-Aminobenzamide-Labeled Oligosaccharides by High-pH Anion-Exchange Chromatography with Fluorometric Detection. *Analytical Biochemistry* **1998**, *264* (1), 66-73.
40. Walsh, I.; Nguyen-Khuong, T.; Wongtrakul-Kish, K.; Tay, S. J.; Chew, D.; José, T.; Taron, C. H.; Rudd, P. M., GlycanAnalyzer: software for automated interpretation of N-glycan profiles after exoglycosidase digestions. *Bioinformatics* **2019**, *35* (4), 688-690.
41. Yamagami, M.; Matsui, Y.; Hayakawa, T.; Yamamoto, S.; Kinoshita, M.; Suzuki, S., Plug-plug kinetic capillary electrophoresis for in-capillary exoglycosidase digestion as a profiling tool for the analysis of glycoprotein glycans. *Journal of Chromatography A* **2017**, *1496*, 157-162.
42. Mariño, K.; Bones, J.; Kattla, J. J.; Rudd, P. M., A systematic approach to protein glycosylation analysis: a path through the maze. *Nature Chemical Biology* **2010**, *6* (10), 713-723.
43. Royle, L.; Campbell, M. P.; Radcliffe, C. M.; White, D. M.; Harvey, D. J.; Abrahams, J. L.; Kim, Y.-G.; Henry, G. W.; Shadick, N. A.; Weinblatt, M. E.; Lee, D. M.; Rudd, P. M.; Dwek, R. A., HPLC-based analysis of serum N-glycans on a 96-well plate platform with dedicated database software. *Analytical Biochemistry* **2008**, *376* (1), 1-12.
44. Guttman, A.; Ulfelder, K. W., Exoglycosidase matrix-mediated sequencing of a complex glycan pool by capillary electrophoresis. *Journal of Chromatography A* **1997**, *781* (1), 547-554.
45. Kailemia, M. J.; Ruhaak, L. R.; Lebrilla, C. B.; Amster, I. J., Oligosaccharide Analysis by Mass Spectrometry: A Review of Recent Developments. *Analytical Chemistry* **2014**, *86* (1), 196-212.

46. Zaia, J., Mass spectrometry of oligosaccharides. *Mass Spectrometry Reviews* **2004**, 23 (3), 161-227.
47. Mechref, Y.; Novotny, M. V.; Krishnan, C., Structural Characterization of Oligosaccharides Using Maldi-TOF/TOF Tandem Mass Spectrometry. *Analytical Chemistry* **2003**, 75 (18), 4895-4903.
48. Harvey, D. J., Collision-induced fragmentation of underivatized N-linked carbohydrates ionized by electrospray. *Journal of Mass Spectrometry* **2000**, 35 (10), 1178-1190.
49. Yu, X.; Jiang, Y.; Chen, Y.; Huang, Y.; Costello, C. E.; Lin, C., Detailed Glycan Structural Characterization by Electronic Excitation Dissociation. *Analytical Chemistry* **2013**, 85 (21), 10017-10021.
50. Harvey, D. J.; Royle, L.; Radcliffe, C. M.; Rudd, P. M.; Dwek, R. A., Structural and quantitative analysis of N-linked glycans by matrix-assisted laser desorption ionization and negative ion nanospray mass spectrometry. *Analytical Biochemistry* **2008**, 376 (1), 44-60.
51. Gaucher, S. P.; Leary, J. A., Determining anomericity of the glycosidic bond in Zn (II)-diethylenetriamine-disaccharide complexes using MSⁿ in a quadrupole ion trap. *J. Am. Soc. Mass Spectrom.* **1999**, 10 (3), 269.
52. Tsai, S.-T.; Liew, C. Y.; Hsu, C.; Huang, S.-P.; Weng, W.-C.; Kuo, Y.-H.; Ni, C.-K., Automatic Full Glycan Structural Determination through Logically Derived Sequence Tandem Mass Spectrometry. *ChemBioChem* **2019**, 20 (18), 2351-2359.
53. Royle, L.; Mattu, T. S.; Hart, E.; Langridge, J. I.; Merry, A. H.; Murphy, N.; Harvey, D. J.; Dwek, R. A.; Rudd, P. M., An Analytical and Structural Database Provides a Strategy for Sequencing O-Glycans from Microgram Quantities of Glycoproteins. *Analytical Biochemistry* **2002**, 304 (1), 70-90.
54. Welply, J. K., Sequencing methods for carbohydrates and their biological applications. *Trends Biotechnol.* **1989**, 7 (1), 5.
55. Morelle, W.; Michalski, J.-C., Analysis of protein glycosylation by mass spectrometry. *Nature Protocols* **2007**, 2 (7), 1585-1602.
56. Cumeras, R.; Figueras, E.; Davis, C. E.; Baumbach, J. I.; Gràcia, I., Review on Ion Mobility Spectrometry. Part 1: current instrumentation. *Analyst* **2015**, 140 (5), 1376-1390.
57. Hopfgartner, G., Current developments in ion mobility spectrometry. *Analytical and Bioanalytical Chemistry* **2019**, 411 (24), 6227-6227.
58. Bohrer, B. C.; Merenbloom, S. I.; Koeniger, S. L.; Hilderbrand, A. E.; Clemmer, D. E., Biomolecule Analysis by Ion Mobility Spectrometry. *Annual Review of Analytical Chemistry* **2008**, 1 (1), 293-327.
59. Shelimov, K. B.; Clemmer, D. E.; Hudgins, R. R.; Jarrold, M. F., Protein Structure in Vacuo: Gas-Phase Conformations of BPTI and Cytochrome c. *Journal of the American Chemical Society* **1997**, 119 (9), 2240-2248.
60. Clemmer, D. E.; Jarrold, M. F., Ion Mobility Measurements and their Applications to Clusters and Biomolecules. *Journal of Mass Spectrometry* **1997**, 32 (6), 577-592.
61. Hoaglund, C. S.; Valentine, S. J.; Sporleder, C. R.; Reilly, J. P.; Clemmer, D. E., Three-Dimensional Ion Mobility/TOFMS Analysis of Electrosprayed Biomolecules. *Analytical Chemistry* **1998**, 70 (11), 2236-2242.
62. Dwivedi, P.; Wu, C.; Matz, L. M.; Clowers, B. H.; Siems, W. F.; Hill, H. H., Gas-Phase Chiral Separations by Ion Mobility Spectrometry. *Analytical Chemistry* **2006**, 78 (24), 8200-8206.
63. Uetrecht, C.; Barbu, I. M.; Shoemaker, G. K.; van Duijn, E.; Heck, A. J. R., Interrogating viral capsid assembly with ion mobility-mass spectrometry. *Nature Chemistry* **2011**, 3 (2), 126-132.
64. Both, P.; Green, A. P.; Gray, C. J.; Šardžik, R.; Voglmeir, J.; Fontana, C.; Austeri, M.; Rejzek, M.; Richardson, D.; Field, R. A.; Widmalm, G.; Flitsch, S. L.; Evers, C. E., Discrimination of epimeric glycans and glycopeptides using IM-MS and its potential for carbohydrate sequencing. *Nature Chemistry* **2014**, 6 (1), 65-74.
65. Gray, C. J.; Thomas, B.; Upton, R.; Migas, L. G.; Evers, C. E.; Barran, P. E.; Flitsch, S. L., Applications of ion mobility mass spectrometry for high throughput, high resolution glycan analysis. *Biochimica et Biophysica Acta (BBA) - General Subjects* **2016**, 1860 (8), 1688-1709.
66. Pagel, K.; Harvey, D. J., Ion Mobility-Mass Spectrometry of Complex Carbohydrates: Collision Cross Sections of Sodiated N-linked Glycans. *Analytical Chemistry* **2013**, 85 (10), 5138-5145.
67. Williams, J. P.; Grabenauer, M.; Holland, R. J.; Carpenter, C. J.; Wormald, M. R.; Giles, K.; Harvey, D. J.; Bateman, R. H.; Scrivens, J. H.; Bowers, M. T., Characterization of simple isomeric oligosaccharides and the rapid separation of glycan mixtures by ion mobility mass spectrometry. *International Journal of Mass Spectrometry* **2010**, 298 (1), 119-127.
68. Harvey, D. J.; Scarff, C. A.; Crispin, M.; Scanlan, C. N.; Bonomelli, C.; Scrivens, J. H., MALDI-MS/MS with Traveling Wave Ion Mobility for the Structural Analysis of N-Linked Glycans. *Journal of the American Society for Mass Spectrometry* **2012**, 23 (11), 1955-1966.
69. Zheng, X.; Zhang, X.; Schocker, N. S.; Renslow, R. S.; Orton, D. J.; Khamsi, J.; Ashmus, R. A.; Almeida, I. C.; Tang, K.; Costello, C. E., Enhancing glycan isomer separations with metal ions and positive and negative

- polarity ion mobility spectrometry-mass spectrometry analyses. *Analytical and bioanalytical chemistry* **2017**, 409 (2), 467-476.
70. Pu, Y.; Ridgeway, M. E.; Glaskin, R. S.; Park, M. A.; Costello, C. E.; Lin, C., Separation and Identification of Isomeric Glycans by Selected Accumulation-Trapped Ion Mobility Spectrometry-Electron Activated Dissociation Tandem Mass Spectrometry. *Analytical Chemistry* **2016**, 88 (7), 3440-3443.
 71. Mookherjee, A.; Uppal, S. S.; Murphree, T. A.; Guttman, M., Linkage Memory in Underivatized Protonated Carbohydrates. *Journal of the American Society for Mass Spectrometry* **2020**.
 72. Gray, C. J.; Schindler, B.; Migas, L. G.; Pičmanová, M.; Allouche, A. R.; Green, A. P.; Mandal, S.; Motawia, M. S.; Sánchez-Pérez, R.; Bjarnholt, N.; Møller, B. L.; Rijs, A. M.; Barran, P. E.; Compagnon, I.; Eysers, C. E.; Flitsch, S. L., Bottom-Up Elucidation of Glycosidic Bond Stereochemistry. *Analytical Chemistry* **2017**, 89 (8), 4540-4549.
 73. Hofmann, J.; Hahm, H. S.; Seeberger, P. H.; Pagel, K., Identification of carbohydrate anomers using ion mobility-mass spectrometry. *Nature* **2015**, 526 (7572), 241-244.
 74. Liu, Y.; Clemmer, D. E., Characterizing Oligosaccharides Using Injected-Ion Mobility/Mass Spectrometry. *Analytical Chemistry* **1997**, 69 (13), 2504-2509.
 75. Hofmann, J.; Stuckmann, A.; Crispin, M.; Harvey, D. J.; Pagel, K.; Struwe, W. B., Identification of Lewis and Blood Group Carbohydrate Epitopes by Ion Mobility-Tandem-Mass Spectrometry Fingerprinting. *Analytical Chemistry* **2017**, 89 (4), 2318-2325.
 76. Hofmann, J.; Pagel, K., Glycan Analysis by Ion Mobility-Mass Spectrometry. *Angewandte Chemie International Edition* **2017**, 56 (29), 8342-8349.
 77. Hamid, A. M.; Ibrahim, Y. M.; Garimella, S. V. B.; Webb, I. K.; Deng, L.; Chen, T.-C.; Anderson, G. A.; Prost, S. A.; Norheim, R. V.; Tolmachev, A. V.; Smith, R. D., Characterization of Traveling Wave Ion Mobility Separations in Structures for Lossless Ion Manipulations. *Analytical Chemistry* **2015**, 87 (22), 11301-11308.
 78. Deng, L.; Ibrahim, Y. M.; Hamid, A. M.; Garimella, S. V. B.; Webb, I. K.; Zheng, X.; Prost, S. A.; Sandoval, J. A.; Norheim, R. V.; Anderson, G. A.; Tolmachev, A. V.; Baker, E. S.; Smith, R. D., Ultra-High Resolution Ion Mobility Separations Utilizing Traveling Waves in a 13 m Serpentine Path Length Structures for Lossless Ion Manipulations Module. *Analytical Chemistry* **2016**, 88 (18), 8957-8964.
 79. Hollerbach, A. L.; Li, A.; Prabhakaran, A.; Nagy, G.; Harrilal, C. P.; Conant, C. R.; Norheim, R. V.; Schimelfenig, C. E.; Anderson, G. A.; Garimella, S. V. B.; Smith, R. D.; Ibrahim, Y. M., Ultra-High-Resolution Ion Mobility Separations Over Extended Path Lengths and Mobility Ranges Achieved using a Multilevel Structures for Lossless Ion Manipulations Module. *Analytical Chemistry* **2020**, 92 (11), 7972-7979.
 80. Nagy, G.; Attah, I. K.; Garimella, S. V. B.; Tang, K.; Ibrahim, Y. M.; Baker, E. S.; Smith, R. D., Unraveling the isomeric heterogeneity of glycans: ion mobility separations in structures for lossless ion manipulations. *Chem. Commun.* **2018**, 54 (83), 11701-11704.
 81. Hernandez, O.; Isenberg, S.; Steinmetz, V.; Glish, G. L.; Maitre, P., Probing Mobility-Selected Saccharide Isomers: Selective Ion-Molecule Reactions and Wavelength-Specific IR Activation. *The Journal of Physical Chemistry A* **2015**, 119 (23), 6057-6064.
 82. Schindler, B.; Barnes, L.; Renois, G.; Gray, C.; Chambert, S.; Fort, S.; Flitsch, S.; Loison, C.; Allouche, A.-R.; Compagnon, I., Anomeric memory of the glycosidic bond upon fragmentation and its consequences for carbohydrate sequencing. *Nature Communications* **2017**, 8 (1), 973.
 83. Rabus, J. M.; Simmons, D. R.; Maître, P.; Bythell, B. J., Deprotonated carbohydrate anion fragmentation chemistry: structural evidence from tandem mass spectrometry, infra-red spectroscopy, and theory. *Physical Chemistry Chemical Physics* **2018**, 20 (44), 27897-27909.
 84. Depraz Depland, A.; Renois-Predelus, G.; Schindler, B.; Compagnon, I., Identification of sialic acid linkage isomers in glycans using coupled InfraRed Multiple Photon Dissociation (IRMPD) spectroscopy and mass spectrometry. *International Journal of Mass Spectrometry* **2018**, 434, 65-69.
 85. Polfer, N. C.; Valle, J. J.; Moore, D. T.; Oomens, J.; Eyler, J. R.; Bendiak, B., Differentiation of Isomers by Wavelength-Tunable Infrared Multiple-Photon Dissociation-Mass Spectrometry: Application to Glucose-Containing Disaccharides. *Analytical Chemistry* **2006**, 78 (3), 670-679.
 86. Gray, C. J.; Compagnon, I.; Flitsch, S. L., Mass spectrometry hybridized with gas-phase InfraRed spectroscopy for glycan sequencing. *Current Opinion in Structural Biology* **2020**, 62, 121-131.
 87. Schindler, B.; Barnes, L.; Gray, C. J.; Chambert, S.; Flitsch, S. L.; Oomens, J.; Daniel, R.; Allouche, A. R.; Compagnon, I., IRMPD Spectroscopy Sheds New (Infrared) Light on the Sulfate Pattern of Carbohydrates. *Journal of Physical Chemistry A* **2017**, 121 (10), 2114-2120.
 88. Rizzo, T. R.; Boyarkin, O. V., Cryogenic Methods for the Spectroscopy of Large, Biomolecular Ions. In *Gas-Phase IR Spectroscopy and Structure of Biological Molecules*, Rijs, A. M.; Oomens, J., Eds. Springer International Publishing: Cham, 2015; pp 43-97.

89. Masellis, C.; Khanal, N.; Kamrath, M. Z.; Clemmer, D. E.; Rizzo, T. R., Cryogenic Vibrational Spectroscopy Provides Unique Fingerprints for Glycan Identification. *J. Am. Soc. Mass Spectrom.* **2017**, *28* (10), 2217.
90. Mucha, E.; González Flórez, A. I.; Marianski, M.; Thomas, D. A.; Hoffmann, W.; Struwe, W. B.; Hahm, H. S.; Gewinner, S.; Schöllkopf, W.; Seeberger, P. H.; von Helden, G.; Pagel, K., Glycan Fingerprinting via Cold-Ion Infrared Spectroscopy. *Angewandte Chemie International Edition* **2017**, *56* (37), 11248-11251.
91. Warnke, S.; Ben Faleh, A.; Scutelnic, V.; Rizzo, T. R., Separation and Identification of Glycan Anomers Using Ultrahigh-Resolution Ion-Mobility Spectrometry and Cryogenic Ion Spectroscopy. *Journal of the American Society for Mass Spectrometry* **2019**, *30* (11), 2204-2211.
92. Ben Faleh, A.; Warnke, S.; Rizzo, T. R., Combining Ultrahigh-Resolution Ion-Mobility Spectrometry with Cryogenic Infrared Spectroscopy for the Analysis of Glycan Mixtures. *Analytical Chemistry* **2019**, *91* (7), 4876-4882.
93. Yalovenko, N.; Yatsyna, V.; Bansal, P.; H. AbiKhodr, A.; R. Rizzo, T., Analyzing glycans cleaved from a biotherapeutic protein using ultrahigh-resolution ion mobility spectrometry together with cryogenic ion spectroscopy. *Analyst* **2020**, *145* (20), 6493-6499.
94. Khanal, N.; Masellis, C.; Z. Kamrath, M.; E. Clemmer, D.; R. Rizzo, T., Cryogenic IR spectroscopy combined with ion mobility spectrometry for the analysis of human milk oligosaccharides. *Analyst* **2018**, *143* (8), 1846-1852.
95. Han, L.; Costello, C. E., Mass spectrometry of glycans. *Biochemistry (Moscow)* **2013**, *78* (7), 710-720.
96. An, H. J.; Lebrilla, C. B., Structure elucidation of native N- and O-linked glycans by tandem mass spectrometry (tutorial). *Mass Spectrometry Reviews* **2011**, *30* (4), 560-578.
97. Lemoine, J.; Fournet, B.; Despeyroux, D.; Jennings, K. R.; Rosenberg, R.; de Hoffmann, E., Collision-induced dissociation of alkali metal cationized and permethylated oligosaccharides: Influence of the collision energy and of the collision gas for the assignment of linkage position. *Journal of the American Society for Mass Spectrometry* **1993**, *4* (3), 197-203.
98. Harvey, D. J.; Bateman, R. H.; Green, M. R., High-energy collision-induced fragmentation of complex oligosaccharides ionized by matrix-assisted laser desorption/ionization mass spectrometry. *Journal of mass spectrometry* **1997**, *32* (2), 167-187.
99. Zhao, C.; Xie, B.; Chan, S.-Y.; Costello, C. E.; O'Connor, P. B., Collisionally activated dissociation and electron capture dissociation provide complementary structural information for branched permethylated oligosaccharides. *Journal of the American Society for Mass Spectrometry* **2008**, *19* (1), 138-150.
100. Wolff, J. J.; Chi, L.; Linhardt, R. J.; Amster, I. J., Distinguishing Glucuronic from Iduronic Acid in Glycosaminoglycan Tetrasaccharides by Using Electron Detachment Dissociation. *Analytical Chemistry* **2007**, *79* (5), 2015-2022.
101. Han, L.; Costello, C. E., Electron Transfer Dissociation of Milk Oligosaccharides. *Journal of the American Society for Mass Spectrometry* **2011**, *22* (6), 997-1013.
102. Lancaster, K. S.; An, H. J.; Li, B.; Lebrilla, C. B., Interrogation of N-Linked Oligosaccharides Using Infrared Multiphoton Dissociation in FT-ICR Mass Spectrometry. *Analytical Chemistry* **2006**, *78* (14), 4990-4997.
103. Domon, B.; Costello, C. E., A systematic nomenclature for carbohydrate fragmentations in FAB-MS/MS spectra of glycoconjugates. *Glycoconjugate J* **1988**, *5* (4), 397-409.
104. Harvey, D. J., Fragmentation of negative ions from carbohydrates: Part 1. Use of nitrate and other anionic adducts for the production of negative ion electrospray spectra from N-linked carbohydrates. *Journal of the American Society for Mass Spectrometry* **2005**, *16* (5), 622-630.
105. Harvey, D. J., Fragmentation of negative ions from carbohydrates: Part 2. Fragmentation of high-mannose N-linked glycans. *Journal of the American Society for Mass Spectrometry* **2005**, *16* (5), 631-646.
106. Abutokaikah, M. T.; Frye, J. W.; Tschampel, J.; Rabus, J. M.; Bythell, B. J., Fragmentation Pathways of Lithiated Hexose Monosaccharides. *Journal of the American Society for Mass Spectrometry* **2018**, *29* (8), 1627-1637.
107. Adamson, J. T.; Håkansson, K., Electron Capture Dissociation of Oligosaccharides Ionized with Alkali, Alkaline Earth, and Transition Metals. *Analytical Chemistry* **2007**, *79* (7), 2901-2910.
108. Cancilla, M. T.; Wong, A. W.; Voss, L. R.; Lebrilla, C. B., Fragmentation Reactions in the Mass Spectrometry Analysis of Neutral Oligosaccharides. *Analytical Chemistry* **1999**, *71* (15), 3206-3218.
109. Zhou, S.; Dong, X.; Veillon, L.; Huang, Y.; Mechref, Y., LC-MS/MS analysis of permethylated N-glycans facilitating isomeric characterization. *Analytical and bioanalytical chemistry* **2017**, *409* (2), 453-466.

110. Wang, H.; Zhang, J.; Dong, J.; Hou, M.; Pan, W.; Bu, D.; Zhou, J.; Zhang, Q.; Wang, Y.; Zhao, K.; Li, Y.; Huang, C.; Sun, S., Identification of glycan branching patterns using multistage mass spectrometry with spectra tree analysis. *Journal of Proteomics* **2020**, *217*, 103649.
111. Khanal, N.; Masellis, C.; Kamrath, M. Z.; Clemmer, D. E.; Rizzo, T. R., Glycosaminoglycan Analysis by Cryogenic Messenger-Tagging IR Spectroscopy Combined with IMS-MS. *Analytical Chemistry* **2017**, *89* (14), 7601-7606.
112. Bansal, P.; Yatsyna, V.; AbiKhodr, A. H.; Warnke, S.; Ben Faleh, A.; Yalovenko, N.; Wysocki, V. H.; Rizzo, T. R., Using SLIM-Based IMS-IMS Together with Cryogenic Infrared Spectroscopy for Glycan Analysis. *Analytical Chemistry* **2020**, *92* (13), 9079-9085.
113. Svendsen, A.; Lorenz, U. J.; Boyarkin, O. V.; Rizzo, T. R., A new tandem mass spectrometer for photofragment spectroscopy of cold, gas-phase molecular ions. *Review of Scientific Instruments* **2010**, *81* (7), 073107.
114. Kim, T.; Tang, K.; Udseth, H. R.; Smith, R. D., A Multicapillary Inlet Jet Disruption Electrodynamical Ion Funnel Interface for Improved Sensitivity Using Atmospheric Pressure Ion Sources. *Analytical Chemistry* **2001**, *73* (17), 4162-4170.
115. Aseev, O.; Rizzo, T. Spectroscopic studies of peptide fragments produced by collision-induced dissociation. EPFL, Lausanne, 2014.
116. De Leoz, M. L. A.; Simón-Manso, Y.; Woods, R. J.; Stein, S. E., Cross-Ring Fragmentation Patterns in the Tandem Mass Spectra of Underivatized Sialylated Oligosaccharides and Their Special Suitability for Spectrum Library Searching. *Journal of The American Society for Mass Spectrometry* **2019**, *30* (3), 426-438.
117. Ibrahim, Y.; Belov, M. E.; Tolmachev, A. V.; Prior, D. C.; Smith, R. D., Ion Funnel Trap Interface for Orthogonal Time-of-Flight Mass Spectrometry. *Analytical Chemistry* **2007**, *79* (20), 7845-7852.
118. Tolmachev, A. V.; Webb, I. K.; Ibrahim, Y. M.; Garimella, S. V. B.; Zhang, X.; Anderson, G. A.; Smith, R. D., Characterization of Ion Dynamics in Structures for Lossless Ion Manipulations. *Analytical Chemistry* **2014**, *86* (18), 9162-9168.
119. Webb, I. K.; Garimella, S. V. B.; Tolmachev, A. V.; Chen, T.-C.; Zhang, X.; Cox, J. T.; Norheim, R. V.; Prost, S. A.; LaMarche, B.; Anderson, G. A.; Ibrahim, Y. M.; Smith, R. D., Mobility-Resolved Ion Selection in Uniform Drift Field Ion Mobility Spectrometry/Mass Spectrometry: Dynamic Switching in Structures for Lossless Ion Manipulations. *Analytical Chemistry* **2014**, *86* (19), 9632-9637.
120. Garimella, S. V. B.; Ibrahim, Y. M.; Webb, I. K.; Tolmachev, A. V.; Zhang, X.; Prost, S. A.; Anderson, G. A.; Smith, R. D., Simulation of Electric Potentials and Ion Motion in Planar Electrode Structures for Lossless Ion Manipulations (SLIM). *Journal of the American Society for Mass Spectrometry* **2014**, *25* (11), 1890-1896.
121. Webb, I. K.; Garimella, S. V. B.; Norheim, R. V.; Baker, E. S.; Ibrahim, Y. M.; Smith, R. D., A Structures for Lossless Ion Manipulations (SLIM) Module for Collision Induced Dissociation. *Journal of the American Society for Mass Spectrometry* **2016**, *27* (7), 1285-1288.
122. Kemper, P. R.; Dupuis, N. F.; Bowers, M. T., A new, higher resolution, ion mobility mass spectrometer. *International Journal of Mass Spectrometry* **2009**, *287* (1), 46-57.
123. Shvartsburg, A. A.; Smith, R. D., Fundamentals of Traveling Wave Ion Mobility Spectrometry. *Analytical Chemistry* **2008**, *80* (24), 9689-9699.
124. Bythell, B. J.; Abutokaikah, M. T.; Wagoner, A. R.; Guan, S.; Rabus, J. M., Cationized Carbohydrate Gas-Phase Fragmentation Chemistry. *Journal of the American Society for Mass Spectrometry* **2017**, *28* (4), 688-703.
125. Rabus, J. M.; Abutokaikah, M. T.; Ross, R. T.; Bythell, B. J., Sodium-cationized carbohydrate gas-phase fragmentation chemistry: influence of glycosidic linkage position. *Physical Chemistry Chemical Physics* **2017**, *19* (37), 25643-25652.
126. Sleno, L.; Volmer, D. A., Ion activation methods for tandem mass spectrometry. *Journal of Mass Spectrometry* **2004**, *39* (10), 1091-1112.
127. Marcus, R. A., Unimolecular Dissociations and Free Radical Recombination Reactions. *The Journal of Chemical Physics* **1952**, *20* (3), 359-364.
128. Kenttamaa, H. I.; Cooks, R. G., Tautomer characterization by energy resolved mass spectrometry. Dimethyl phosphite and dimethyl phosphonate ions. *Journal of the American Chemical Society* **1985**, *107* (7), 1881-1886.
129. Dunbar, R. C., Infrared radiative cooling of isolated polyatomic molecules. *The Journal of Chemical Physics* **1989**, *90* (12), 7369-7375.
130. Ho, Y.-P.; Dunbar, R. C., Radiative cooling rate of 9-cyanophenanthrene ions by time-resolved photodissociation thermometry. *International Journal of Mass Spectrometry and Ion Processes* **1996**, *154* (3), 133-144.

131. Gray, C. J.; Migas, L. G.; Barran, P. E.; Pagel, K.; Seeberger, P. H.; Evers, C. E.; Boons, G. J.; Pohl, N. L. B.; Compagnon, I.; Widmalm, G.; Flitsch, S. L., Advancing Solutions to the Carbohydrate Sequencing Challenge. *J. Am. Chem. Soc.* **2019**, *141*, 14463.
132. Harvey, D. J., Identification of protein-bound carbohydrates by mass spectrometry. *Proteomics* **2001**, *1* (2), 311.
133. Hsu, H. C.; Liew, C. Y.; Huang, S. P.; Tsai, S. T.; Ni, C. K., Simple method for de novo structural determination of underivatized glucose oligosaccharides. *Sci. Rep.* **2018**, *8* (1), 5562.
134. Hsu, H. C.; Liew, C. Y.; Huang, S. P.; Tsai, S. T.; Ni, C. K., Simple approach for de novo structural identification of mannose trisaccharides. *J. Am. Soc. Mass Spectrom.* **2018**, *29* (3), 470.
135. Mucha, E.; González Flórez, A. I.; Marianski, M.; Thomas, D. A.; Hoffmann, W.; Struwe, W. B.; Hahm, H. S.; Gewinner, S.; Schöllkopf, W.; Seeberger, P. H., Glycan Fingerprinting Via Cold-Ion Infrared Spectroscopy. *Angew. Chem., Int. Ed.* **2017**, *56* (37), 11248.
136. Rizzo, T. R.; Boyarkin, O. V.; Rijs, A. M.; Oomens, J., *Gas-Phase IR Spectroscopy and Structure of Biological Molecules*. 2015; p 43.
137. Lorenz, U. J.; Rizzo, T. R., Multiple Isomers and Protonation Sites of the Phenylalanine/Serine Dimer. *Journal of the American Chemical Society* **2012**, *134* (27), 11053-11055.
138. Masson, A.; Kamrath, M. Z.; Perez, M. A. S.; Glover, M. S.; Rothlisberger, U.; Clemmer, D. E.; Rizzo, T. R., Infrared Spectroscopy of Mobility-Selected H⁺-Gly-Pro-Gly-Gly (GPGG). *Journal of the American Society for Mass Spectrometry* **2015**, *26* (9), 1444-1454.
139. Pereverzev, A. Y.; Cheng, X.; Nagornova, N. S.; Reese, D. L.; Steele, R. P.; Boyarkin, O. V., Vibrational Signatures of Conformer-Specific Intramolecular Interactions in Protonated Tryptophan. *The Journal of Physical Chemistry A* **2016**, *120* (28), 5598-5608.
140. Schindler, B.; Legentil, L.; Allouche, A.-R.; Ferrières, V.; Compagnon, I., Spectroscopic diagnostic for the ring-size of carbohydrates in the gas phase: furanose and pyranose forms of GalNAc. *Physical Chemistry Chemical Physics* **2019**, *21* (23), 12460-12467.
141. Deng, L.; Ibrahim, Y. M.; Baker, E. S.; Aly, N. A.; Hamid, A. M.; Zhang, X.; Zheng, X.; Garimella, S. V. B.; Webb, I. K.; Prost, S. A.; Sandoval, J. A.; Norheim, R. V.; Anderson, G. A.; Tolmachev, A. V.; Smith, R. D., Ion Mobility Separations of Isomers based upon Long Path Length Structures for Lossless Ion Manipulations Combined with Mass Spectrometry. *ChemistrySelect* **2016**, *1* (10), 2396-2399.
142. Warnke, S.; Faleh, A. B.; Pellegrinelli, R. P.; Yalovenko, N.; Rizzo, T. R., Combining ultra-high resolution ion mobility spectrometry with cryogenic IR spectroscopy for the study of biomolecular ions. *Faraday discussions* **2019**, *217*, 114-125.
143. Kanie, O.; Kurimoto, A.; Kanie, Y.; Daikoku, S.; Ohtake, A.; Suzuki, K., Analysis of behavior of sodiated sugar hemiacetals under low-energy collision-induced dissociation conditions and application to investigating mutarotation and mechanism of a glycosidase. *Proceedings of the Japan Academy, Series B* **2009**, *85* (6), 204-215.
144. Alkorta, I.; Popelier, P. L. A., Computational study of mutarotation in erythrose and threose. *Carbohydrate Research* **2011**, *346* (18), 2933-2939.
145. Giles, K.; Ujma, J.; Wildgoose, J.; Pringle, S.; Richardson, K.; Langridge, D.; Green, M., A Cyclic Ion Mobility-Mass Spectrometry System. *Analytical Chemistry* **2019**, *91* (13), 8564-8573.
146. Ujma, J.; Ropartz, D.; Giles, K.; Richardson, K.; Langridge, D.; Wildgoose, J.; Green, M.; Pringle, S., Cyclic Ion Mobility Mass Spectrometry Distinguishes Anomers and Open-Ring Forms of Pentasaccharides. *Journal of the American Society for Mass Spectrometry* **2019**, *30* (6), 1028-1037.
147. Dyukova, I.; Ben Faleh, A.; Warnke, S.; Yalovenko, N.; Yatsyna, V.; Bansal, P.; Rizzo, T. R., A new approach for identifying positional isomers of glycans cleaved from monoclonal antibodies. *Analyst* **2021**.
148. Pellegrinelli, R. P.; Yue, L.; Carrascosa, E.; Warnke, S.; Ben Faleh, A.; Rizzo, T. R., How General Is Anomeric Retention during Collision-Induced Dissociation of Glycans? *Journal of the American Chemical Society* **2020**, *142* (13), 5948-5951.
149. Stanley, P.; Taniguchi, N.; Aebi, M., N-Glycans. In *Essentials of Glycobiology*, 3rd ed.; Varki, A.; Cummings, R. D.; Esko, J. D.; Stanley, P.; Hart, G. W.; Aebi, M.; Darvill, A. G.; Kinoshita, T.; Packer, N. H.; Prestegard, J. H.; Schnaar, R. L.; Seeberger, P. H., Eds. Cold Spring Harbor Laboratory Press: Cold Spring Harbor (NY), 2015.
150. Brockhausen, I.; Stanley, P., O-GalNAc Glycans. In *Essentials of Glycobiology*, 3rd ed.; Varki, A.; Cummings, R. D.; Esko, J. D.; Stanley, P.; Hart, G. W.; Aebi, M.; Darvill, A. G.; Kinoshita, T.; Packer, N. H.; Prestegard, J. H.; Schnaar, R. L.; Seeberger, P. H., Eds. Cold Spring Harbor Laboratory Press: Cold Spring Harbor (NY), 2015.

151. Scutelnic, V.; Rizzo, T. R., Cryogenic Ion Spectroscopy for Identification of Monosaccharide Anomers. *The Journal of Physical Chemistry A* **2019**, *123* (13), 2815-2819.
152. Partyka, J.; Foret, F., Cationic labeling of oligosaccharides for electrophoretic preconcentration and separation with contactless conductivity detection. *Journal of Chromatography A* **2012**, *1267*, 116-120.
153. Gattuso, G.; Nepogodiev, S. A.; Stoddart, J. F., Synthetic Cyclic Oligosaccharides. *Chemical Reviews* **1998**, *98* (5), 1919-1958.
154. Pedersen, C. J., Cyclic polyethers and their complexes with metal salts. *Journal of the American Chemical Society* **1967**, *89* (26), 7017-7036.
155. Hapiot, F.; Tilloy, S.; Monflier, E., Cyclodextrins as Supramolecular Hosts for Organometallic Complexes. *Chemical Reviews* **2006**, *106* (3), 767-781.
156. Casy, A. F.; Mercer, A. D., Application of cyclodextrins to chiral analysis by ¹H NMR spectroscopy. *Magnetic Resonance in Chemistry* **1988**, *26* (9), 765-774.
157. Řezanka, P.; Navrátilová, K.; Řezanka, M.; Král, V.; Sýkora, D., Application of cyclodextrins in chiral capillary electrophoresis. *Electrophoresis* **2014**, *35* (19), 2701-2721.
158. Biwer, A.; Antranikian, G.; Heinzle, E., Enzymatic production of cyclodextrins. *Appl Microbiol Biotechnol* **2002**, *59* (6), 609-617.
159. Crini, G., Review: A History of Cyclodextrins. *Chemical Reviews* **2014**, *114* (21), 10940-10975.
160. Davis, M. E.; Brewster, M. E., Cyclodextrin-based pharmaceuticals: past, present and future. *Nature Reviews Drug Discovery* **2004**, *3* (12), 1023-1035.
161. Del Valle, E. M. M., Cyclodextrins and their uses: a review. *Process Biochemistry* **2004**, *39* (9), 1033-1046.
162. Dias, H. M. A. M.; Berbic, F.; Pedrochi, F.; Baesso, M. L.; Matioli, G., Butter cholesterol removal using different complexation methods with beta-cyclodextrin, and the contribution of photoacoustic spectroscopy to the evaluation of the complex. *Food Research International* **2010**, *43* (4), 1104-1110.
163. Jones, S. T.; Cagno, V.; Janeček, M.; Ortiz, D.; Gasilova, N.; Piret, J.; Gasbarri, M.; Constant, D. A.; Han, Y.; Vuković, L.; Král, P.; Kaiser, L.; Huang, S.; Constant, S.; Kirkegaard, K.; Boivin, G.; Stellacci, F.; Tapparel, C., Modified cyclodextrins as broad-spectrum antivirals. *Science Advances* **2020**, *6* (5), eaax9318.
164. Lindner, K.; Saenger, W., β -Cyclodextrin Dodecahydrate: Crowding of Water Molecules within a Hydrophobic Cavity. *Angewandte Chemie International Edition in English* **1978**, *17* (9), 694-695.
165. Szejtli, J., Introduction and General Overview of Cyclodextrin Chemistry. *Chemical Reviews* **1998**, *98* (5), 1743-1754.
166. Griffiths, J., A Brief History of Mass Spectrometry. *Analytical Chemistry* **2008**, *80* (15), 5678-5683.
167. Gabelica, V.; Galic, N.; De Pauw, E., On the specificity of cyclodextrin complexes detected by electrospray mass spectrometry. *Journal of the American Society for Mass Spectrometry* **2002**, *13* (8), 946-953.
168. Lebrilla, C. B., The Gas-Phase Chemistry of Cyclodextrin Inclusion Complexes. *Accounts of Chemical Research* **2001**, *34* (8), 653-661.
169. Marangoci, N.; Mares, M.; Sillion, M.; Fífere, A.; Varganici, C.; Nicolescu, A.; Deleanu, C.; Coroaba, A.; Pinteala, M.; Simionescu, B. C., Inclusion complex of a new propiconazole derivative with β -cyclodextrin: NMR, ESI-MS and preliminary pharmacological studies. *Results in Pharma Sciences* **2011**, *1* (1), 27-37.
170. Reale, S.; Teixidó, E.; Angelis, F. d., Study of Alkali Metal Cations Binding Selectivity of β -Cyclodextrin by ESI-MS. *Annali di Chimica* **2005**, *95* (6), 375-381.
171. Sforza, S.; Galaverna, G.; Corradini, R.; Dossena, A.; Marchelli, R., ESI-mass spectrometry analysis of unsubstituted and disubstituted β -cyclodextrins: fragmentation mode and identification of the AB, AC, AD regioisomers. *Journal of the American Society for Mass Spectrometry* **2003**, *14* (2), 124-135.
172. Su, P.; Smith, A. J.; Warneke, J.; Laskin, J., Gas-Phase Fragmentation of Host-Guest Complexes of Cyclodextrins and Polyoxometalates. *Journal of The American Society for Mass Spectrometry* **2019**, *30* (10), 1934-1945.
173. He, F.; Ramirez, J.; Lebrilla, C. B., Evidence for an Intermolecular Proton-Transfer Reaction Induced by Collision in Gas-Phase Noncovalently Bound Complexes. *Journal of the American Chemical Society* **1999**, *121* (19), 4726-4727.
174. Sonnendecker, C.; Thürmann, S.; Przybylski, C.; Zitzmann, F. D.; Heinke, N.; Krauke, Y.; Monks, K.; Robitzki, A. A.; Belder, D.; Zimmermann, W., Large-Ring Cyclodextrins as Chiral Selectors for Enantiomeric Pharmaceuticals. *Angewandte Chemie International Edition* **2019**, *58* (19), 6411-6414.
175. Peptu, C.; Danchenko, M.; Škultéty, L.; Mosnáček, J., Structural Architectural Features of Cyclodextrin Oligoesters Revealed by Fragmentation Mass Spectrometry Analysis. *Molecules* **2018**, *23* (9).
176. Zhang, Q.; Li, G.-Z.; Becer, C. R.; Haddleton, D. M., Cyclodextrin-centred star polymers synthesized via a combination of thiol-ene click and ring opening polymerization. *Chem. Commun.* **2012**, *48* (65), 8063-8065.

177. Frański, R.; Gierczyk, B.; Schroeder, G.; Beck, S.; Springer, A.; Linscheid, M., Mass spectrometric decompositions of cationized β -cyclodextrin. *Carbohydrate Research* **2005**, *340* (8), 1567-1572.
178. Madhusudanan, K. P., Multiple lithium exchange under lithium cationization of cyclodextrins. *Journal of Mass Spectrometry* **2003**, *38* (4), 409-416.
179. Bythell, B. J.; Rabus, J. M.; Wagoner, A. R.; Abutokaikah, M. T.; Maître, P., Sequence Ion Structures and Dissociation Chemistry of Deprotonated Sucrose Anions. *Journal of The American Society for Mass Spectrometry* **2018**, *29* (12), 2380-2393.
180. Marianski, M.; Supady, A.; Ingram, T.; Schneider, M.; Baldauf, C., Assessing the Accuracy of Across-the-Scale Methods for Predicting Carbohydrate Conformational Energies for the Examples of Glucose and α -Maltose. *J. Chem. Theory Comput.* **2016**, *12* (12), 6157-6168.
181. Supady, A.; Blum, V.; Baldauf, C., First-Principles Molecular Structure Search with a Genetic Algorithm. *J. Chem. Inf. Model.* **2015**, *55* (11), 2338-2348.
182. Halgren, T. A., Merck molecular force field. I. Basis, form, scope, parameterization, and performance of MMFF94. *Journal of Computational Chemistry* **1996**, *17* (5-6), 490-519.
183. Halgren, T. A., Merck molecular force field. II. MMFF94 van der Waals and electrostatic parameters for intermolecular interactions. *Journal of Computational Chemistry* **1996**, *17* (5-6), 520-552.
184. Halgren, T. A., Merck molecular force field. III. Molecular geometries and vibrational frequencies for MMFF94. *Journal of Computational Chemistry* **1996**, *17* (5-6), 553-586.
185. Halgren, T. A.; Nachbar, R. B., Merck molecular force field. IV. conformational energies and geometries for MMFF94. *Journal of Computational Chemistry* **1996**, *17* (5-6), 587-615.
186. Halgren, T. A., Merck molecular force field. V. Extension of MMFF94 using experimental data, additional computational data, and empirical rules. *Journal of Computational Chemistry* **1996**, *17* (5-6), 616-641.
187. Frisch, M. J.; Trucks, G. W.; Schlegel, H. B.; Scuseria, G. E.; Robb, M. A.; Cheeseman, J. R.; Scalmani, G.; Barone, V.; Mennucci, B.; Petersson, G. A.; Nakatsuji, H.; Caricato, M.; Li, X.; Hratchian, H. P.; Izmaylov, A. F.; Bloino, J.; Zheng, G.; Sonnenberg, J. L.; Hada, M.; Ehara, M.; Toyota, K.; Fukuda, R.; Hasegawa, J.; Ishida, M.; Nakajima, T.; Honda, Y.; Kitao, O.; Nakai, H.; Vreven, T.; Montgomery, J. A., Jr.; Peralta, J. E.; Ogliaro, F.; Bearpark, M.; Heyd, J. J.; Brothers, E.; Kudin, K. N.; Staroverov, V. N.; Kobayashi, R.; Normand, J.; Raghavachari, K.; Rendell, A.; Burant, J. C.; Iyengar, S. S.; Tomasi, J.; Cossi, M.; Rega, N.; Millam, J. M.; Klene, M.; Knox, J. E.; Cross, J. B.; Bakken, V.; Adamo, C.; Jaramillo, J.; Gomperts, R.; Stratmann, R. E.; Yazyev, O.; Austin, A. J.; Cammi, R.; Pomelli, C.; Ochterski, J. W.; Martin, R. L.; Morokuma, K.; Zakrzewski, V. G.; Voth, G. A.; Salvador, P.; Dannenberg, J. J.; Dapprich, S.; Daniels, A. D.; Farkas, Ö.; Foresman, J. B.; Ortiz, J. V.; Cioslowski, J.; Fox, D. J., *Gaussian 09 Revision A.02*. 2009.
188. Becke, A. D., Density-functional thermochemistry. III. The role of exact exchange. *The Journal of Chemical Physics* **1993**, *98* (7), 5648-5652.
189. Lee, C.; Yang, W.; Parr, R. G., Development of the Colle-Salvetti correlation-energy formula into a functional of the electron density. *Phys. Rev. B* **1988**, *37* (2), 785-789.
190. Stephens, P. J.; Devlin, F. J.; Chabalowski, C. F.; Frisch, M. J., Ab Initio Calculation of Vibrational Absorption and Circular Dichroism Spectra Using Density Functional Force Fields. *J. Phys. Chem.* **1994**, *98* (45), 11623-11627.
191. Grimme, S., Exploration of Chemical Compound, Conformer, and Reaction Space with Meta-Dynamics Simulations Based on Tight-Binding Quantum Chemical Calculations. *J. Chem. Theory Comput.* **2019**, *15* (5), 2847-2862.
192. Pracht, P.; Bohle, F.; Grimme, S., Automated exploration of the low-energy chemical space with fast quantum chemical methods. *Physical Chemistry Chemical Physics* **2020**, *22* (14), 7169-7192.
193. Pracht, P.; Grimme, S., Calculation of absolute molecular entropies and heat capacities made simple. *Chemical Science* **2021**.
194. Snor, W.; Liedl, E.; Weiss-Greiler, P.; Karpfen, A.; Viernstein, H.; Wolschann, P., On the structure of anhydrous β -cyclodextrin. *Chemical Physics Letters* **2007**, *441* (1-3), 159-162.
195. Hamid, A. M.; Garimella, S. V. B.; Ibrahim, Y. M.; Deng, L.; Zheng, X.; Webb, I. K.; Anderson, G. A.; Prost, S. A.; Norheim, R. V.; Tolmachev, A. V.; Baker, E. S.; Smith, R. D., Achieving High Resolution Ion Mobility Separations Using Traveling Waves in Compact Multiturn Structures for Lossless Ion Manipulations. *Analytical Chemistry* **2016**, *88* (18), 8949-8956.
196. Przybylski, C.; Bonnet, V.; Cézar, C., Probing the common alkali metal affinity of native and variously methylated β -cyclodextrins by combining electrospray-tandem mass spectrometry and molecular modeling. *Physical Chemistry Chemical Physics* **2015**, *17* (29), 19288-19305.

197. Stachowicz, A.; Styrz, A.; Korchowiec, J.; Modaressi, A.; Rogalski, M., DFT studies of cation binding by β -cyclodextrin. *Theor Chem Acc* **2011**, *130* (4), 939-953.
198. Angelova, S. E.; Nikolova, V. K.; Dudev, T. M., Determinants of the host-guest interactions between α -, β - and γ -cyclodextrins and group IA, IIA and IIIA metal cations: a DFT/PCM study. *Physical Chemistry Chemical Physics* **2017**, *19* (23), 15129-15136.
199. Gámez, F.; Hurtado, P.; Hortal, A. R.; Martínez-Haya, B.; Berden, G.; Oomens, J., Cations in a Molecular Funnel: Vibrational Spectroscopy of Isolated Cyclodextrin Complexes with Alkali Metals. *ChemPhysChem* **2013**, *14* (2), 400-407.
200. Daskhan, G. C.; Jayaraman, N., Backbone-modified amphiphilic cyclic di- and tetrasaccharides. *Chem. Commun.* **2014**, *50* (62), 8554-8557.
201. Mukai, K.; Watanabe, H.; Oku, K.; Nishimoto, T.; Kubota, M.; Chaen, H.; Fukuda, S.; Kurimoto, M., An enzymatically produced novel cyclic tetrasaccharide, cyclo- $\{\rightarrow 6\}$ - α -d-Glcp-(1 \rightarrow 4)- α -d-Glcp-(1 \rightarrow 6)- α -d-Glcp-(1 \rightarrow 4)- α -d-Glcp-(1 \rightarrow) (cyclic maltosyl-(1 \rightarrow 6)-maltose), from starch. *Carbohydrate Research* **2005**, *340* (8), 1469-1474.
202. Ikuta, D.; Hirata, Y.; Wakamori, S.; Shimada, H.; Tomabechi, Y.; Kawasaki, Y.; Ikeuchi, K.; Hagimori, T.; Matsumoto, S.; Yamada, H., Conformationally supple glucose monomers enable synthesis of the smallest cyclodextrins. *Science* **2019**, *364* (6441), 674-677.
203. Immel, S.; Brickmann, J.; Lichtenthaler, F. W., Molecular modeling of saccharides, 6. Small-ring cyclodextrins: Their geometries and hydrophobic topographies. *Liebigs Ann.* **1995**, *1995* (6), 929-942.
204. Chen, J.-L.; Ngan, H. S.; Hsu, P.-J.; Tsai, S.-T.; Liew, C. Y.; Kuo, J.-L.; Hu, W.-P.; Ni, C.-K., Collision-induced dissociation of sodiated glucose and identification of anomeric configuration. *Physical Chemistry Chemical Physics* **2017**, *19* (23), 15454-15462.
205. Huynh, H. T.; Phan, H. T.; Hsu, P.-J.; Chen, J.-L.; Ngan, H. S.; Tsai, S.-T.; Roongcharoen, T.; Liew, C. Y.; Ni, C.-K.; Kuo, J.-L., Collision-induced dissociation of sodiated glucose, galactose, and mannose, and the identification of anomeric configurations. *Physical Chemistry Chemical Physics* **2018**, *20* (29), 19614-19624.

